



UNIVERSITY OF
BIRMINGHAM

**THE EFFECT OF NANOFORCES ON THE
ATTACHMENT OF CELLS**

By

YANG YANG

A Thesis submitted to
The University of Birmingham
For the degree of
DOCTOR OF PHILOSOPHY

Mechanical Engineering
College of Engineering and Physical Sciences
The University of Birmingham
[Feb. 2018]

UNIVERSITY OF
BIRMINGHAM

University of Birmingham Research Archive

e-theses repository

This unpublished thesis/dissertation is copyright of the author and/or third parties. The intellectual property rights of the author or third parties in respect of this work are as defined by The Copyright Designs and Patents Act 1988 or as modified by any successor legislation.

Any use made of information contained in this thesis/dissertation must be in accordance with that legislation and must be properly acknowledged. Further distribution or reproduction in any format is prohibited without the permission of the copyright holder.

Abstract

This research aims to investigate whether nanoforces on a substrate surface is an important factor in the attachment of anchorage dependent cells. If proven true, the outcome will lead to a convenient methodology to design and assess the surface of biomaterials. This research not only expands the understanding of cell attachment but also has the potential to preview how well cells can attach to a surface conveniently.

The first part of the project explores the mechanical properties of living cells. A series of atomic force microscopy (AFM) indentation experiments were carried out on MC3T3 cells (an osteoblast precursor cell line) under different conditions. Hertz and Johnson-Kendall-Roberts (JKR) contact models were applied to fit the force-displacement data. Increased time-dependent adhesions were observed by adding pausing time intervals of 1 second to 30 seconds between the AFM tip approaching and retracing processes. The effect of different AFM tip geometries/materials on cell indentation was studied by utilising different AFM probes, including polystyrene colloidal tips (PSC), borosilicate glass colloidal tips (BGC), titanium coated polystyrene colloidal tips (TIC) and parabolic tips (CSC17). Different adhesion behaviours between the tips were obtained and discussed.

A series of experiments were conducted to test the correlation between the surface nanoforces and initial cell attachment under different experimental conditions. The surface nanoforces of several treated glass samples were acquired by AFM and were compared to *in vitro* cell attachment data for four different cell types: MC3T3, chicken tendon fibroblasts (CTF), mouse endothelial cells (MEC) and bone marrow stromal cells (BMSC). The MTT assay, a colorimetric assay for assessing cell metabolic

activity, was utilised to assess the viable cell numbers. The correlation between nanoforces and cell attachment were evaluated qualitatively by figure plotting and quantitatively by statistical regression. Surface forces for typical biological materials were also obtained and compared with the data presented in the published literature. The results showed a general correlation between cell attachment and the surface adhesion force under serum-free conditions.

To further examine the hypothesis and explore the potential of materials in biological applications, two new graphene composite materials were investigated through a series of tests. The manufacturing processes of a graphene platelet composite of alumina ceramic ($\text{Al}_2\text{O}_3/\text{GPL}$) and a porous three-dimensional graphene foam (3DGF) were described, and the mechanical properties of these enhanced materials were assessed using various techniques. After an evaluation of their mechanical properties, *in vitro* cell seeding experiments were carried out using MC3T3 cells and BMSCs. Then the biological results were assessed using the MTT assay and fluorescence microscopy. The performance of the two materials and their potential biological applications were discussed. Finally, cell attachment data were compared to surface adhesion and was found to validate the correlation between surface adhesion and cell attachment further.

In conclusion, different AFM probes generated different adhesion forces, and the adhesion forces on the cell surface generally increase with longer setpoint pausing intervals. Regarding the mechanical properties of cells, the JKR model and Hertz model both yielded a reasonable elastic modulus for cells, although the JKR model could better model the adhesive retraction force curves. In the correlation between the measured surface characteristics and cell attachment, the surface adhesive force was found to be the most important factor in serum-free culture. The test results from the limited test conditions and data extracted from the literature matched the hypothesis

well; however, more data is needed for a wider range of cells, materials, and surface topographical features to validate the hypothesis further. Similar tests are recommended for future work. For the graphene-enhanced materials, Al₂O₃/GPL and 3DGF foam showed enhanced mechanical properties and the potential to be applied in biomedical applications. An empirical methodology using AFM to simplify the assessment of cell attachment on biomaterials has been initially tested, and initial cell attachment data was found to correspond to surface adhesion force changes.

Dedication

This thesis is dedicated to my adorable wife, Dr Xi Li. She has always been there for me with love and trust.

To my parents, Mr Qihai Yang and Ms Yanli Sun, my sister Shuangying Yang, my parents-in-law Mr Jianguo Li and Ms Linxia Ren; the family is the most important thing in my life.

Acknowledgements

I would like to take this opportunity to express my deepest gratitude to my supervisor Professor Kyle Jiang, for his professional guidance and support during my PhD study. Like a father to his son, he was very patient when teaching me the basic knowledge and techniques required at the start of this degree; when I made mistakes through the journey he pointed me in the right direction with trust and support; when I felt doubtful and frustrated, he kept inspiring me to move forward and be brave enough to accomplish tasks that looked impossible to conquer. He has set an outstanding example for me, on not only about how people should work hard to establish a career but also how people should live their life.

Next, I would like to thank Dr James Bowen and Dr Neeraj Jumbu for providing essential training, guidance, and support enabling me to conduct experiments in this research project. Their patience, professionalism and enormous knowledge in the research area helped me to solve problems countless times, and without their help, I would not have finished my experiments.

Colleagues in the Mechanical Engineering Micro/Nano group, including Dr Jian Liu, Dr Sunan Deng, Dr Guang Pu, Dr Guanxiong Wang, Dr Aydin Sabouri, and Dr Nasim Mahmoodi amongst others provided not only friendly advice and experiences during my PhD life but also resources and academic contacts which made collaborative work possible. The technicians, Miss Becky Charles and Mr Adam Sheward, performed a highly professional job keeping all the equipment running smoothly. The work in Chapter 5 was carried out in collaboration with Dr Jian Liu who manufactured ceramic composites, which is much appreciated.

The TRAILab group at the University of Birmingham led by Professor Liam Grover are also thanked for facilitating all the biological experiments in this project. The suggestions and discussions with Dr Richard Williams, Dr Gurpreet Chouhan, Dr Sophie Cox, Miss Alexandra Iordachescu and Miss Niusha Nikravesch were invaluable in my experimental design and planning.

Dr Xinyao Zhu from the University of Warwick provided great help, and we had critical discussions on the analysis of the AFM data on living cells.

Oxbridge Proofreading is thanked for helping edit and proofread this thesis.

The Mechanical Engineering Department of the University of Birmingham provided the financial support for this PhD project, and their research facilities have been indispensable.

Finally, I would like to express my sincerest gratitude to my family; my parents, my parents-in-law, my sister, and especially my beloved wife Dr Xi Li, for their continuous support and love. My good friends gave me friendship and encouragement, which together have made this journey the most valuable experience of my life.

Table of Contents

Abstract	i
Dedication	iv
Acknowledgements	v
Table of Contents	vii
List of Figures	xi
List of Tables	xvi
List of Abbreviations	xvii
Chapter 1 - Introduction	1
1.1 The Research Topic	1
1.2 Aims and Objectives	2
1.3 Structure of the Thesis	3
Chapter 2 - Literature Review and Background Information	5
2.1 Introduction.....	5
2.2 Biocompatibility	5
2.2.1 Definition and a Brief History	5
2.2.2 Research Outcomes related to Biocompatibility	8
2.3 Cell Attachment and Adhesion	15
2.3.1 Factors Affecting Cell Attachment and Adhesion.....	16
2.3.2 Serum-Free Cell Culture	17
2.4 Nanoforces in Cell Culture	19
2.4.1 Van der Waals Forces	20
2.4.2 DLVO forces.....	22
2.4.3 Steric, Ligand-Bond and Depletion Forces.....	24
2.4.4 Experimental Techniques for Measuring Sub-Micro-Newton Forces.....	25

2.5 Atomic Force Microscopy	26
2.5.1 Mechanism of AFM.....	26
2.5.2 AFM Working Modes.....	30
2.5.3 AFM Applications in Biological Research.....	31
2.6 Summary	35
Chapter 3 - AFM Measurements of Live Cells	36
3.1 Introduction.....	36
3.2 Methodology	39
3.2.1 Cell Preparation	39
3.2.2 AFM System Setup.....	39
3.2.3 Different AFM Tips and Tip Modification.....	42
3.2.4 AFM Measurement of Cells in Aqueous Solutions.....	44
3.2.5 Fitting the Data to the Hertz and JKR Models.....	44
3.3 Results and Discussion	48
3.3.1 AFM Tests on Live Cells.....	48
3.3.2 Effect of Indentation Pausing Time	54
3.3.3 Effect of Different AFM Tips.....	57
3.4 Summary	61
Chapter 4 - Correlation between Surface Nanoforces and Cell Attachment.....	64
4.1 Introduction.....	64
4.2 Methodology	65
4.2.1 Sample Preparation	66
4.2.2 AFM Testing.....	70
4.2.3 Cell Preparation and Culture.....	73
4.2.4 MTT Assay	74

4.2.5 Statistical Analysis.....	76
4.3 Results and Discussion	77
4.3.1 Treated Glass	77
4.3.2 Cell Attachment of Other Cell Types	85
4.3.3 Initial Cell Attachment on Treated Titanium Samples	87
4.3.4 Tests of Other Biomaterials	93
4.4 Summary.....	97
Chapter 5 - Cell Attachment to Graphene Composite Materials.....	100
5.1 Introduction.....	100
5.1.1 Background to Graphene Composite Materials.....	101
5.1.2 Alumina Ceramic and Graphene Platelet.....	102
5.1.3 Tissue Engineering Scaffold and 3D Graphene Foam.....	104
5.2 Methodology	105
5.2.1 Fabrication Process for the Al ₂ O ₃ /GPL Composite.....	105
5.2.2 Fabrication of 3D Graphene Foam	108
5.2.3 Measurement of the Mechanical Properties and Microstructure Characterisation of Al ₂ O ₃ /GPL.....	109
5.2.4 AFM Indentation of 3DGF and Al ₂ O ₃ /GPL	109
5.2.5 Cell Culture.....	111
5.2.6 <i>In vitro</i> MTT Assay	112
5.2.7 Fluorescence Microscopy	113
5.3 Results and Discussion	114
5.3.1 Enhanced Mechanical Properties and <i>In vitro</i> Experiments of Al ₂ O ₃ /GPL Composites.....	114
5.3.2 Mechanical Properties and <i>In vitro</i> Biocompatibility of 3DGF	125

5.3.3 Empirical Methodology for Early Assessment of Initial Cell Attachment on New Materials.....	131
5.4 Summary of the Chapter	134
Chapter 6 - Conclusions and Future Work	136
6.1 Thesis Conclusions	136
6.2 Future Work.....	138
References.....	140

List of Figures

Figure 2.1: Annual number of published articles referring to ‘biocompatibility’, from 1970 to 2016	7
Figure 2.2: A schematic of the DLVO interaction between two charged surfaces in aqueous solutions	23
Figure 2.3: Surface-bound and free coils of polymer chains in solution	24
Figure 2.4: A schematic of atomic force microscopy	27
Figure 2.5: Different types of AFM tip geometry	28
Figure 2.6: Schematic of an AFM artefact caused by tip geometry	28
Figure 2.7: Single molecule force spectroscopy experiments to unravel the nanomechanics of biomolecule adhesions	34
Figure 3.1: Schematic of (A) single molecule force spectroscopy and (B) single cell force spectroscopy	37
Figure 3.2: JPK NanoWizard®II atomic force microscopy system	40
Figure 3.3: NanoWizard®II AFM head and schematics of the AFM system	40
Figure 3.4: Cantilever holder with an AFM tip and a schematic of a CSC17/NO AL cantilever.....	41
Figure 3.5: SEM images of an AppNano® SICON-TL-BSG-A colloidal tip (left) and MikroMasch® HQ CSC17/NO AL silicon parabolic tip (right)	42
Figure 3.6: Schematics of stress distributions of the Hertz, JKR and DMT models during compression.....	46
Figure 3.7: AFM tests performed on different cellular locations and typical force-displacement curves	49
Figure 3.8: Examples of how the Young’s modulus changed with different indentation depth for the (a) nucleus zone and (b) cytoplasm zone	51

Figure 3.9: Example of curve fitting using the JKR model (left) and the Hertz model (right)	53
Figure 3.10: Comparison of the Hertz and JKR model fitting for the cytoplasm zone ..	53
Figure 3.11: Schematics of the pausing time interval experiments	54
Figure 3.12: Tip-sample adhesion on the nucleus zone and cytoplasm zone for different contact pausing times.....	55
Figure 3.13: A typical force- displacement curve for the cytoplasm zone showing molecule binding breaks on the retraction curve	56
Figure 3.14: Hertz fitted modulus for the nucleus zone and cytoplasm zone with different pausing times.....	57
Figure 3.15: Typical force-displacement curves for a CSC17 tip indenting an MC3T3 cell.....	58
Figure 3.16: Averaged tip-sample adhesion results using TIC and PSC tips with different pausing times.....	59
Figure 3.17: Hertz and JKR model fitting results for measurements with different tips	60
Figure 3.18: JKR fitting work of adhesion compared to the pull off force	61
Figure 4.1: Modification of a 6-well cell culture plate to test treated glass samples.....	67
Figure 4.2: Effects of ethanol treatment and UV treatment on PDMS cell attachment .	68
Figure 4.3: AFM measurement of the hydroxyapatite layer deposited onto treated Ti with a measurement area of $2\ \mu\text{m} \times 2\ \mu\text{m}$	70
Figure 4.4: AFM tip, MikroMasch HQ csc17/no Al	71
Figure 4.5: Schematic of how the sample surface was scanned by AFM	72
Figure 4.6: An example of force- displacement curves as measured using the AFM contact mode.....	72

Figure 4.7: Example AFM topographical measurements of a graphene composite material	73
Figure 4.8: Formazan crystals dissolved in MTT solution	75
Figure 4.9: Example MTT calibration curve for CTF cells	76
Figure 4.10: EDS results for the chemical composition of treated glass sample surfaces	77
Figure 4.11: Adhesion forces and surface roughness of glass samples	78
Figure 4.12: Cell number calculation for the glass samples	79
Figure 4.13: Surface attraction force and cell attachment percentage for treated glass samples.....	80
Figure 4.14: Surface adhesion force and cell attachment percentage for treated glass samples.....	81
Figure 4.15: Surface adhesion energy and cell attachment percentage for treated glass samples.....	81
Figure 4.16: Surface roughness and cell attachment percentage for treated glass samples	82
Figure 4.17: Surface adhesion forces when treated glass samples were immersed in DMEM and associated cell attachment data.....	84
Figure 4.18: Surface adhesion forces and cell attachment of MC3T3, MEC and CTF on treated glass samples.....	85
Figure 4.19: Surface adhesion forces and cell attachment of BMSC on treated glass samples.....	86
Figure 4.20: SEM images of the treated titanium surfaces.....	88
Figure 4.21: AFM measurements of the surface adhesion force and surface roughness of treated titanium samples	89

Figure 4.22: Surface characteristics of the alkali treated Ti surface.....	90
Figure 4.23: Surface characteristics of alkali-heat treated Ti surface.....	91
Figure 4.24: Surface adhesion force and cytolysis of rat bone marrow cells seeded on Ti and alkali treated Ti surfaces	93
Figure 4.25: Surface adhesion forces and initial cell attachment percentage of MC3T3, MEC and CTF on PDMS and glass surfaces	94
Figure 4.26: Initial cell attachment of NHGF and MG63 cells on PS and Ti surfaces, compared with surface adhesion forces	95
Figure 4.27: Surface adhesion forces and initial cell attachment of osteoblasts on hydroxyapatite and Ti	96
Figure 4.28: Surface adhesion forces and initial cell attachment percentage of MC3T3 on PDMS and alumina surfaces.....	97
Figure 5.1: Schematic diagram of the manufacturing process for Al ₂ O ₃ /GPL.....	105
Figure 5.2: SEM images of raw materials before mixing.....	106
Figure 5.3: SEM images of the GPL/ Al ₂ O ₃ powder mixture	107
Figure 5.4: Sintered and polished Al ₂ O ₃ /GPL samples	107
Figure 5.5: Images of 3DGF samples	108
Figure 5.6: Schematic of the Hertz Contact Model	110
Figure 5.7: Fluorescence microscopes used in this study	114
Figure 5.8: SEM images of sintered and polished ceramic surfaces	115
Figure 5.9: Grain sizes of GPL/Al ₂ O ₃ composites matrices.....	116
Figure 5.10: Surface topography of Al ₂ O ₃ /GPL measured by AFM indentation.....	117
Figure 5.11: GPL exposure on Al ₂ O ₃ /GPL composites surfaces.....	119
Figure 5.12: Surface mechanical properties of Al ₂ O ₃ /GPL composites with different GPL concentrations.....	120

Figure 5.13: MTT results for different ceramics composites using serum-supplemented culture medium	121
Figure 5.14: Fluorescence microscopy images of BMSC present on the sample surfaces	123
Figure 5.15: Live/dead cell counts of BMSC on ceramic composites.....	124
Figure 5.16: Viable MC3T3 cell attachment on Al ₂ O ₃ /GPL composites using non-serum culture medium	125
Figure 5.17: AFM surface topographical measurement of a 3DGF rim structure.....	127
Figure 5.18: Overview of Young's modulus for common biological materials.....	128
Figure 5.19: Fluorescence microscopy images of MC3T3 cells attached to the outer layer of 3DGF (left) and the nickel template (right).....	129
Figure 5.20: Fluorescence microscopy images of MC3T3 cells growing inside the 3DGF matrix	130
Figure 5.21: Live/dead cell count inside 3DGF and Nickel foam matrix.....	130
Figure 5.22: Surface adhesion forces and initial cell attachments on GPL/Al ₂ O ₃ composites	132
Figure 5.23: Surface adhesion forces and cell attachment on 3DGF vs. nickel foam ..	133

List of Tables

Table 2.1: Notable historical tissue engineering research outcomes	14
Table 2.2: Van der Waals interaction potential $E(D)$ and force $F(D)$ between macroscopic bodies with different geometries	21
Table 2.3: Electric double-layer interaction potential $E(D)$ and force $F(D)$ between macroscopic bodies with different geometries	22
Table 2.4: Characteristic length scales and typical orders of magnitude for non-covalent interactions of biomolecules and biomolecular assemblies	25
Table 3.1: Properties of different AFM probes.....	43
Table 3.2: Differences between the Hertz, JKR, and DMT models	46
Table 3.3: Mechanical properties of MC3T3 cells as measured by AFM indentation...	52
Table 4.1: PDMS reaction with different chemicals after immersion	67
Table 4.2: Statistical correlation between the tested surface parameters and the independent variable cell attachment.....	84
Table 5.1: Biomedical applications of ceramics and composites	103
Table 5.2: Flexural strength and fracture toughness of Al_2O_3 /GPL composites with different compositions of GPL	118
Table 5.3: Mechanical properties of 3DGF by AFM indentation.....	126

List of Abbreviations

3DGF	Three-Dimensional Graphene Foam
AFM	Atomic Force Microscopy
Al ₂ O ₃	Alumina
BFP	Bioforce Probe
BMSC	Bone Marrow Stromal Cell
BGC	Borosilicate Glass Colloidal Tip
CCL	ATCC [®] CCL [™] Cell Line
CO ₂	Carbon Dioxide
CSC17	Parabolic Tip
CTF	Chicken Tendon Fibroblast
CVD	Chemical Vapour Deposition
DL	Double-Layer (force)
DLVO	Derjaguin, Landau, Verwey, and Overbeek force
DMEM	Dulbecco's Modified Eagle's Medium
DMT	Derjaguin–Muller–Toporov (contact model)
DNA	Deoxyribonucleic Acid
ECM	Extracellular Matrix
EDS	Energy Dispersive Spectroscopy
F-D	Force-Displacement (curve)
FAK	Focal Adhesion Kinase

FBS	Foetal Bovine Serum
FDA	US Food and Drug Administration
FeCl ₃	Iron (III) Chloride
GAG	Glycosaminoglycan
GPL	Graphene Platelets
HA	Hydroxylapatite
HCl	Hydrochloric Acid
HEPES	4-(2-Hydroxyethyl)-1-Piperazineethanesulfonic Acid
hMSC	Human Mesenchymal Stem Cell
JKR	Johnson-Kendall-Roberts (contact model)
MC	Microfiber Cantilever
MEC	Mouse Endothelial Cells
MEM	Minimum Essential Medium
MEMS	Microelectromechanical Systems
MPA	Micropipette Aspiration
MTT	3-(4,5-Dimethylthiazol-2-yl)-2,5-Diphenyltetrazolium Bromide
NaOH	Sodium Hydroxide
OT	Optical Tweezers
PBS	Phosphate-Buffered Saline
PDMS	Poly-Di-Methyl-Siloxane, silicone
PI	Propidium Iodide

PMMA	Poly(Methyl Methacrylate)
PS	Polystyrene
PSC	Polystyrene Colloidal Tip
PTFE	Polytetrafluoroethylene
PVC	Polyvinyl Chloride
RICM	Reflection Interference Contrast Microscopy
RMS	Root Mean Squared (roughness)
RNA	Ribonucleic Acid
SCFS	Single Cell Force Spectroscopy
SMFS	Single Molecule Force Spectroscopy
SEM	Scanning Electron Microscopy
SFA	Surface Force Apparatus
SFD	Shear Force Detachment
SMFS	Single Molecule Force Spectroscopy
TIC	Titanium Coated Polystyrene Colloidal Tip
TiO ₂	Titanium Dioxide
TIRM	Total Internal Reflection Microscopy
UV	Ultraviolet Light
VDW	Van der Waals (force/interaction)

Chapter 1 - Introduction

1.1 The Research Topic

This PhD project presents the investigation of whether the surface nanoforces of substrates play an important role in cell attachment. This investigation was inspired by a literature review, and carefully planned experiments were conducted for a variety of different test conditions as will be described.

Initially, a study of the mechanical properties of live cells was performed using atomic force microscopy (AFM) indentation, which utilised various test parameters and several AFM probes. Live cells' adhesive behaviour was demonstrated through a series of experiments using different cells, different substrate materials, and under different test conditions to initially test the hypothesis. The results were presented both qualitatively and quantitatively in the study. Afterwards, an empirical methodology, which used AFM to assess the initial cell attachment ability of a material, was proposed based on the hypothesis. This methodology was utilised to estimate the initial cell attachment on two novel graphene composite materials: graphene platelet composite alumina ceramic ($\text{Al}_2\text{O}_3/\text{GPL}$) and 3D porous graphene foam (3DGF). Mechanical properties and *in vitro* cell attachment of these two graphene-enhanced materials were examined.

The outcomes of this research could contribute to a convenient approach for evaluating or estimating how well cells can attach to a substrate. The design and test process of biomaterials could be improved in a cost and time-efficient manner. The correlation between surface adhesion and cell attachment can be used in combination with other technologies to enable better control of cell attachment, and therefore affect subsequent cell activities. AFM and the contact model curve fitting techniques used in this study on

both organic and inorganic samples are useful for other research areas, as well as the findings for the two novel graphene composite materials. Al₂O₃/GPL and 3DGF could potentially be used in biological applications as supportive implantation structures and tissue engineering scaffolds although this would require further validation.

1.2 Aims and Objectives

This PhD project aimed to investigate the hypothesis that surface nanoforces are important in initial cell attachment, and then to utilise this outcome for the easy assessment and estimation of cell attachment to substrates.

To achieve the aims of this research project, several objectives were established:

- Review and understand the cell attachment and adhesion process. Understand and practice how to assess cell performance on different substrates.
- Review and understand the intermolecular forces presented during different stages of biological applications. Understand and practice how to measure material surface force properties using AFM.
- Design and carry out AFM indentations on live cells. Study the properties and interactions of cells with different AFM probes under different test conditions. Examine and compare different contact mechanics models on biological materials.
- Design and carry out experiments to establish whether there is a correlation between the overall surface intermolecular adhesion force and cell attachment.
- Compare the findings from this research with the results from existing publications to test the proposed hypothesis.
- Study the development of graphene composite materials. Use the developed methodology to predict the initial cell attachment ability of these materials.

- Test the performance of graphene composite materials in biological applications.
Compare initial cell attachment results with the predicted outcome.

1.3 Structure of the Thesis

The thesis consists of six chapters, including this introductory chapter. It presents the research carried out between September 2012 and December 2016 and includes the motivation, background study, experimental design, experimental work undertaken, and discussions of the results.

Chapter 2 presents a review of the literature for background knowledge. Fundamental theories and research outcomes are presented, such as the process of cell attachment and adhesion, factors affecting cell adhesion, intermolecular interactions under cell culture conditions, Derjaguin, Landau, Verwey, and Overbeek (DLVO) theory, van der Waals (VDW) force etc. The current status of related research topics and other researchers' work are also detailed, and various scientific equipment and techniques which are utilised in this study are introduced. AFM has been extensively used during this project to detect surface properties, such as surface adhesion forces and surface roughness, and thus greater attention is paid to AFM. The fundamental mechanism of AFM testing, its applications in biological cell measurements, and its strengths and limitations are discussed.

In Chapter 3 the results of a series of AFM indentation experiments performed on live cells are detailed. Force-displacement (F-D) curves of different testing conditions and with different probes are presented. Hertz and Johnson-Kendall-Roberts (JKR) contact models were applied and the results analysed and compared. Different contact time and different AFM tips were utilised in order to observe the reactions of the cells.

Chapter 4 presents an investigation of the hypothesis that was conducted to test whether the surface nanoforces of a substrate were the dominant factor affecting the initial cell attachment ability within the serum-free cell culture. The investigation was demonstrated by comparing the initial cell attachment results with surface adhesion data under various conditions. Mouse osteoblast precursor cells, mouse endothelial cells, chicken tendon fibroblasts and mouse bone marrow stromal cells were selected for these experiments, together with several substrates, including silicone, polystyrene (PS), alumina ceramic, glass and treated glass, titanium (Ti) and treated Ti. A literature survey was conducted to support the study from a broader perspective.

Chapter 5 describes two novel graphene composite materials which were tested, with mechanical measurements acquired using various testing rigs, and the results were discussed and compared with conventional materials. *In vitro* cell seeding experiments were performed to investigate whether these new materials can be used in biological applications. Attached cells were assessed via an MTT assay and observed by fluorescence microscopy. The surface nanoforces of new materials were measured and compared with the initial cell attachment results to validate the correlation proposed in Chapter 4.

In the final chapter, the research conclusions are presented. The contributions of the findings to the research area are discussed, as well as the limitations, before suggestions for future improvements are proposed.

Chapter 2 - Literature Review and Background Information

2.1 Introduction

In this chapter, the background to this research is presented. It begins with a fundamental definition, history and development of biocompatibility, where it is revealed that the term biocompatibility refers to a general description of how biomaterials function in specific applications. Thus the focus is placed on the process of cell attachment, which is a critical step in the life cycle of anchorage dependent cells. A brief introduction to the different phenomena which occur during the process of cell attachment and adhesion is then presented, together with the differences between serum supplemented cell culture and serum-free cell culture. This is followed by a literature survey of different factors that affect cell attachment and adhesion. A review of the work undertaken by other researchers found that limited work has been conducted on nanoforces, which are an important factor which affects various physical and chemical reactions. Therefore nanoforces in cell culture conditions are discussed, with a focus on the DLVO force. Finally, the main technique used in this research project is introduced in detail, and a basic explanation of the principle of AFM, different detection modes and different AFM applications are presented.

2.2 Biocompatibility

2.2.1 Definition and a Brief History

The term biocompatibility was first proposed in 1970 by Homsy (1), and it quickly drew great attention and became an important research sub-discipline. Originally, biocompatibility was a concept widely used in biomaterials science to describe the

interactions between human tissues and materials used as implantable devices which were designed to remain inside a human body for a long period (2). Generally speaking, the basic requirements for materials in biological applications are non-toxic, non-immunogenic, non-thrombogenic, non-carcinogenic and non-irritant. To date, many materials have been tested as biomaterials in different situations. For example, between the 1940s and 1980s chemically inert metals were utilised as the first generation of implantable materials. Initially plain carbon and vanadium steels were used and then later stainless steel, and Ti alloys were widely adopted as they had improved corrosion resistance. Different types of polymers, such as nylons and polyesters were tested but were later replaced by polytetrafluoroethylene (PTFE), poly(methyl methacrylate) (PMMA) and silicones to control chemical degradation.

The development of biomaterials also reflects the increased in-depth understanding of biocompatibility. In the early years, the only requirement for a 'biocompatible' material was to maintain its mechanical strength without causing harm to a patient. Later, it was found that even though a 'compatible' biomaterial that performs designed functions very well within a specific tissue, would inevitably cause some negative side effects when inside the human body, which could ultimately make it a failure in other applications. It is important to note that biocompatibility is a complicated subject and is correlated to each specific tissue type, and thus a modern definition of biocompatibility has been proposed by Williams (3) which emphasises the case-dependent nature of biocompatibility: 'the ability of a material to perform with an appropriate host response in a specific application.'

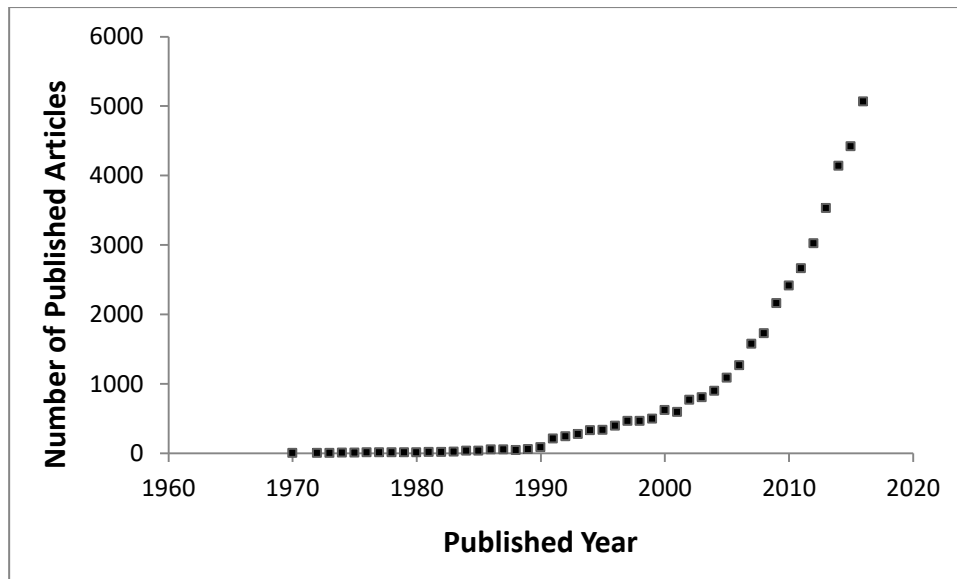


Figure 2.1: Annual number of published articles referring to ‘biocompatibility’, from 1970 to 2016

(Data from Web of Science™)

With a more practical and better understanding, biocompatibility can be summarised under three specific points. The word ‘appropriate’ indicates that the specific materials and mechanism selected should be individual for a specific tissue, organ or cells in specific situations. For example, the effect of implantable medical devices are considered to differ from patient to patient (3), and there are many variables that need to be taken into account, such as age, sex, general health and concurrent disease, physical mobility, and lifestyle (4). The relationship between the design of devices and a patient’s condition has an important role, and the presence of micro-organisms and endotoxins also need to be considered (5-7). Furthermore, the increasing number of applications has highlighted the reactions of devices with tissues rather than individual cells, which cannot be ignored. Through greater consideration of these reactions, biomaterials can be tested more thoroughly in a similar environment in order to avoid unnecessary incompatibility. Finally, it is now being admitted that it is impossible to create a perfect biomaterial which does not degrade, and instead, the focus is on how to control degradation over time inside the human body.

Biocompatibility is mainly concerned with the complicated process of how a host responds to a material during the entire device lifecycle. It relates to both biomaterials and living tissue, and the continual problems and challenges. For example, materials and tissue function both separately and when integrated, and consequently the interface between them is critical. Protein adsorption and desorption, platelet adhesion, foreign body giant cell reactions and immune cell responses need to be considered at the interface. The stability of implanted materials inside a patient is also important, as material degradation can result in the loss of the functionality of a device, which may cause difficulties regarding removal and disposal. Furthermore, the degradation process may also influence the surrounding tissues by interacting with cells or organs, both temporarily or permanently. Both of these situations are crucial for biocompatibility, and even pose a threat to life. In addition, biomaterials are normally implanted into a body which already has diseased organs or cells, and so it is difficult to control or predict changes to tissues following the implantation of biomaterials. The response of a host may initially be positive; however, host deterioration can cause a series of negative effects, not only to the tissues nearby but also associated with other cell-material and molecule-material interactions. One of the worst negative scenarios for a biomaterial following implantation is it leading to the formation of tumours, which can be caused by chemical carcinogenicity, fibrosis and chronic inflammation.

2.2.2 Research Outcomes related to Biocompatibility

In this section, a summary of the research outcomes for biocompatibility relating to different biomaterials, associated tissues and applications is presented. The first part is concerned with the biocompatibility of different materials, since previous research has focused on the principles/mechanisms of biocompatibility. The second part of this

section summarises biocompatibility in specific biomedical applications, and the research focused on how to solve related issues in these applications.

2.2.2.1 Biocompatibility Tests on Different Materials

Extensive research on biocompatibility has focused on exploring the relationship between biological reactions and the properties of materials, both bulk properties of the material as a whole and the micro/nano-properties of local areas.

Anderson (8) reviewed how living tissues react with foreign materials and evaluated the biocompatibility of materials through *in vivo* testing. Johnson et al. (9) performed a series of *in vitro* tests using 12 standardised cell lines against 20 materials and concluded that four cell lines (CCL 1 mouse connective tissue, CCL 74 raccoon uterus, CCL 76 human skin and CCL 131 mouse neuroblastoma) had an obvious toxic reaction to polyvinyl chloride (PVC, Sn stabilised). There are some reports that the stiffness of a substrate affects cell behaviour (10-12), while others believe that it is crucial to monitor biodegradation processes, i.e. residuals or ions peeling off from the bulk material after being in contact with body fluids, especially in tissue engineering (13, 14). There is some evidence that the surface electrical charge mixing into an electrolyte (15, 16) affects how cells grow.

The influence of surface topography on biocompatibility is another important consideration, and surface roughness has been reported to have an impact on cell growth (17). By utilising nano-fabrication technology, Washburn et al. (18) discovered that osteoblasts sense a difference in the surface root mean square (RMS) roughness ranging from 0.5 to 13 nm. Organised surface structures, both on the micro and nanometre scales, have been extensively studied using fast-moving micro-/nano-manufacturing technology. The effect of the surface pattern size has been studied for

seeding cells onto fabricated surfaces with specific structures. Observations on a larger scale have revealed that cells attach and grow better on nanometre features rather than micrometre ones (19-23). The interactions of cells with a TiO₂ nanotube diameter ranging from 15 to 100 nm showed that cells adhere to smaller nanotubes much better than to larger nanotubes, while the latter tended to lead to a dramatic reduction in cellular activities and cause a high level of programmed cell death (24, 25).

The experimental results on polymer demixed nano-islands by Dalby et al. (26, 27) showed that islands shorter than 30 nm increased cell adhesion, while islands taller than 30 nm decreased it. Andersson et al. (28) reported that fibroblasts react to photolithographically fabricated columns, with a width between 58 and 166 nm, with wider columns resulting in a better distribution of cells. Brammer et al. (29) and Seunghan et al. (30) also noted better elongation and differentiation of stem cells on larger TiO₂ nanotubes compared to smaller ones. Structures with different shapes (31-36), different arrangements (37), and different feature densities (38, 39) have also been investigated with the intention of determining the best conditions for the growth of various cells. Unfortunately, no conclusions could be drawn.

The effects of surface treatments on biocompatibility have also been studied. Usually, the surface treatment has focused on only a few chemical reactions between the surface groups and proteins involved in cell culture. The most well-known example is the treatment of plastic surfaces for either enhancing (40-43) or prohibiting (44-46) cell growth. Ti and its alloys are popular bone replacement materials and are often treated with alkali before undergoing a heating process in order to promote osteogenesis (47). The treatment of glass surfaces has been tested to improve the attachment of HeLa cells by Nordling et al (48). The early work of Rappaport (49) explored how to increase mammalian cell growth on treated glass surfaces, by increasing the surface charge and

surface Na⁺ ion concentration. Countless patents have been filed on novel materials or treatment methods concerning biocompatibility, and some have been shown to enhance the biocompatibility of biomaterials in designated applications; however, the reasons why some of the methods work are not fully understood. In addition, it has been observed that different cell species react differently under the same experimental conditions (50-54).

2.2.2.2 Biocompatibility Research on Biomedical Devices

Initially, biomaterials were intended to be implanted into the human body for long periods of time. Following several decades of development, it remains an important research topic to maintain the long-term performance of devices for the replacement of damaged or diseased tissue. For example research on joint replacement has focused on total joint replacement prostheses for more than 40 years. In the early 1970s mechanical properties, such as material fatigue, creep strength, toughness and wear-resistance, were examined in biocompatibility studies to maximise long-term stability and minimise material ageing (2). After consideration of the balance between mechanical properties and material degradation, metallic components were determined to be the best materials for long-term implantable devices, and Ti alloys and cobalt-chromium alloys are both good candidates due to their excellent and fast attachment to bone and precise surface chemistry (55, 56).

Aside from metallic materials, polymers are also a good candidate for this application; however, it has been reported that the release of polymer wear debris induces inflammatory cells to produce osteoclasts, leading to a negative impact on bone resorption (57). Inflammatory cells may be observed during the late stage of degradation many years after the original implantation (58), and similar problems have been reported in polymer-based drug delivery systems (59). Consequently,

biodegradation has to be taken into consideration, since material degradation can lead to loss of structural integrity, and degradation products may affect the tissues. The mechanism of polymer degradation, reason and location in causing inflammation within local tissue remains unclear. Recent interest has been focused on polymers with nanoparticles, for example, instead of using microspheres, nanospheres with a diameter of 100 nm or less are investigated for drug delivery (60). The increase of research on nanoparticle-based polymers has led to a better understanding of their degradation and biocompatibility.

Ceramics have excellent wear resistance for use in joint replacement, and it has been found that adding ceramic oxidation components into a biomaterial can improve wear resistance and minimise osteolysis (61). Currently, the research frontier of biological ceramic technology is bioactive ceramics, which unlike traditional inert materials, are designed to actively react with the tissues they are in contact with and thus together perform vital activities. Some ceramic-based bioactive compounds, such as hydroxyapatite, calcium phosphates and glass, can be synthesised and used as a coating to cover metallic materials to enhance wear-resistance, bone bonding and minimise material fatigue (62-64). Many applications for tissue engineering and drug delivery have adopted this method, but only Ti and cobalt-chromium alloys and hydroxyapatite are suitable for bioactive coatings, and the stability of these materials is excellent in the kinetics of bone adaptation (65, 66).

Aside from joint replacement, synthetic materials are also commonly applied in ophthalmology. For example, standard cataract treatment involves the implantation of artificial intraocular lenses (67), and thus biocompatibility research has examined test lenses made of PMMA, silicone and acrylic (68, 69). Another ophthalmological

treatment involves synthetic corneas, which have been developed and tested to ease the shortage of human cornea donation (70, 71).

Regarding cardiac implantations, biomaterials and surface treatment technology are continually being developed to improve degradation and compatibility, for example, the covering on pacemaker leads (72, 73), stents (74, 75) and heart valves (76, 77).

2.2.2.3 Tissue Engineering

Tissue engineering is ‘the creation of new tissue for the therapeutic reconstruction of the human body, by the deliberate and controlled stimulation of selected target cells through a systematic combination of molecular and mechanical signals’ (2). Compared to the inert implants discussed above, where most artificial systems are restricted to non-viable replacements for diseased tissue, tissue engineering is very different. Implantable and degradable materials can only solve physical problems or mechanical defects, while tissue engineering therapy facilitates the regeneration and repair of defective tissues/organs. In the process of tissue regeneration, other biomaterials are usually involved which aid in refining the shape of the tissue or providing external stimulation signals. In this process, the biomaterials involved are important, as they need to be designed to stimulate the cells/tissue they are in contact with. Preferred bioactive materials should progressively degrade and dissolve as new tissue forms, through a process which is different from inert materials. A better understanding of the biodegradation of materials in tissue engineering is therefore urgently required. Both conventional synthetic biomaterials and natural biopolymers can be good candidates for tissue engineering applications, for example, individual proteins such as collagen (78), elastin (79) and silk (80), polysaccharides such as hyaluronan (81), alginate (82) and chitosan (83), and natural tissue-derived materials (84, 85), together with some engineered forms or derivatives of such substances (86).

Even though this is a relatively new field, there have been many successes related to tissue engineering and regenerative medicine. The first tissue-based materials to be developed were used in skin grafting techniques in 1962 (87), although the first successful tissue-based skin products were produced during the 1970s and 1980s, which signified the start of a new era in modern tissue engineering. To date, the most commonly developed engineered tissues are skin, cartilage and liver. Some historic landmarks in tissue engineering are listed in Table 2.1 to provide an overview of this rapidly developing topic.

Table 2.1: Notable historical tissue engineering research outcomes

Year	Technology and accomplishment	Ref
1962	Ivalon sponge developed as a ‘synthetic substitute for skin’ by Chardack	(87)
1975	<i>In vitro</i> cultivation of keratinocytes by Rheinwald and Green	(88)
1979	Cultured autologous epithelium, later commercialised as Eqicel by Genzyme	(89)
1981	Composite living skin equivalent by Bell, later commercialised as Apligrad by Organogenesis	(90)
1982	Collagen-glycosaminoglycans (GAG)-based dermal matrix by Yannas, later commercialised as Dermal Regeneration Template by Integra Life sciences	(91)
1987	‘Tissue engineering’ term firstly mentioned by Y.C. Fung	(92)
1988	Cell transplantation in synthetic biodegradable polymers	(93)
1994	Chondrocyte culture and transplantation by Brittbery, later commercialised as Carticel by Genzyme	(94)
2006	Artificial bladder cultured <i>in vitro</i> and implanted <i>in vivo</i>	(95)
2008	Engineering trachea from de-cellularised matrix seeded with human cells derived from stem cells	(96)
2013	Artificial beef burger produced and eaten by Mark Post	(97)
2016	First artificial pancreas approved by the FDA	(98)

More recently, several ground-breaking new technologies have been developed which have had a significant impact on tissue engineering. These new technologies are mainly focused on combining nano-manipulation and micro/nano-fabrication technology to

tissue engineering materials, scaffold generation, and stem cell technologies. For example, microfabrication and microelectromechanical systems (MEMS) have been utilised to enable the precise and ultra-fine control of the size and complexity of the *in vivo* environment (99, 100).

2.3 Cell Attachment and Adhesion

Cell attachment and adhesion is an important process that plays a critical role in various physiological processes which subsequently occur. Attachment refers to the process of floating cells adhering to a solid substrate and developing anchoring structures, such as focal adhesion complexes. Attachment and adhesion rely on the interactions between different cells and their surrounding environment. In most biological applications cells are required to bond to inorganic biomaterials, for example metals, alloys, polymers and ceramics in bone replacement treatments. On the contrary, for some other applications, such as contact lenses, cells must not adhere and attach to the material. Thus cell adhesion and attachment to material is an essential point to consider. Cell attachment and adhesion mechanisms are not fully understood, but a summary is provided here in order to provide a better understanding to this basic unit of living creatures, and also to help design and manufacture artificial materials/devices to function better.

When cells approach a surface, there are three main factors which induce adhesion: a bridging system, electrostatic interactions, and long-range forces. Bridging is the most common method which results in cell adhesion, and it acts by absorbing one molecule to another. Some macromolecular bridges require the help of electrostatic forces if their range is half the length of the bridging molecule, since electrostatic attractions enable two surfaces with opposite charges to attract each other and adhere. This type of interaction has been reported by several scientists, including Bierman (101) and

Deryagin (102). Alternatively, long-range forces may result in attractions which lead to cell adhesion, but these are dependent on the magnitude and range of attraction and also repulsion forces (103).

Three common experimental approaches are typically used to investigate and assess cell adhesion strength. The first approach studies the conditions when attachment and adhesion are broken and assesses why this has occurred, while the second examines the formation of stronger attachments and adhesions. It is important to pay attention to the vital activities of cells and tissues following adhesion, such as the morphology of adhesions between cells and biomaterials.

2.3.1 Factors Affecting Cell Attachment and Adhesion

As discussed earlier, mechanical properties, including bulk properties and surface properties, are generally relevant to performance in a biological system and artificial system functionality. Most mammalian cells are anchorage-dependent cells (104); therefore cell adhesion and attachment is the first step towards any vital activities. There is no doubt that material properties affect the biological cells and tissues they are in contact with through their impact on cell adhesion and attachment.

Surface roughness is correlated to interfacial energy and the wettability of a surface, which affects cell adhesion and attachment. The interfacial adhesive force, which is proportional to the contact area, is also affected by surface roughness. Thus, surface roughness needs to be increased in order to optimise the contact between cells and materials, and it determines the tissue reaction at the interface and influences cellular activities. It has been found that increasing surface roughness and the presence of fibronectin can promote cell adhesion, allowing cells to spread and proliferate on Ti surfaces (105). Surface topography was studied in cell culture before the 1990s and was

found to have an influence on cell adhesion, attachment, growth and orientation. Microscopic surface texturing has been used for a long time, for example in the pre-treatment of a sample via etching, and has a significant influence on the surface area of an interface (106). Surface stiffness is also an important feature of the cellular microenvironment (107), and its effect depends on the cell type, as cortical neuron cells need to be attached to a soft gel substrate but not astrocytes (108). In some more complicated scenarios complex stiffness is used to describe when cells sense the stiffness of both soft and rigid surfaces (109).

2.3.2 Serum-Free Cell Culture

Cell culture is one of the most basic techniques used in the cellular function and molecular studies. In the early 1930s, scientists began to develop complex biological sera for culturing and analysing cells. *In vitro* experiments usually involve the use of serum-supplemented cell culture medium, mostly to provide hormonal proteins and polypeptides for stimulating cell growth, proliferation and differentiation. Minerals and trace elements are also important in some of cell life cycle processes, and serum proteins function as transporters, such as globulin and albumin, while others act as facilitators in cell attachment and spreading, such as fibronectin, vitronectin and collagen. The most widely used serum is foetal bovine serum (FBS), while other common sources are new-born calf serum, horse serum and human serum. The serum selection is based on cell type and medium base type. However, there are a few issues associated with serum supplemented cell culture:

1. There are hundreds of constituents within serum, and the precise composition of serum remains unknown. Let alone the specific consequences due to the various components (110, 111). Complexity in serum composition leads to product variance

between different manufacturers. Usually, the variance cannot even be eliminated batch to batch from the same manufacturer. This variance generates inconsistency in the experimental results obtained by different researchers or even between repeats of experiments by the same researcher (112, 113).

2. For most *in vitro* cell cultures, animal serum supplemented culture will not be the same as the *in vivo* physiological conditions, as the stimuli present in the serum are different to those a cell would naturally respond to; thus serum could cause different reactions for different cell types.

3. Some serum components may be toxic, prohibit cell growth or cause cell apoptosis. Also, serum could potentially be contaminated with viruses, mycoplasma or bacteria during the manufacturing process (114-116).

4. Ethical concerns and the cost of the mass production of serum from animals are also the subject of much debate, but are beyond the scope of this research.

5. In serum-supplemented cell culture, protein adsorption on both the cell surface and the substrate surface cannot be ignored. This is a complex and dynamic process which is highly dependent on the physicochemical conditions and the properties of the surface, such as pH, ion concentration, surface energy, etc. Various intermolecular interactions play an important role in this process, including VDW forces, hydrophobic forces, hydrogen bonds, steric repulsion and electrostatic interactions, etc. Additionally, biological processes, such as the conformational change of a protein and protein-receptor bond, are also occurring concurrently.

To explore the physical factors of cell attachment the use of the serum-free medium is an option to study cell adhesion and attachment without too many specific biological interactions being involved.

2.4 Nanoforces in Cell Culture

Within a biological system, biological interactions are often different due to simple chemical reactions or a physical change to a system, which is due to the high complexity of biological macromolecules and the systems involved. Instead of a linear relationship, biological interactions contain competing interactions, branching pathways and feedback loops. (117) It is also important to note that these interactions are 'dynamic' rather than 'static' since biological environments are never in a state of thermodynamic equilibrium. For example, integrins are a very important transmembrane protein and play a critical role during the cell life cycle as a result of biological interactions. Through receptor-ligand interactions, integrins connect adhesive proteins to the extracellular matrix (ECM) and cytoskeleton inside the cell membrane, and these biological interactions of integrins also function as a signal pathway. For example, when the extracellular domain of an integrin binds to ECM proteins, a structural change occurs to the cytoplasmic domain, which can lead to a change to interactions with other cytoplasmic proteins, such as focal adhesion kinase (FAK) which then could trigger a signal cascade.

Complicated biological processes are constructed of simple elemental interactions between biomolecules, which are the same as the intermolecular interactions between inorganic molecules and widely exist between cells, macro bodies and charged molecules. These forces are often known as non-specific interactions, for example, VDW forces, electrostatic force, steric hindrance and thermal fluctuation. These forces

can be attractive or repulsive, depending on the geometry, temperature and local concentrations.

2.4.1 Van der Waals Forces

VDW forces, named after the Dutch scientist Johannes Diderik van der Waals, were originally described in physics in relation to the interaction between atoms, molecules and surfaces. VDW forces can be broken down into three parts: the force between permanent dipoles (Keesom force); the force between a permanent dipole and a corresponding induced dipole (Debye force); and the force between instantaneously induced dipoles (London dispersion force). A dispersion force exists between any atoms and molecules (118) and is caused by the fluctuations in the electric dipole moments of molecules which become correlated when molecules come closer. In essence, this is an attractive force, just like when two rotating magnets become aligned and are attracted to each other. The VDW interaction between two molecules can be calculated based on the separation D , as described below:

$$E(D) = -C_{VDW}/D^6 \quad (2.1)$$

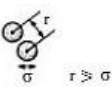
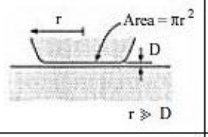
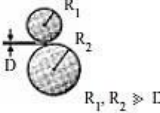
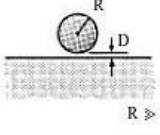
In equation 2.1, the VDW constant C_{VDW} depends on the properties and geometry of the interacting bodies, and the force can be attractive or repulsive. Many scientists have contributed to the development of the mechanism of action of VDW forces. Hamaker (119) derived the VDW interaction between macroscopic bodies using the ‘Lifshitz theory’. The equations are described regarding the Hamaker constant, A , which for two bodies 1 interacting across a medium 2 is given by:

$$A = \frac{3}{4} kT \left(\frac{\epsilon_1 - \epsilon_2}{\epsilon_1 + \epsilon_2} \right)^2 + \frac{3h\nu_e}{16\sqrt{2}} \frac{(n_1^2 - n_2^2)^2}{(n_1^2 + n_2^2)^{3/2}} \quad (2.2)$$

In which A is determined by the properties of the interacting bodies, ϵ_1 , ϵ_2 are dielectric constants and n_1 , n_2 are refractive indexes. The value of the Hamaker constant is typically in the range of $5-10 \times 10^{-20}$ J for non-conducting solids and liquids interacting in a vacuum or the air. For interactions in an aqueous medium such as water, the Hamaker constants are typically an order of magnitude smaller.

Table 2.2: Van der Waals interaction potential $E(D)$ and force $F(D)$ between macroscopic bodies with different geometries (120)

How to calculate the VDW energy and the VDW force in four typical geometries. Negative values in E and F indicate that the interaction is attractive.

Geometry of bodies with surfaces D apart ($D \ll R$)		van der Waals interaction	
		Energy, E	Force, F
Two atoms or small molecules		$-C_{VDW}/r^6$	$-6C_{VDW}/r^7$
Two flat surfaces (per unit area)		$E_0 = -A/12\pi D^2$	$-A/6\pi D^3$
Two spheres or macromolecules of radii R_1 and R_2		$\frac{-A}{6D} \left(\frac{R_1 R_2}{R_1 + R_2} \right)$	$\frac{-A}{6D^2} \left(\frac{R_1 R_2}{R_1 + R_2} \right)$ Also $F = 2\pi \left(\frac{R_1 R_2}{R_1 + R_2} \right) E_0$
Sphere or macromolecule of radius R near a flat surface		$-AR/6D$	$-AR/6D^2$ Also $F = 2\pi R E_0$

The equations to calculate VDW forces and energies are presented in Table 2.2, where VDW interactions in some common geometries are listed, for example, two small molecules, two flat surfaces or two spherical bodies interacting with each other, or the interaction between a sphere and a flat surface.

2.4.2 DLVO forces

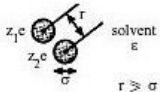
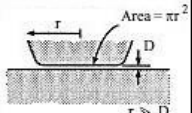
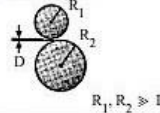
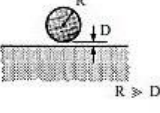
In addition to VDW forces, another force which commonly occurs between two molecules or surfaces within aqueous solutions is the electric ‘double-layer’ force (DL). DL forces together with VDW forces led to the DLVO theory of colloid stability by Derjaguin and Landau (121), Verwey and Overbeek (122). The long-range electrostatic interaction energy between two similar molecules or surfaces can be approximately calculated as:

$$E(D) \approx + C_{ES} e^{-\kappa D} \quad (2.3)$$

Where C_{ES} is a constant value dependent upon the geometry of the interacting surfaces, surface charge densities and solution conditions.

Table 2.3: Electric double-layer interaction potential $E(D)$ and force $F(D)$ between macroscopic bodies with different geometries (120)

How to calculate the DL energy and the DL force in four typical geometries. Constant Z is determined by solution condition, temperature, concentration of electrolytes and surface charge density.

Geometry of bodies with surfaces D apart ($D \ll R$)		Electric double-layer interaction	
		Energy, E	Force, F
Two ions or small charged molecules		$+ \frac{z_1 z_2 e^2}{4\pi\epsilon\epsilon_0 r} e^{-\kappa(r-\sigma)}$	$\frac{+ z_1 z_2 e^2 (1 + \kappa r)}{4\pi\epsilon\epsilon_0 r^2 (1 + \kappa\sigma)} e^{-\kappa(r-\sigma)}$
Two flat surfaces (per unit area)		$(\kappa/2\pi) Z e^{-\kappa D}$	$(\kappa^2/2\pi) Z e^{-\kappa D}$
Two spheres or macromolecules of radii R_1 and R_2		$\left(\frac{R_1 R_2}{R_1 + R_2} \right) Z e^{-\kappa D}$	$\kappa \left(\frac{R_1 R_2}{R_1 + R_2} \right) Z e^{-\kappa D}$
Sphere or macromolecule of radius R near a flat surface		$R Z e^{-\kappa D}$	$\kappa R Z e^{-\kappa D}$

The value $1/\kappa$ is the Debye length, which is dependent on the solution conditions, temperature and concentration of electrolytes. The DL force between macromolecules of different geometries is summarised in Table 2.3. In an aqueous solution, van der Waals and DL forces usually occur together; thus DLVO theory is commonly used to describe the net interaction of two surfaces. Figure 2.2 illustrates the relationship between these two forces and the resulting net force.

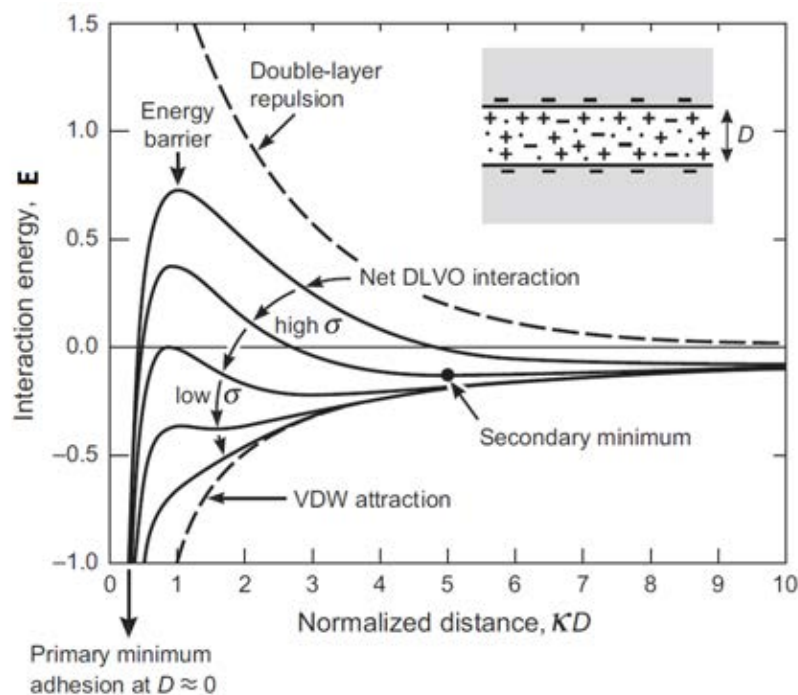


Figure 2.2: A schematic of the DLVO interaction between two charged surfaces in aqueous solutions (120)

This figure demonstrates how the DLVO interaction changes with distance D between two surfaces. The two dashed lines represent the double-layer repulsion (above the x-axis) and the VDW attraction (below the x-axis) alone. Solid lines represent the DLVO interactions with different surface charge densities σ . X and Y axis are in arbitrary units.

In Figure 2.2 it can be seen how the attractive VDW and repulsive electrostatic DL forces act together to determine the total interaction potential between two charged surfaces in an aqueous electrolyte solution at different surface charge densities σ or potentials ψ . The actual magnitude of the energy E is proportional to the particle size (radius) or interaction area (between two planar surfaces). The DLVO theory has been

found to adequately describe the long-range forces between similarly charged colloidal and some bio-colloidal surfaces within aqueous solutions.

2.4.3 Steric, Ligand-Bond and Depletion Forces

Polymer-like groups are commonly used and exposed on biological surfaces within an aqueous environment. Regardless of whether chains are attached to the protein surface, the presence of these polymers normally dominates the interaction forces between two surfaces. Steric forces exist between surfaces containing bound coils when they are approaching each other within an aqueous solution. A surface-bound polymer may contain functional groups along its chain or a specific ligand bond at its free end. When a guest molecule or membrane approaches a host and exposes binding sites for these functional groups, then a ‘bridging’ attraction can result between the two structures once they are sufficiently close for some initial binding to occur, as shown in Figure 2.3.

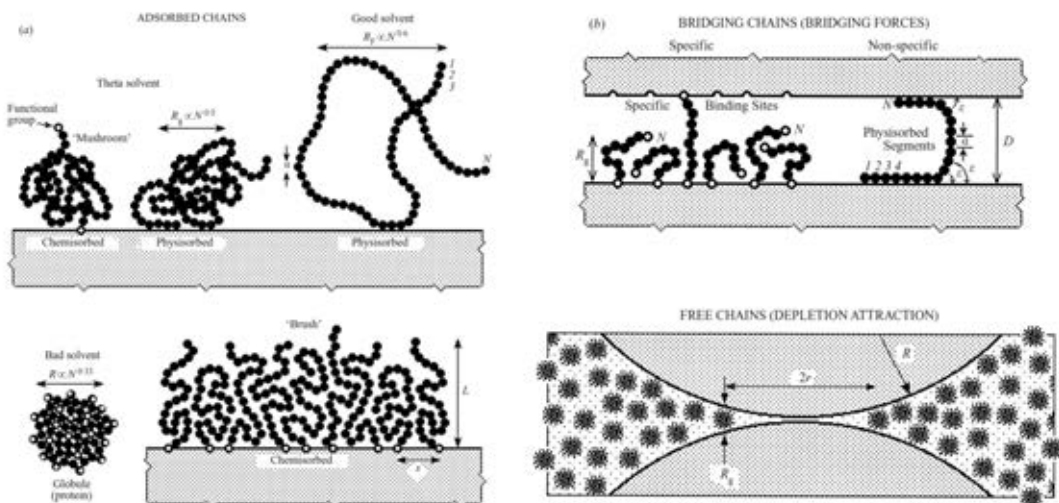


Figure 2.3: Surface-bound and free coils of polymer chains in solution (117)

(a) The binding to a surface can be via chemical bonds (chemisorption) or physical bonds (physisorption). (b) The forces between such surfaces can be attractive or repulsive or both, i.e. attractive at large separations but repulsive at small separations or vice versa.

A depletion force arises when polymers are free in aqueous solution, such as when they are not adhered or attached to a surface. As reported by Boni (123), depletion forces are

widely used in biomedical experiments to form ‘hybrid’ cells. This force arises from the osmotic pressure between the bulk solution that contains a concentrated polymer and the ‘depletion zone’ of radius r between the two surfaces that are free of polymer.

2.4.4 Experimental Techniques for Measuring Sub-Micro-Newton Forces

There are many techniques for measuring sub-micro-Newton forces between two surfaces, a surface and a molecule, and two molecules. The most common method is the measurement of the direct force and the energy of interaction, while other methods, such as measuring surface deformations, molecular rearrangements, conformational and structural changes, can also provide insights on the micro-scale.

Table 2.4: Characteristic length scales and typical orders of magnitude for non-covalent interactions of biomolecules and biomolecular assemblies (117)

Typical ranges and strengths of interaction energies and forces for undeformed particles in aqueous 0.15M NaCl solutions are shown. The effective range of an interaction is defined as the distance at which the interaction energy is of the same order as the thermal energy kT , where the thermal energy kT is the product of the Boltzmann constant, k , and the temperature, T . kT is often used in physics as a unit of energy for molecular scale systems, and at 25 °C, $kT \approx 4.11 \times 10^{-21}$ J.

Parameters measured	Bonds, molecules and sub-molecular groups	Nanoscale surfaces and macromolecules	Microscopic surfaces and small particles	Macroscopic (flat) surfaces and large particles
Typical surface or particle radius	0.1 nm	1 nm	1 μ m	1 mm
Binding/adhesion energy	1 kT	10 kT	1000 kT	10 ⁶ kT 100 mJ m ⁻²
Adhesion force	10 pN	100 pN	100 nN	100 μ N 10 ⁸ N m ⁻²
Effective range of interaction	0.2 nm	2 nm	20 nm	50 nm
Suitable experimental techniques	OT, AFM & MC, MPA & BFP	OT, AFM (tip) & MC, MPA & BFP	OT, AFM (bead) & MC, MPA & BFP, TIRM & RICM, SFD	SFA, OP, RICM, SFD

Table 2.4 summarises the typical ranges and strengths of interaction energies and forces under different conditions, together with applicable experimental techniques. Different

techniques are suitable for measuring different parameters, for example, AFM is an ideal technique for bonds, molecules, nanoscopic and microscopic surfaces but not for macroscopic surfaces. Currently, surface forces apparatus (SFA) and AFM are the most commonly used techniques to detect and observe a range of surface forces and separations. The interactions between microscopic particles and cells are usually measured using micropipette aspiration (MPA), a bioforce probe (BFP), total internal reflection microscopy (TIRM), reflection interference contrast microscopy (RICM), AFM and shear flow detachment (SFD). Molecular-scale and single bond interactions are best measured using optical tweezers (OT), AFM, SFD, BFP and microfiber cantilever (MC) techniques.

2.5 Atomic Force Microscopy

In 1985 G. Binnig and C. F. Quate from Stanford University and Christoph Gerber from IBM Zurich Laboratories together established AFM (124), a scanning probe-type of microscopy that does not require conductive specimens. The surface of an object can be explored at very close distances by a probe the size of an atom, allowing surface details and characteristics to be distinguished at a higher resolution than with any other microscope. With modifications, AFM can also be used to determine the electrical, magnetic and mechanical properties of samples without incurring destructive damage. AFM has enabled the direct observation of the microscopic world.

2.5.1 Mechanism of AFM

Typically, AFM consists of three parts: force detection, position detection, and the feedback system, as shown in Figure 2.4.

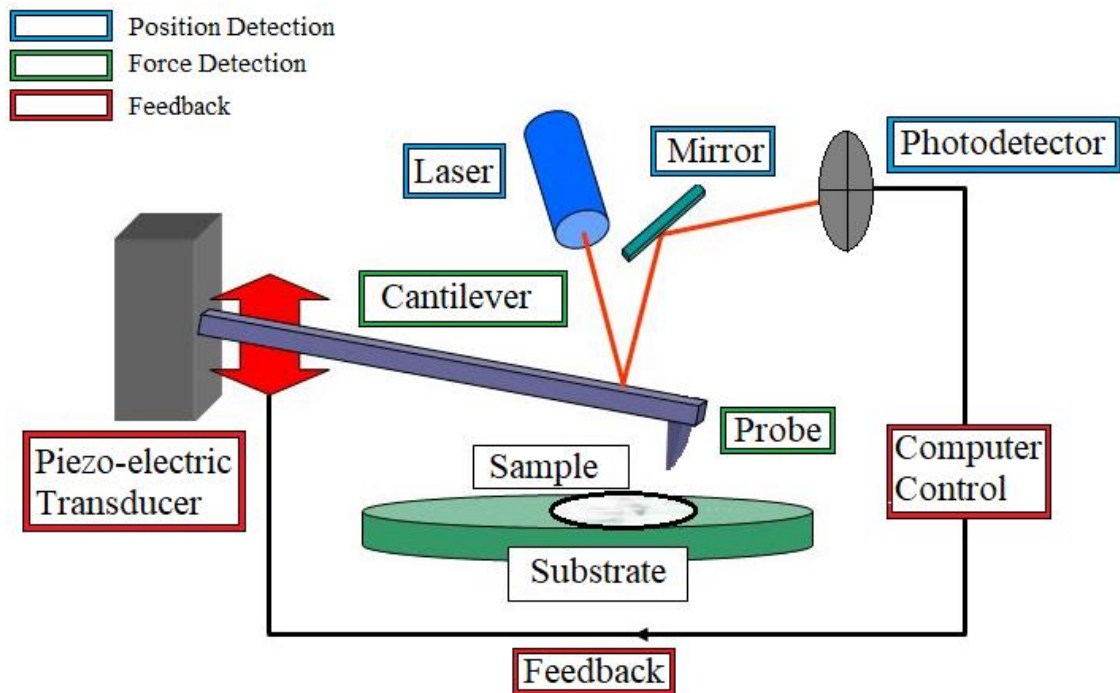


Figure 2.4: A schematic of atomic force microscopy (125)

In the general setup of an atomic force microscope, a probe is installed at the open end of a micro-cantilever beam. When the probe approaches a sample surface, atoms on the probe and the sample surface interact with each other via intermolecular forces. As a result, the micro-cantilever is slightly deformed. The force detection system is shown as green boxes in the figure. A laser beam is reflected from the back of the micro-cantilever to a photo-detector, which can accurately measure the slight deformation of the micro-cantilever. The position detection system is indicated by blue boxes. The deformation signals are recorded and sent to a feedback system (red boxes) which then adjusts the movement of the cantilever accordingly.

In AFM interactions between the tip and sample are detected using a cantilever, which typically consists of a silicon wafer or silicon nitride sheet 100 to 500 μm in length and approximately 500 nm to 5 μm thick (125). The cantilever length, width and material are selected according to the characteristics of the sample, the different operating modes and probe type. The tip of the micro-cantilever is used to interact with samples, and typical AFM tips with different geometries are shown in Figure 2.5.

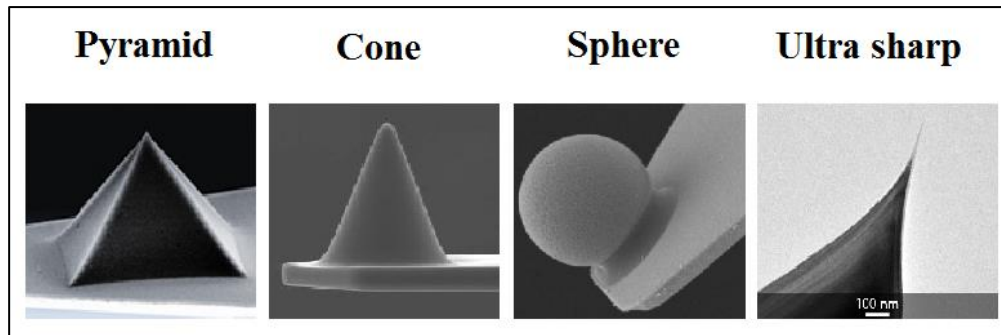


Figure 2.5: Different types of AFM tip geometry
(from manufacturer)

Which tip to use is case dependent, and sometimes an AFM tip needs to be functionalised for special measurements, such as surface metal coating for electrical measurements. Pyramid and cone shape tips are used for general applications and are widely manufactured around the world, while spherical tips are often used to study and quantify colloidal interactions. When soft samples, such as cells, are measured using the contact mode, spherical tips are preferred to prevent damage to the samples. An ultra-sharp tip is required for a high-resolution test, as the other tips will lead to artefacts, an example of which is illustrated in Figure 2.6. However, the cost is high, and the tip wears quicker than the other types.

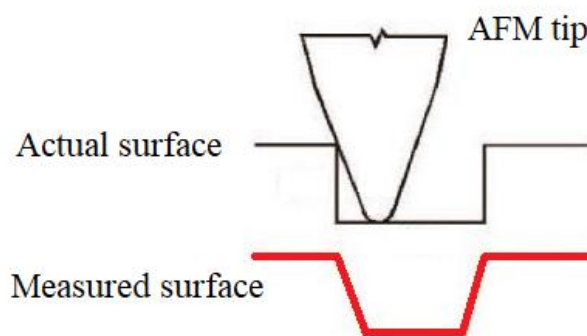


Figure 2.6: Schematic of an AFM artefact caused by tip geometry

The measurement is inaccurate because of the interaction between the sample surface and the side of the AFM tip.

The interaction between the tip and the sample causes the cantilever to deflect. A laser is positioned at the end of the micro-cantilever, meaning that the position of the reflection changes due to fluctuations of the cantilever leading to small displacements. A laser spot position detector is used to record the offset which is then converted into electrical signals for the controller, which is responsible for signal processing. The laser light focused on the micro-cantilever is reflected to the laser position detector, and by calculating the intensity of the four quadrants falling on the detector, the size of the micro-cantilever deformation due to the surface topography can be obtained, resulting in detailed information on the surface of the sample.

The signal is taken up by the laser detector and treated as a feedback signal in the feedback system as an internal adjustment signal. This is driven by the voltage created in a ceramic tube to determine the appropriate movement to maintain a specific force between the sample and the tip. The AFM system uses piezoelectric ceramics to precisely control tiny scanning movements; these are a specific form of functional electro-ceramics. When an electric field is applied to a piezoelectric ceramic, it will be deformed longer or shorter in a specific direction, and the deformation dimension is linearly related to the magnitude of the applied voltage. In other words, a small deformation can be controlled by the change in voltage applied to a piezoelectric ceramic. In general, the three perpendicular directions of a piezoelectric ceramic, X, Y and Z, are composed of the shape of a tripod, and by controlling the X and Y directions, the probe can be driven to scan the surface of a sample, whereas by controlling the Z direction the distance between the probe and a sample can be controlled. In AFM the surface properties are obtained within these three directions.

2.5.2 AFM Working Modes

The working modes in AFM are classified by the force between the tip and a sample, and there are three main operating modes: contact mode, non-contact mode and tapping mode.

Contact mode is the most direct imaging mode in AFM. As described by its name, in this mode there is intimate contact through the repulsive force with the sample surface during the scanning process. During scanning the force exerted on the tip of the cantilever may damage the surface structure of a specimen, and normally, the working force is in the range of 10^{-10} to 10^{-6} N. However, if a sample surface is soft and cannot sustain such a force, then it is not appropriate to use the contact mode for sample surface imaging.

In the non-contact mode, the cantilever oscillates 5 to 10 nm above the surface of a specimen. The interaction between the sample and the tip is the attractive VDW force, which is approximately 10^{-12} N. Thus, a sample will not be damaged, and the tip will not be contaminated, which is especially appropriate for materials with very soft and delicate surfaces. The disadvantage of this mode is that it is difficult to achieve at room temperature because the surface of a sample inevitably accumulates a thin layer of water, which creates a small capillary bridge between the sample and the tip, and this results in the tip sticking to the surface and increases the pressure on the tip.

The tapping mode is a hybrid between the contact and non-contact modes, whereby the cantilever oscillates above the surface of a specimen at its resonant frequency, and consequently the tip only periodically contacts or strikes the surface of a sample. This results in a significantly reduced force which is generated when the tip touches a sample. Consequently, it is the best choice for detecting soft and delicate surfaces. When

scanning a sample in this mode, the device will input data into the system for surface analysis, such as surface roughness, average height, the maximum distance between peaks and peaks. At the same time, AFM can also complete force measurements and measure the degree of bending of the cantilever to determine the size of the force between the tip and the sample size.

The contact mode is the only mode where it is possible to achieve an ‘atomic resolution’ image of any vertical changes of hard samples due to the fast scanning rate. However, samples may be damaged, and a low-resolution image may be obtained due to adhesion between the tip and the sample due to the effect of an adsorbent layer on the surface of the sample. In the non-contact mode, no force is applied to the sample surface, but there is low resolution due to the separation of the tip from the sample and the low scanning speed compared to that in the tapping and contact modes. This mode is commonly used for samples which cannot get into contact with water. The non-contact mode is consequently used far less often than the two other two modes. The tapping mode is excellent regarding eliminating the impact of lateral forces and reducing the force caused by an adsorbent layer. Compared to the two other modes, the tapping mode can be used for any sample without damaging its surface in order to obtain a high-resolution image. The only limitation of the tapping mode is the relatively slower scanning rate compared to the contact mode.

2.5.3 AFM Applications in Biological Research

With the developments in measurement technology and equipment, life sciences have begun to develop rapidly regarding quantitative measurements. Most experimental work has focused on the relationship between biological macromolecules, especially the structure of nucleic acids and proteins, and their related functions. Using AFM the

image resolution for the surface of natural materials has been vastly improved, and subsequently, AFM has become one of the most important characterisation techniques for the study of biomedical and biological macromolecules. AFM is mainly used in three areas: the surface morphology of biological cells; the structure and functional properties of biological macromolecules; and to measure forces between different biological molecules.

2.5.3.1 AFM Probing of Cells

AFM is often used to observe the surface morphology of cells and to conduct image analysis. For example, changes to the surface morphology of cells following infection and the effect of free radical damage on the surface morphology of erythrocyte membranes can be directly observed by AFM. Quantitative scans can be achieved as well, such as surface area, thickness, width and the volume of cells.

AFM has been shown to not only generate ultra-high resolution cell images but also to detect the micromechanical properties of cells. Furthermore, AFM can be utilised to detect live cell dynamics and cell motility without requiring the pre-treatment of samples; this is the only characterisation technique which allows the detection of cells in near-physiological conditions. Using AFM direct imaging methods, it is possible to study living cells and subcellular structures. Detailed information on the structure of organelles, the cell membrane and the cytoskeleton can be obtained (125, 126). The cell membrane structure consists of folds, lamellar bodies, microfilaments, microvilli and other characteristics which could only be observed in fixed cells. Because the internal skeleton of a cell is covered by the cytoplasmic membrane, a new method for carefully removing this was also developed. One of the most important features of AFM in cell research is the real-time imaging of viable processes, which allows cell interactions to be observed in response to internal and external stimuli. AFM has also been used to

investigate the infection of cells by viruses (127, 128), to study changes in platelet shape when in their active state (129), and the gastric digestion of interfacial protein by enzymes (130).

2.5.3.2 AFM Imaging of Macromolecules

AFM has improved and significantly progressed protein research, where it has been utilised to observe the behaviour of a wide range of proteins, such as albumin, haemoglobin, and insulin. It has also been very useful for understanding bioactivity, *in vitro* cell growth, and protein and membrane purification. For example, Dufrene et al. (131) used AFM to investigate the assembly behaviour of collagen adsorbed to the surface of polymers, and Quist et al. used it to study the adsorption behaviour of albumin and porcine insulin on a mica substrate (132). Meanwhile, Evans et al. (133) have used AFM to study the detachment of agglutinin-bonded red blood cells, in which the ligand-receptor binding strength was assessed by pull-off experiments. In research on the purple membrane of bacteria, Müller et al. (134) visualised bacteriorhodopsin molecules with an impressive resolution of several nanometres.

2.5.3.3 The Force Spectrum between Biomolecules

The measurement of the various interactions of the cell surface biomolecules is a very important application of AFM. Intermolecular forces dominate many biological processes, including physiological, biochemical, and pathological phenomena, such as the opening or closing of ion channels, the binding or disintegration of receptors and ligands, enzyme function activation or suppression, etc. Therefore, the study of the interactions between biomolecules is essentially the most fundamental within the life science. In recent years single molecule force spectroscopy (SMFS), which is based on AFM, has been developed to measure forces and motions associated with biological molecules and enzymatic activity. In SMFS a biomolecule is fixed onto the AFM probe

tip, and then through pressing and pulling the AFM tip towards cells/surfaces/other molecules, the interaction between the attached molecule and the test objective is recorded as a set of data with force and distance. The F-D relationship is sometimes referred to as the force spectrum.

The force spectrum shows the interaction patterns between molecules, as well as the binding strength and the elastic properties of the molecule chain. Figure 2.7 shows some examples of how the force spectrum can have different patterns due to protein recognition, protein unfolding, protein unzipping and a protein spring. Applications of SMFS have been to study molecule binding and unbinding in various conditions, such as the unfolding of a protein (135, 136) and nucleic acids (137), while other applications include measuring the unfolding strength of fibrinogen in order to study the elastic properties of blood clots (138), studying DNA structure (139), antibody-antigen binding events (140), and cell adhesion (141) amongst others.

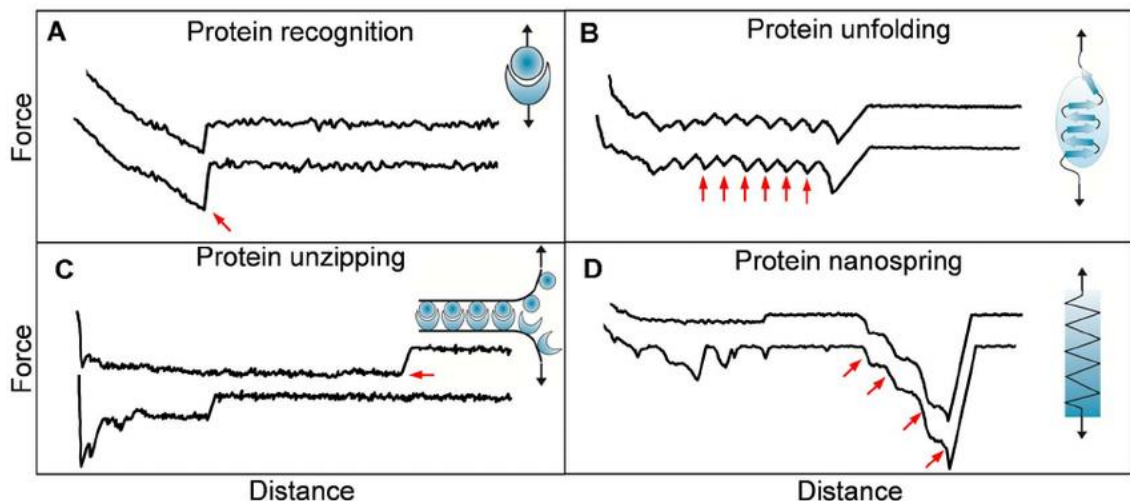


Figure 2.7: Single molecule force spectroscopy experiments to unravel the nanomechanics of biomolecule adhesions (142)

Series of F-D profiles obtained by stretching adhesins from various microbial species: (A) single adhesion peaks reflecting specific recognition; (B) saw-tooth patterns with multiple force peaks corresponding to the force-induced unfolding of protein secondary structures; (C) constant force plateaus originating from the mechanical unzipping of interactions between multiple adhesins; and (D) single large adhesion force peaks with linear pullback shapes. The arrows emphasise the characteristic force peaks in each case.

2.6 Summary

In this chapter, a summary of the literature on biocompatibility and intermolecular forces has been presented, which serves as a background introduction and provides theoretical support for the experimental work described in the following chapters.

A brief history and the development of biocompatibility, including the concept, different research areas, underlying principles, and examples have been discussed. Cell attachment and adhesion processes were briefly described, together with common factors which affect this process. The difference between serum containing and serum-free cell culture was also detailed. The intermolecular nanoforces present within the cell culture environment, including VDW forces, DL electrical force, and steric and ligand-receptor force have been briefly presented. Finally, AFM is used extensively in this project, and so its operating modes, advantages and disadvantages, and its applications in biological research have been presented and discussed.

Chapter 3 - AFM Measurements of Live Cells

3.1 Introduction

This chapter presents a study of the mechanical properties of living cells using the AFM indentation technique. The cytoskeleton of living cells, as well as their cytoplasm, membrane and numerous accessory proteins, determine the mechanical properties of cells. Consequently, they reflect the situation of these living cells. By investigating these characteristics a better understanding of the status of living cells and certain physiological processes can be achieved (143). Biomechanical scientists can also study certain diseases and identify potential solutions by investigating the mechanical properties of normal cells and then comparing with abnormal cells (144). Therefore it is meaningful to explore the various mechanical properties of cells, such as topography, elastic modulus, and surface adhesion force. The surface adhesion forces acquired in these experiments are of particular interest as they have a strong influence on cell attachment, which is essential for anchorage-dependent cells. Adhesion forces measured under different conditions are the first step to verifying the correlation between surface nanoforces and cell attachment.

The need to determine the mechanical properties of biomedical tissues has led to the appearance of a wide range of instrumentation for probing biological cells and molecules within appropriate environments. AFM, among other tools, is powerful for the study of soft biological samples under physiological conditions, since it can function within aqueous conditions with high spatial and force resolution. Various studies using AFM on cells have already been conducted, and AFM based techniques are continually developing. The most convenient approach to study the mechanical properties of cells is through direct indentation, which has been widely adopted and

used to investigate numerous biological sample surfaces, for example Li et al. (144), Cross et al. (145) and Faria et al.(146) have studied various cancer cell properties using this technique. Through the addition of actuators, AFM can also be used for micro-manipulation, and this technique has been applied to modify biological materials at the molecular level (147), to extract genetic material from chromosomes (148), and to deliver drugs at the molecular level (149). A set of special techniques, known as single molecule force spectroscopy (SMFS) and single cell force spectroscopy (SCFS) has emerged as an effective tool for investigating the interactions associated with specific biological molecules/cells.

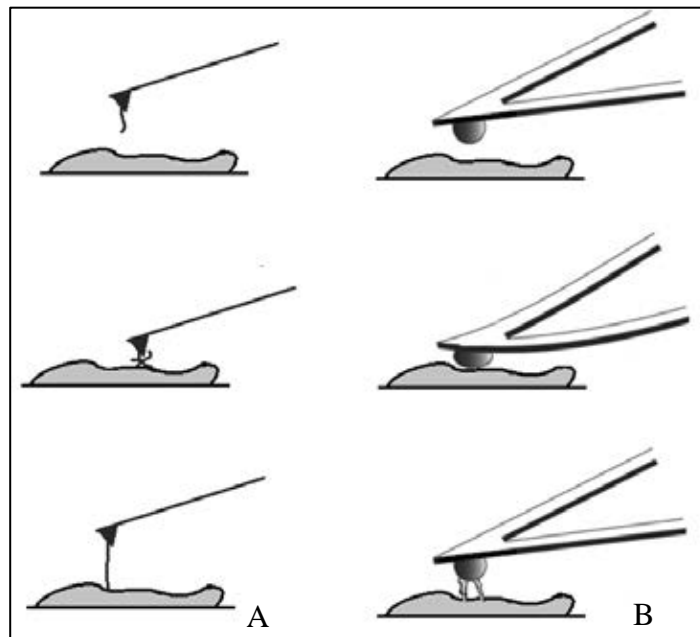


Figure 3.1: Schematic of (A) single molecule force spectroscopy and (B) single cell force spectroscopy

In SMFS, the AFM tip is functionalised by a designed molecule, which engages with the target sample to study interactive forces. In SCFS a cell is attached to a tipless cantilever. This is a powerful technique to study cell-cell interactions and how a cell reacts with its surroundings in a controlled environment.

As shown in Figure 3.1, both techniques require some modifications to traditional AFM equipment. The molecule or cell of interest, which can be living or frozen depending on the purpose of the experiment, is attached to a tipless cantilever that can then be used as

a functionalised AFM tip to interact with an object. Example applications include the research by Benoit et al. (150), Kedrov et al. (151), and Beaussart et al. (152).

The research presented in this chapter mainly focuses on the general mechanical properties of living cells and the way in which different parameters affect the measurements. The AFM direct indentation technique was adopted. By recording data when an AFM probe is pressing against a cell, the F-D relationship during the indenting and relaxing period was captured. A cell's mechanical properties can be calculated from contact mechanics models. The effect of different AFM tip geometries/materials on cell indentation were studied by using different AFM probes for cell indentation; the first type of tip used was a cone/parabolic tip constructed from n-type silicon, while the second type was a colloidal tip with a microsphere constructed from glass and polystyrene attached to the end of the cantilever.

Two contact mechanic models, the Hertz model and the JKR model were chosen to calculate the mechanical properties of the living cells, and the effect of applying different contact mechanic models on living cell measurements was discussed. The Hertz contact model has been widely adopted for calculating elasticity based on AFM indentation data by other researchers. During the experiments, the Hertz model was initially applied to fit the non-adhesive approaching curves. For the later measurements where relatively large colloidal AFM probes were applied, the JKR model was applied to study the indentation F-D curves, as the adhesive interaction between the tip and cell surface were non-negligible.

Finally, time-dependent adhesions were investigated by adding pausing time intervals between the AFM tip approaching and then retracting. Time intervals of 1 second, 10

seconds and 30 seconds were utilised in separate groups of experiments, and the resulting adhesion changes were then examined.

3.2 Methodology

3.2.1 Cell Preparation

MC3T3 cells, an osteoblast precursor cell line, supplied by TRAILab, University of Birmingham, were thawed from liquid nitrogen stocks. The thawed cells were from passage numbers 10 to 20, and were cultured in supplemented Dulbecco's Modified Eagle's Medium (DMEM) and incubated at 37°C in a humidified incubator with 5% CO₂. The cell culture medium consisted of the base DMEM (Sigma D6546), supplemented with 10% FBS, 2% L-glutamine (200mM, Sigma), 1% penicillin-streptomycin (10,000 units penicillin and 10 mg streptomycin per mL, Sigma) and 2.4% HEPES buffer (1M, Sigma). After fully recovering, the cells were detached using TrypLE™ Express (Gibco®), separated by centrifugation, and cultured in serum-free medium for a further 24 hours prior to the AFM investigation. During the AFM procedure, serum-free DMEM was added to the cell culture petri dishes in order to minimise the influence of serum proteins.

3.2.2 AFM System Setup

Cell surface characteristics data were acquired using a JPK NanoWizard®II Atomic Force Microscope system, and a TopViewOptics™ optical microscope system was integrated into the system to enable better control during the measurements. An overview of the AFM system is shown in Figure 3.2. The sample under test was fixed onto a sample holder and placed on top of the motorised precision stage (Figure 3.3), and the AFM probe was mounted on a glass cantilever holder using a special spring clip

(indicated by the black arrows in Figure 3.4), then the cantilever holder was installed into the AFM head.

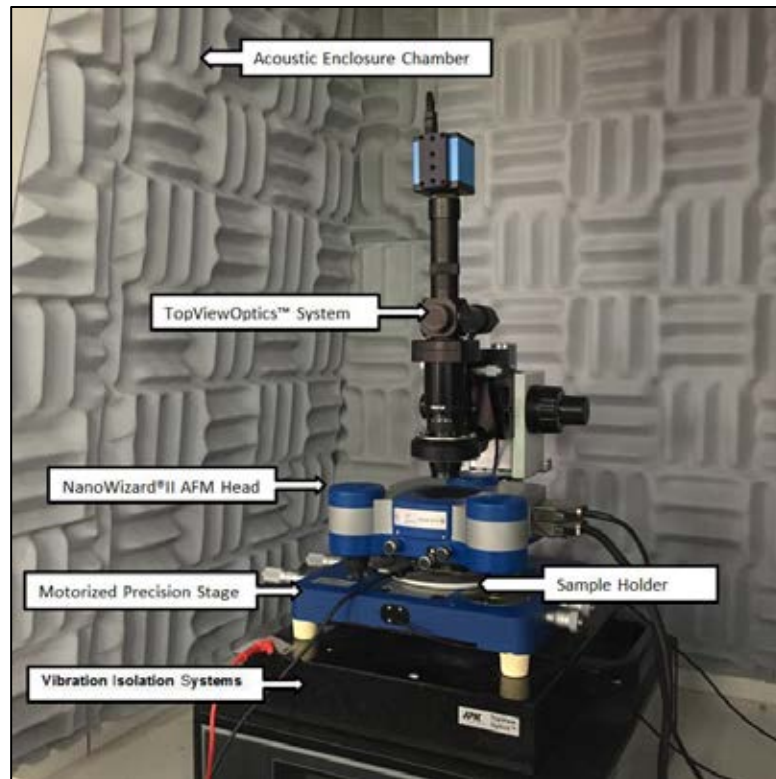


Figure 3.2: JPK NanoWizard®II atomic force microscopy system

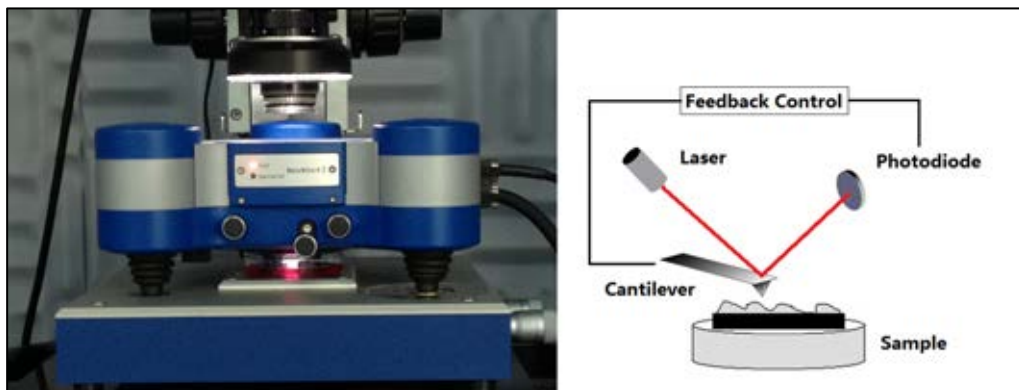


Figure 3.3: NanoWizard®II AFM head and schematics of the AFM system

The NanoWizard®II AFM head is the core element of this AFM system which contains a cantilever, laser, photodetector and feedback control system.

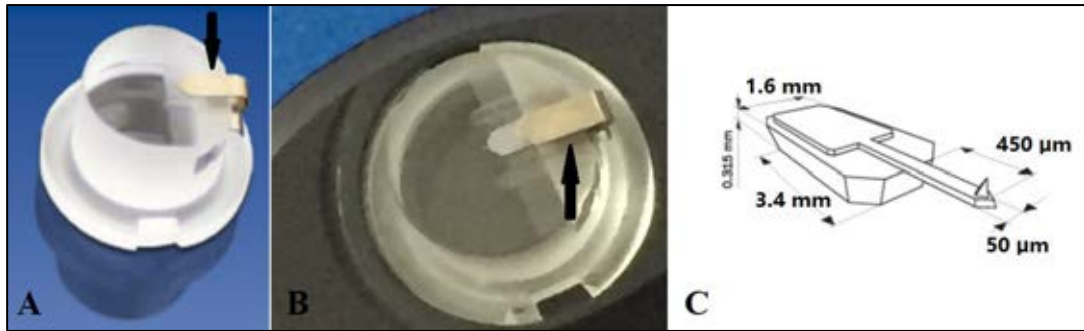


Figure 3.4: Cantilever holder with an AFM tip and a schematic of a CSC17/NO AL cantilever

(A) The transparent cantilever holder; the AFM cantilever is mounted via the spring clip indicated by the black arrow. (B) A close-up picture of an AFM cantilever mounted on the cantilever holder. (C) A schematic of the CSC17/NO AL cantilever from the manufacturer MikroMasch; the cantilever and the AFM tip in this figure are for illustration purposes and are not proportional to the real dimensions.

Movement of the AFM tip in the x-y-z directions was controlled by step motors and the piezo stage. The maximum scanning range of the machine was $100\ \mu\text{m} \times 100\ \mu\text{m}$ laterally, while the maximum vertical movement range was $90\ \mu\text{m}$. The laser beam was reflected off the back of the cantilever and then recorded. The surface interaction with the cantilever caused deflections to the cantilever, which led to a change in the direction of the laser beam. Thus the laser signal was collected and analysed in order to reveal the cantilever deflections. Combined with the cantilever's mechanical properties, the surface interaction with the cantilever was also acquired. During an AFM test the sample and the movement of the tip could also be simultaneously observed using the TopViewOptics™ CCD camera, which provided increased accuracy regarding the setup and relocation. Vibration isolation and the acoustic enclosure chamber were utilised in order to eliminate noise during the system's operation.

The contact mode of AFM was utilised in this chapter, whereby the scanning tip moved across the sample and the fixed end of the cantilever repeatedly moved up and down to maintain a constant compressive force. The test area in each measurement position varied from a $1\ \mu\text{m} \times 1\ \mu\text{m}$ square (to repeatedly test a local area) to a $50\ \mu\text{m} \times 50\ \mu\text{m}$

square (to obtain an overview of a cell's morphological information), depending on the test conditions. F-D curves and surface topographical data were collected and later analysed using JPK data processing software.

3.2.3 Different AFM Tips and Tip Modification

Two types of AFM probes were applied in this chapter: MikroMasch[®] HQ CSC17/NO AL parabolic tips and AppNano colloidal tips. Parabolic tips are pyramidal silicon etched probes manufactured by MikroMasch, with a tip radius of 8 nm and a cone angle of 40°. Colloidal probes were manufactured by AppNano Inc., and borosilicate glass microspheres (diameter 5.4 μm +/- 0.3 μm) and polystyrene microspheres (diameter 5.2 μm +/- 0.52 μm) were attached to silicon tipless cantilevers using high precision six-axis micro-manipulators with 1,000 \times optics. Examples of the tips are shown in the scanning electron microscopy (SEM) images presented in Figure 3.5 from the manufacturer's description documents.

In addition to purchased standard tips, a set of polystyrene colloidal tips was modified, whereby the microsphere of the colloidal tip was coated with a layer of Ti (thickness 5-10 nm) using the chemical vapour deposition technique, so that the interaction between a Ti surface and a cell surface could be mimicked.

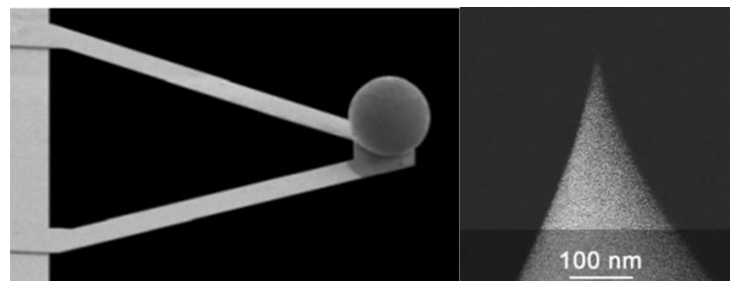


Figure 3.5: SEM images of an AppNano[®] SICON-TL-BSG-A colloidal tip (left) and MikroMasch[®] HQ CSC17/NO AL silicon parabolic tip (right)

The spring constant of AFM tips used in the experiments was calibrated at the start of each experiment section using a two-step method. Firstly, the sensitivity of the cantilever was obtained by indenting a standard silicon wafer substrate. Then, the cantilever was tuned in the air, and the resonant frequency k was captured by the AFM system. The cantilever thickness was calculated based on its length and width (value from the tip manufacture) and the measured resonant frequency from the first step. Afterwards, the cantilever spring constant was calculated based on the measurements obtained using the established spring constant equation for a rectangular beam:

$$k = \frac{E_b w t^3}{4L^3} \quad (3.1)$$

where E_b is Young's modulus of the beam, w , L and t are the width, length and thickness of the beam. The details of the calibration method and the modifications of the equation when spheres were attached have been described in the article of Bowen et al. (153). The properties of different AFM probes used in this chapter are listed in Table 3.1.

Table 3.1: Properties of different AFM probes

Probe	Tip Shape	Tip radius of curvature (μm)	Force Constant (N/m)	Sensitivity (nm/V)
CSC17	Cone	0.008	0.329	93.53
BGC	Sphere	2.7	0.108	72.87
PSC	Sphere	2.6	0.171	64.25
TIC	Sphere	2.6	0.162	64.94

The CSC17 probes are standard Si probes suitable for tests of general purposes. It has a sharp cone-shaped tip and can be used to obtain surface topography of down to 5-10 nm. Colloidal probes have around 5 μm diameter microspheres attached on the tip and were applied to measure surface-surface interactions between cells and different materials.

3.2.4 AFM Measurement of Cells in Aqueous Solutions

For cell surface measurements the AFM indentations took place in aqueous solutions, as the samples were submerged in DMEM. Before the actual test, the culture medium was allowed to equilibrate for 20 minutes in order to reach the laboratory temperature. The cell-culture petri dish containing living MC3T3 cells was attached to the AFM sample holder using double-sided tape. Then the AFM probe was controlled to gradually descend into the solution, where it remained at a steady position above the sample for 3-5 minutes to establish thermal equilibrium. Under aqueous conditions, the setpoint was set at 5-12 nN for cell measurements, and the sampling rate was 10,000 Hz. Based on experience and in reference to the literature (154), the cantilever movement speed was set at the low speed of 2 $\mu\text{m/s}$ to reduce hydrodynamic noise while maintaining a reasonable experimental time.

3.2.5 Fitting the Data to the Hertz and JKR Models

Two contact mechanics models were adopted in order to study the elastic properties of the tested samples: the non-adhesive Hertz model (155) and the JKR model (156) which takes into consideration adhesion between the AFM tip and the sample. F-D curves acquired from the AFM indentation experiments were fitted using the equations derived from the Hertz and JKR models as will be described.

In the Hertz model, the relationship between force and displacement was adopted to fit the experimental results acquired by pressing the AFM tip on non-adhesive sample surfaces.

The equations are as follows: for an elastic sphere with a radius R making contact with an elastic half-space, the relationship between the indentation displacement δ , contact radius a , and tip load F , is described as follows:

$$a = \sqrt{R\delta} \quad (3.2)$$

$$F(a) = \frac{4E^*a^3}{3R} \quad (3.3)$$

The reduced modulus E^* is:

$$E^* = \frac{1 - \nu_1^2}{E_1} + \frac{1 - \nu_2^2}{E_2} \quad (3.4)$$

Based on the above equations, non-adhesive F-D curves can be fitted using the Hertz contact model through an automatic process within the JPK data processing software to obtain the Young's modulus.

When taking into consideration the adhesive interaction between an AFM tip and a sample, the models developed by Johnson–Kendall–Roberts (JKR) (156) and Derjaguin–Müller–Toporov (DMT) (157) are those most often applied. Figure 3.6 demonstrates the differences between the Hertz, JKR and DMT contact models in terms of the pressure distribution under compression, the shapes of two bodies under compression, and the shapes of two bodies under zero loads when offloading. It can be seen from the stress distribution that there is no adhesion in the Hertz model, whereas adhesive contacts are presented outside the contact area for the DMT model and inside the contact area for the JKR model.

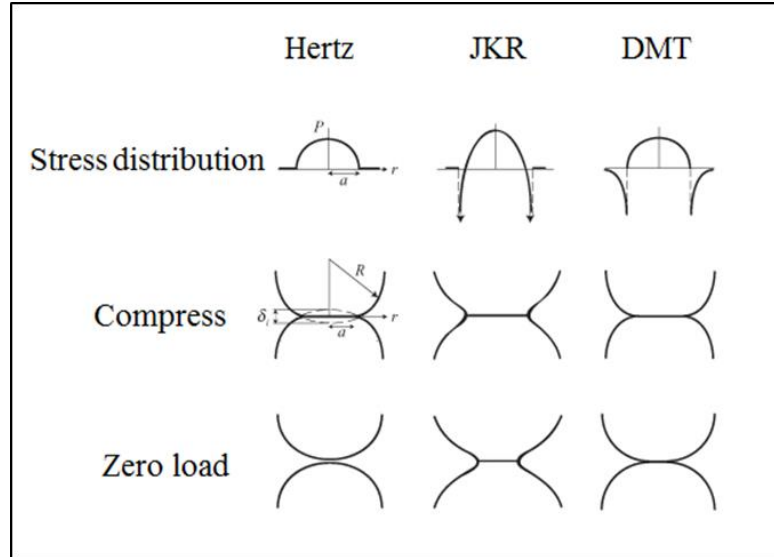


Figure 3.6: Schematics of stress distributions of the Hertz, JKR and DMT models during compression

The differences between the Hertz, JKR and DMT contact models regarding the pressure distribution under compression, the shapes of two bodies under compression and the shapes of two bodies under zero load when offloading is shown. The Hertz model assumes full elastic deformation and no adhesion to be present between the two contacting surfaces. Stress is distributed symmetrically around the centre of the contact circle (with radius a). When fully offloaded there is no adhesion force between two bodies. The JKR and DMT models take into consideration the surface forces, and adhesive forces are present at the edge of the contacting zone; therefore two spheres cannot be separated when the load is back to zero. A pull-off force is required to separate two spheres in the JKR and DMT models. The difference between the JKR and DMT models is that in the JKR model the area of contact is larger than that predicted in the Hertz model and all the stress is within the area of contact. In contrast, the DMT model assumes that the contact profile remains the same as in the Hertz model but with additional attractive interactions outside the area of contact.

To quantify the differences between different models, equations of the applied load F and the contact radius a , at deformation δ are listed in Table 3.2.

Table 3.2: Differences between the Hertz, JKR, and DMT models

Differences regarding the contact radius a , the sample deformation δ , and the adhesion force F for a spherical tip on a flat surface.

	Hertz	JKR	DMT
a^3	$\frac{3RF}{4E^*}$	$\frac{3R}{4E^*} (F + 3\pi R\Delta\gamma + \sqrt{6\pi RF\Delta\gamma + (3\pi R\Delta\gamma)^2})$	$\frac{3R}{4E^*} (F + 2\pi R\Delta\gamma)$
δ	$\frac{a^2}{R}$	$\frac{a^2}{R} - \sqrt{\frac{2\pi a\Delta\gamma}{E^*}}$	$\frac{a^2}{R}$
$F_{\text{pull-off}}$	0	$\frac{3}{2}\pi R\Delta\gamma$	$2\pi R\Delta\gamma$

In Table 3.2 $\Delta\gamma$ is the work of adhesion and represents the adhesion between a spherical tip and a flat surface. This is defined as the work needed to separate two adjacent bodies marked 1 and 2:

$$\Delta\gamma = \gamma_1 + \gamma_2 - \gamma_{12} \quad (3.5)$$

In the Hertz model the adhesion $\Delta\gamma$ of the tip-sample interaction is neglected, while the other models take this into account either outside (DMT model) or inside (JKR model) the contact area; however, both theories are approximations. Tabor (158) reported that these two theories can be unified by a parameter defined as:

$$\lambda = \frac{\delta_c}{z_0} \approx \sqrt[3]{\frac{R(\Delta\gamma)^2}{E^* z_0^3}} \quad (3.6)$$

where z_0 is the equilibrium separation between the two surfaces in contact.

The JKR model applies to large, compliant spheres for which λ is larger than 5, while the DMT model applies to small, stiff spheres ($\lambda < 0.1$) (159). In the study presented in this chapter, the JKR model can be applied as large tips are utilised to indent soft samples with a large adhesion force. Therefore, the relationship between the indentation depth δ and force F can be fitted using experimental data and the following equations:

$$\delta = \frac{a^2}{R} - \sqrt{\frac{2\pi a \Delta\gamma}{E^*}} \quad (3.7)$$

$$a = \sqrt[3]{\frac{3R}{4E^*} [F + 3\pi R \Delta\gamma + \sqrt{6\pi R F \Delta\gamma + (3\pi R \Delta\gamma)^2}]} \quad (3.8)$$

A program was designed using MATLAB software to fit the F-D curves acquired from the experiments utilising equations 3.6 and 3.7, which calculated the work of adhesion $\Delta\gamma$ and Young's modulus E.

3.3 Results and Discussion

3.3.1 AFM Tests on Live Cells

Figure 3.7 shows an example of an attached MC3T3 cell. From experience, the morphology and size of this example of an MC3T3 cell cultured in the serum-free medium are not like that of cells cultured in serum-supplemented media. The cell had a spread approximately 30 μm on the major axis and spread to other directions to a similar extent; the height of the example cell was around 7.5 μm in the nucleus centre area. AFM indentation tests were separately carried out with a polystyrene colloidal probe on the nucleus area, the cytoplasm area and the substrate zone.

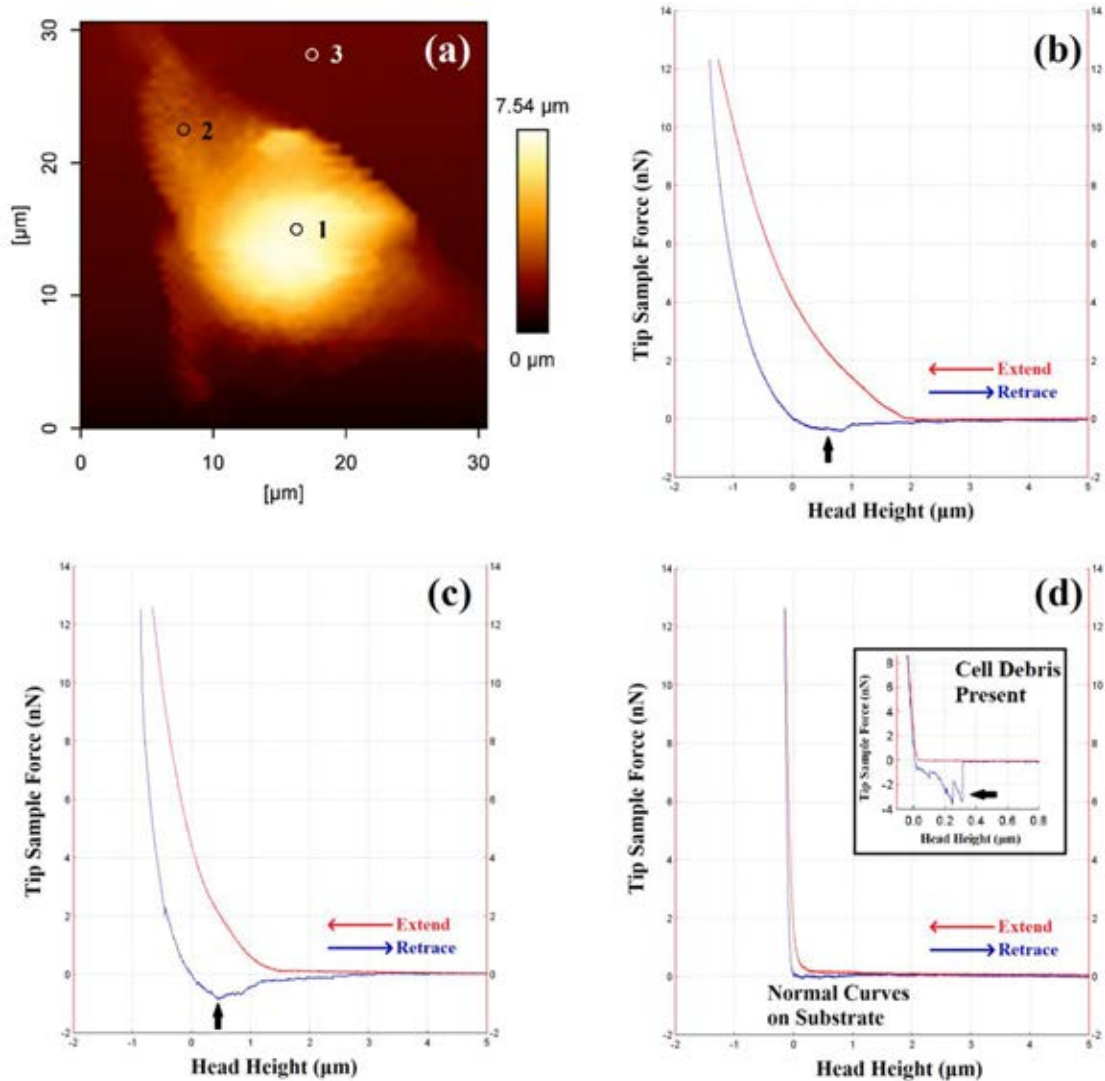


Figure 3.7: AFM tests performed on different cellular locations and typical force-displacement curves

(a) AFM topography image of an MC3T3 cell. Areas marked 1, 2 and 3 represent illustrative measurement positions for the cell nucleus, cytoplasm and substrate, respectively. The cell had a spread of around 30 μm on the major axis, and the height was around 7.5 μm in the nucleus centre area. (b) An example of F-D curves measured on the cell nucleus area, i.e. on area 1. The blue retraction curve shows some adhesive force (black arrow) before the detachment of cell surface and the AFM tip. (c) An example of F-D curves measured on cell cytoplasm area, i.e. on area 2. It can be seen that the red extend curve showed a faster increase in the repel force while compressing against the cell surface, which suggests a higher elastic modulus. At the same time, the blue retraction curve shows a higher adhesive force (black arrow) than that of the nucleus zone. (d) An example of F-D curves for the substrate, i.e. on area 3. The elastic modulus was significantly higher than those for the biological sample, and there was no apparent adhesion force present. If there were cell debris in the substrate, then the F-D curve has a saw-tooth pattern as shown in the inset.

As expected, the AFM F-D curves on the different test areas yielded different patterns. The hysteresis between the extension and the retraction curves in Figure 3.7(b) for the nucleus and Figure 3.7(c) for the cytoplasm were caused by the viscous behaviour of the cell, as the indentation energy was dissipated during the AFM tip extension and retraction process. This viscous behaviour was related to the loading speed of the test, which had been set to be 2 $\mu\text{m/s}$, which led to the corresponding loading time of around 1 second. This loading rate was set in order to maintain low hydrodynamic noise and viscous relaxation, balanced against experimental efficiency. The viscous behaviour of cells is a very important point to understand and has been the focus of many previous studies (160, 161); however, it was not the focus of this study. It can also be seen that the F-D curve measured on the cell nucleus area generally demonstrates less adhesion than that for the cytoplasmic area. AFM indentation curves for the substrate area revealed standard elastic solid curves; however, occasionally molecule-chain breaking could be observed in the retraction curves, which occurred when cell debris was present on the surface, as shown in Figure 3.7(d).

The elastic properties of cells were studied by fitting the F-D curves to contact mechanical models. The Hertz model was initially used to fit the extension curves, and if soft materials like living cells are the target, it is important to choose the appropriate fitting range from the F-D curves for a reasonable elastic modulus. From Figure 3.8, it can be seen that the calculated elastic modulus of a cell sample varied with different indentation depths, which was because the AFM tip was interacting with inhomogeneous materials during the indentation process. During the indentation of the nucleus zone, as shown in Figure 3.8(a), the calculated Young's modulus started to increase and then plateaued at around 500 nm, which suggests contact with the cell surface, before reaching a stable zone at an indentation depth of around 1200 - 1300 nm,

which suggests that the probe was indenting the nucleus in the elastic region. After this steady zone, the elastic modulus increased with indentation depth, suggesting that the solid substrate underneath was influencing the measurements. A similar pattern could be found in the cytoplasm zone as shown in Figure 3.8(b), where an indentation depth of 500-700 nm corresponded to the stable zone.

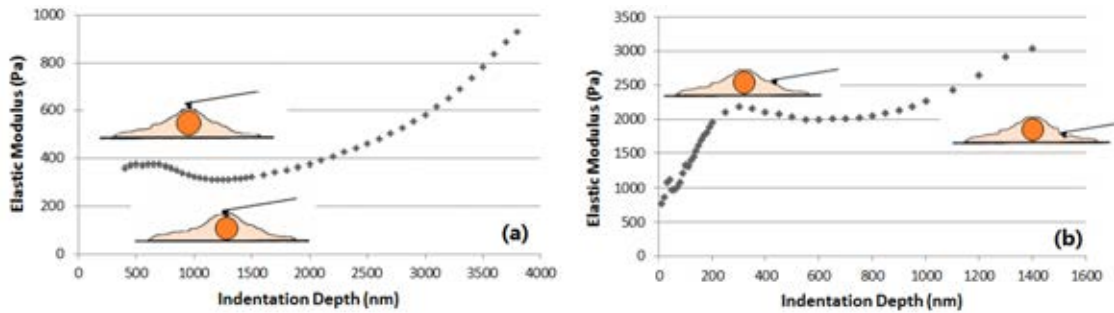


Figure 3.8: Examples of how Young’s modulus changed with different indentation depth for the (a) nucleus zone and (b) cytoplasm zone

The measured Young’s modulus depended upon the indentation depth due to the inhomogeneity of the tested sample; consequently, it is important to find the fit range (indentation depth) in order to yield optimal and reproducible results. (a) During the indentation of the nucleus zone, Young’s modulus started to increase to a plateau of around 500 nm, which suggested contact with the cell surface. Then it reached a stable zone at an indentation depth of around 1200 - 1300 nm, which suggests that the probe was indenting the nucleus in the elastic region. After the steady zone, the elastic modulus increased with indentation depth, which suggests that the solid substrate underneath was influencing it. (b) A similar pattern could be found for the cytoplasm zone, where an indentation depth of 500-700 nm corresponded to the stable zone.

After determination of the optimised fitting range, 10 to 20 repeating results were acquired for each test location. The averaged Hertz fitting results are provided in Table 3.3, together with the measured adhesion force. The measurements for the ‘substrate’ in Table 3.3 were based on data collected from a rigid substrate, i.e. without the presence of cell debris and the accompanying molecule-chain breaking phenomenon that was shown in Figure 3.7(d).

Table 3.3: Mechanical properties of MC3T3 cells as measured by AFM indentation

Maximum adhesion forces and Young's modulus of the nucleus zone, the cytoplasm zone and the substrate. (Mean and SD presented for each testing area, N = 16)

Testing location	Adhesion force (pN)		Young's modulus Hertz model (kPa)	
	Mean	SD	Mean	SD
Nucleus	399	166	0.748	0.265
Cytoplasm	972	256	1.604	0.285
Substrate	73.6	13.4	25260	2723

From Table 3.3 it can be seen that the calculated Young's modulus was generally greater in the cytoplasm zone (1.604 kPa) than the nucleus zone (0.748 kPa), while the petri dish substrate had a significantly higher value than the soft biological samples. The results shown in Table 3.3 demonstrate that the cytoplasm zone generated a larger adhesion force than the nucleus zone, while that of the substrate was minimal. It can also be seen that the standard deviation for the inorganic substrate measurements was small compared to the measurements for the biological tissues. Because the testing targets in both the cytoplasm and nucleus zones were not homogeneous, nor did they behave with a typical pattern, the standard deviations for the biological measurements were quite high. The results were averaged from different testing points of a cell, which may too have contributed to the high deviation observed. Also, the test results for the nucleus zone (SD 35%) were more diverse than that of the cytoplasm zone (SD 17%), which was caused by greater material inhomogeneity and possibly horizontal movement of the nucleus while under pressure from the AFM tip.

It can be seen from Figure 3.7(c) and Table 3.3 that a large adhesion force is apparent in the cytoplasm zone test results. Therefore the JKR model was applied to fit the retraction curves acquired from the cytoplasm zone. Figure 3.9 demonstrates an example of curve fitting results of the JKR model (left) for the retraction curve and the Hertz model (right) for the compression curve. Regarding the methodology, the Hertz

fitting was performed using the JPK data processing software, while the JKR fitting was performed using the MATLAB code developed from equations 3.7 and 3.8. As can be seen from the left panel of Figure 3.9, the sudden increase in the indentation force was due to the discontinuous decrease of the contact area during the pulling out process, and the discontinuous steps of the retraction curve (blue curve) cannot be fitted using the JKR model, which is shown by the black curve.

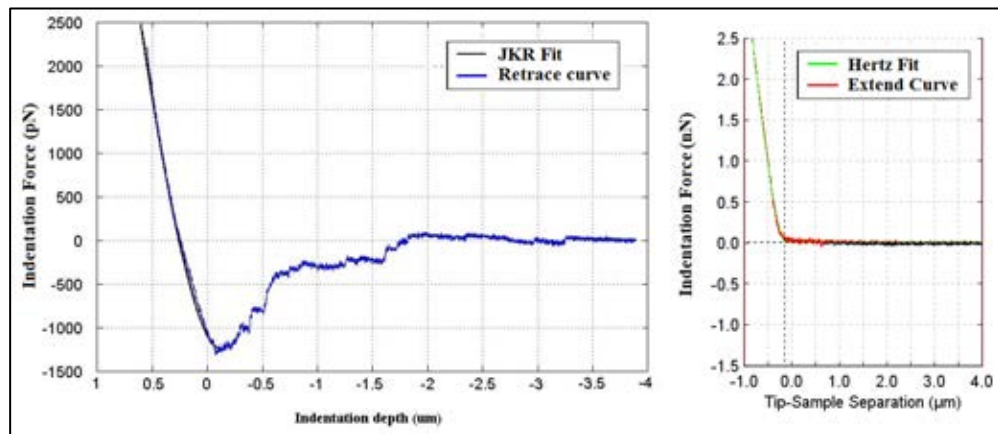


Figure 3.9: Example of curve fitting using the JKR model (left) and the Hertz model (right)

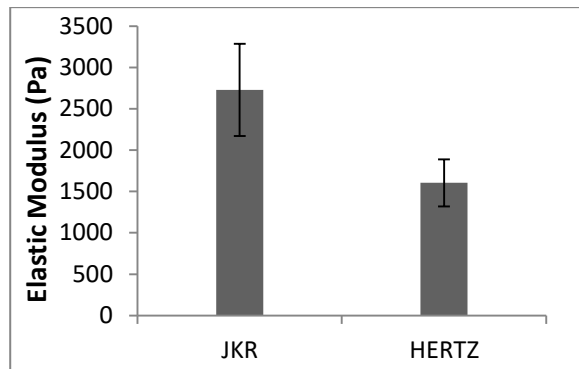


Figure 3.10: Comparison of the Hertz and JKR model fitting for the cytoplasm zone

The elastic modulus (Mean \pm SD) was obtained by the JKR model (N = 13) and the Hertz model (N = 16).

The averaged fitting results for the Hertz and JKR models are presented in Figure 3.10, and the averaged Young’s modulus value obtained from the JKR model (N = 13, 2.73 \pm 0.53 kPa) was larger than that from the Hertz contact model (N = 16, 1.60 \pm 0.28 kPa), although this difference was insignificant ($p > 0.1$). Comparing these results with those

of other researchers, the elastic modulus of MC3T3 cells were not significantly affected by the presence or absence of serum in the culture medium. For example, Gardinier et al. (162) found MC3T3 cells to have 1.7 ± 0.3 kPa stiffness using AFM, and Takai et al. (163) reported similar values for MC3T3 cells which were within the range of 1 and 2 kPa.

3.3.2 Effect of Indentation Pausing Time

The time-related interactions between an AFM tip and the cell surface are presented in this section. AFM indentations were carried out with various pausing times added during the contacting period. As illustrated in Figure 3.11, during each testing cycle the AFM tip was held in contact with the sample for a specified period (pausing time) between the normal extension process and the retraction process.

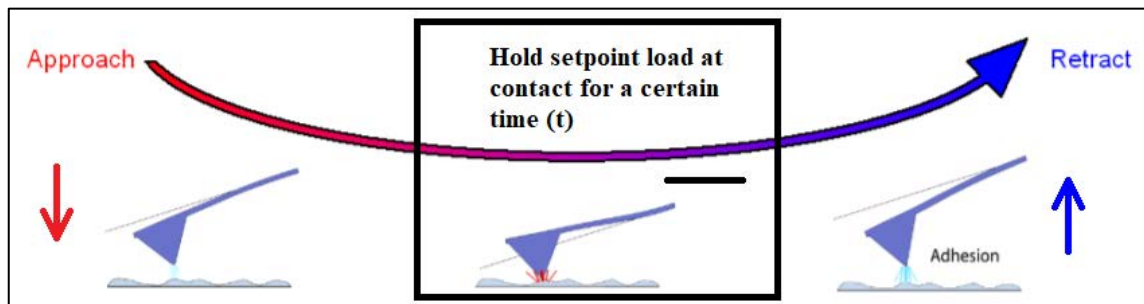


Figure 3.11: Schematics of the pausing time interval experiments

After approaching the sample surface, the AFM tip was held (with constant load) for a specified period while in contact with the sample, before the tip was pulled out of the sample.

Three groups of indentation experiments were carried out with contact pausing times of 1 second, 10 seconds and 30 seconds added separately to living MC3T3 cells. Similar to the experiments in Section 3.3.1, indentations were also carried out on the cytoplasm zone and nucleus zones independently. Each setup was repeated 16 times on different testing points, and the results are summarised in Figure 3.12 and Figure 3.14.

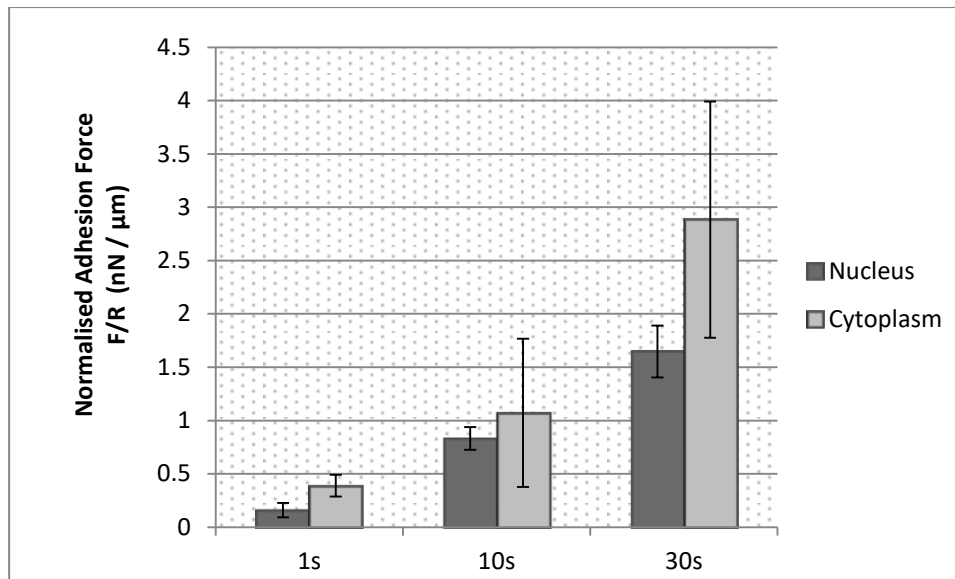


Figure 3.12: Tip-sample adhesion on the nucleus zone and cytoplasm zone for different contact pausing times

The adhesion forces between the AFM tip and cell surface after pausing for 1 second, 10 seconds and 30 seconds. Indentations were performed on both the nucleus zone and the cytoplasm zone, and the results are shown in the normalised form of the force divided by the tip radius. (Mean \pm SD. N = 16)

Figure 3.12 shows two clear trends in the adhesion results. Spherical AFM tips have a different radius compared to the microspheres attached which affected the adhesion force measured. Thus the adhesion force results were normalised against the tip radius R to enable a more meaningful comparison to be made between different tips. Tests on both the nucleus and cytoplasm zones showed increased adhesion with more pausing time. For tests performed above the cell nucleus, adhesion was increased from the minimum value of 0.160 nN/ μm for 1 second pausing, to 0.832 nN/ μm and 1.647 nN/ μm after 10 seconds and 30 seconds pausing, respectively. The results for the cytoplasm zone showed a similar increasing trend, as the adhesion forces after 10 seconds and 30 seconds pausing were 1.76 times and 6.42 times larger than after a 1 second pause. It was also noted that for every cell tested the adhesion for the cytoplasm zone was always greater than that of the nucleus zone.

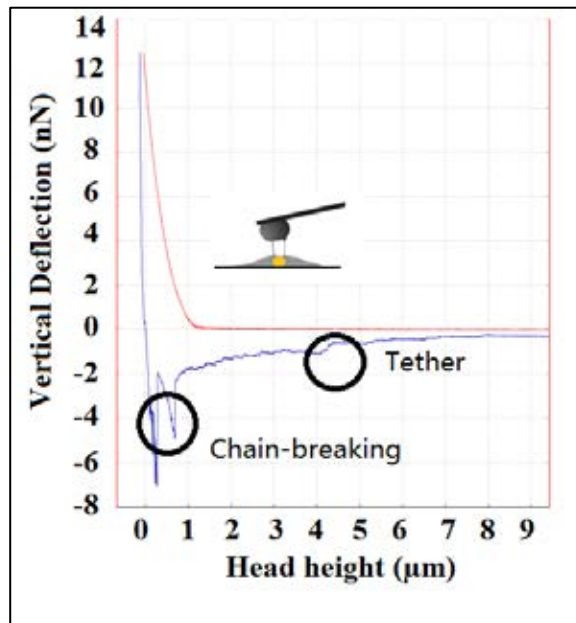


Figure 3.13: A typical force-displacement curve for the cytoplasm zone showing molecule binding breaks on the retraction curve

Indentation curves for the cytoplasm zone indicated molecule chain breaking behaviour at some positions (Figure 3.13), and the sudden change in force indicates the breaking of ligand-receptor binding during the detachment. The tether steps in the force curve represent the gradual rupture of the cell membrane by the AFM tip. This type of curve was frequently observed for cytoplasm indentations in the 10 second and 30 second pausing groups, which led to a large variance in the testing results (error bars). However, it was rarely seen for nucleus zone curves or for results of the 1 second pausing time.

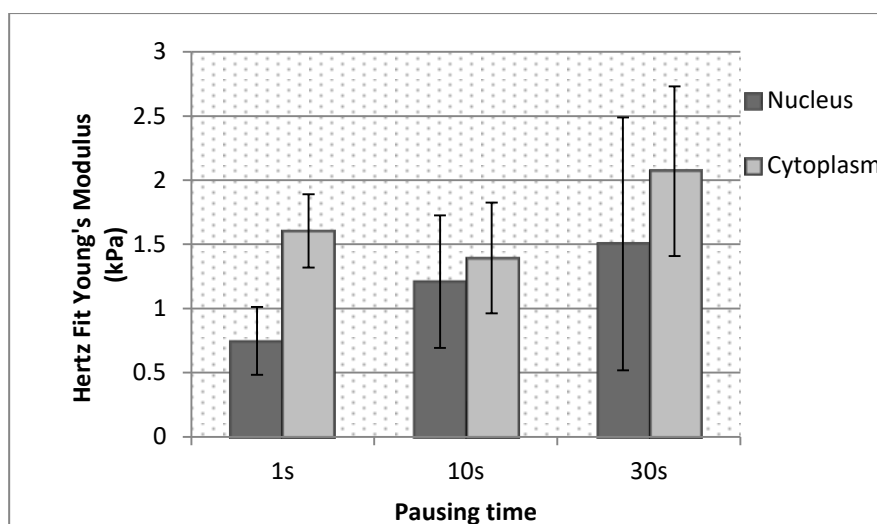


Figure 3.14: Hertz fitted modulus for the nucleus zone and cytoplasm zone with different pausing times

The Young's modulus was acquired by the Hertz fitting mode. Indentations were performed on both the nucleus zone and the cytoplasm zone with pausing times of 1 second, 10 seconds and 30 seconds. (Mean \pm SD, N = 16)

The Hertz fitted Young's modulus values are presented in Figure 3.14. Consistent with the findings from section 3.3.1, the elastic modulus was higher for the cytoplasm zone than the nucleus zone, due to the influence of the rigid substrate. Longer pausing times had no significant influence on the averaged elastic modulus fitted using the indenting curves. The error bars increased with longer pausing times, which was expected since the samples may be moving or dissipating compressed energies during the holding period, and this uncertainty caused variance in the Hertz fitting range and thus led to a larger variance in the results.

3.3.3 Effect of Different AFM Tips

In addition to the PS colloidal tip (PSC) used in the previous studies, three more probes were applied in order to explore the interaction between cells and different probes: a borosilicate glass colloidal tip (BGC); a parabolic tip (CSC17); and a Ti coated PS colloidal tip (TIC). Indentation experiments were performed with different pausing times of 1 second, 10 seconds and 30 seconds, and the Hertz and JKR models were

applied to investigate the effect of different probes on the measured mechanical properties of the cells. Each set of experiment was repeated 10 to 20 times on different testing points.

F-D curves obtained from the CSC17 tip did not show any noticeable adhesion regardless of the length of the pausing time (Figure 3.15), and no molecule breaking jump effect was observed. This was believed to be caused by the small tip size and the cone shape tip geometry. The CSC17 tip is usually used for a quick topographical scan, and it has completely different geometries compared to the other spherical tips so the measurement cannot be normalised in the same way as with the other spherical tips.

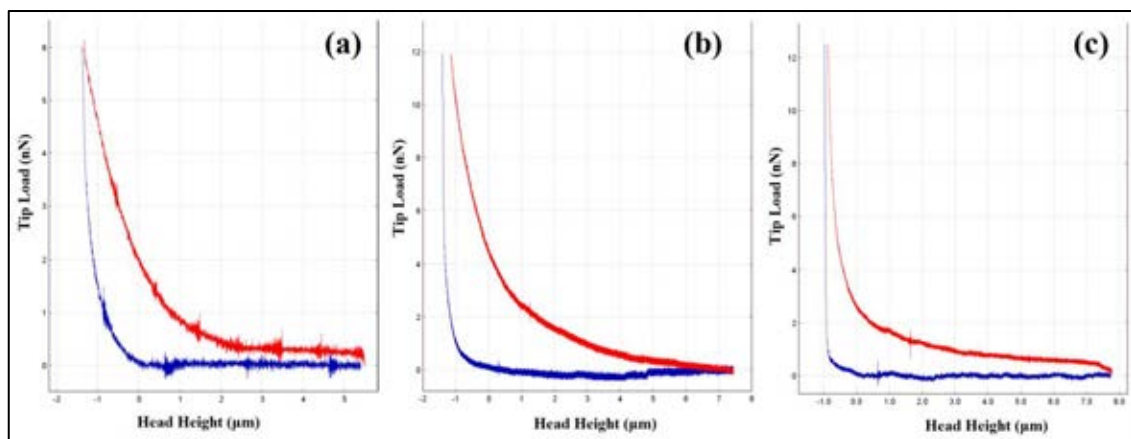


Figure 3.15: Typical force-displacement curves for a CSC17 tip indenting an MC3T3 cell Pausing times were (a) 1 second; (b) 10 seconds; and (c) 30 seconds.

The averaged tip-sample adhesion for TIC tips and PSC tips are shown in Figure 3.16. It was revealed that PSC tips showed better adhesion forces than the TIC tips for all three pausing times, although both probes showed increased adhesion force with increasing pausing times. Besides, the time-dependent adhesion increased more rapidly for PSC tips compared to TIC tips. The adhesion force for PSC tips was approximately 1.7 times that of TIC tips for 1 second pausing time, and this increased to 2.7 times and 3.5 times for the 10 seconds and 30 seconds pausing times, respectively.

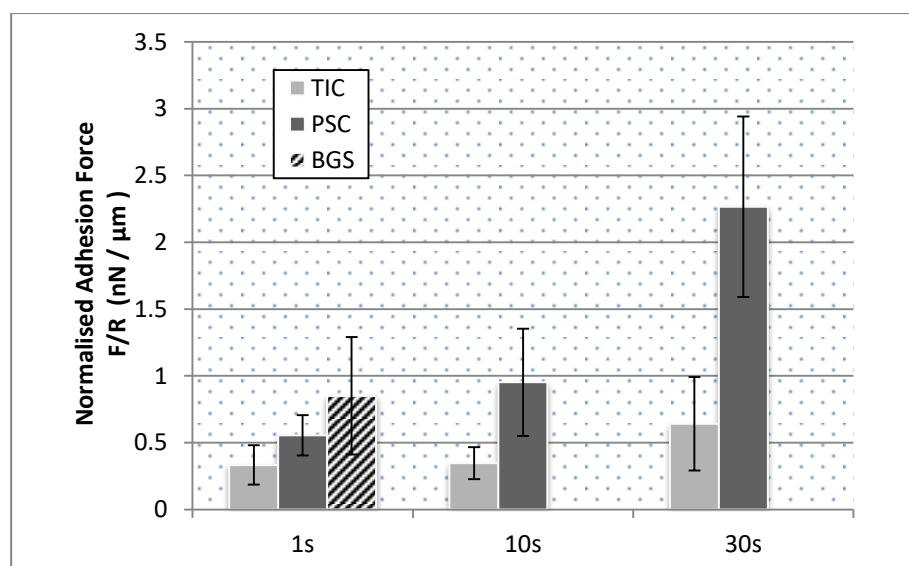


Figure 3.16: Averaged tip-sample adhesion results using TIC and PSC tips with different pausing times

The PSC tip and TIC tip were used for experiments with all pausing time intervals while the BGC tip was only utilised in the one second experiments due to the limitation of experimental conditions. Results are shown in the normalised form of force divided by tip radius. (Mean \pm SD, N = 10)

Experiments with a BGC tip were only performed successfully with 1 second pausing due to an issue with the AFM system. It can be seen from Figure 3.16 that MC3T3 cells demonstrated different adhesion tendencies for different tips; however, all three colloidal tips generated obvious adhesion, as can be seen from the F-D curves, with that for the BGC tip being noticeably larger than the TIC tip. Consequently, it can be assumed that floating cells will experience a different level of adhesion when approaching PS, Ti or glass surfaces. It was noticed that the standard deviations of the adhesion force measurements were high (above 50% of the mean for some groups), especially with the larger pausing time. This is believed to be potentially caused by molecule binding that occurred during the contact period and then chain breaking when the tips were moved away from cells (Figure 3.13). Another reason for the high standard deviation was the limited sample size. Only a limited number of measurements were acquired because AFM measurements on live cells are time-consuming, and AFM

probes are often contaminated by cell debris after several indentations, thereby limiting reliable measurements to only the first few scans.

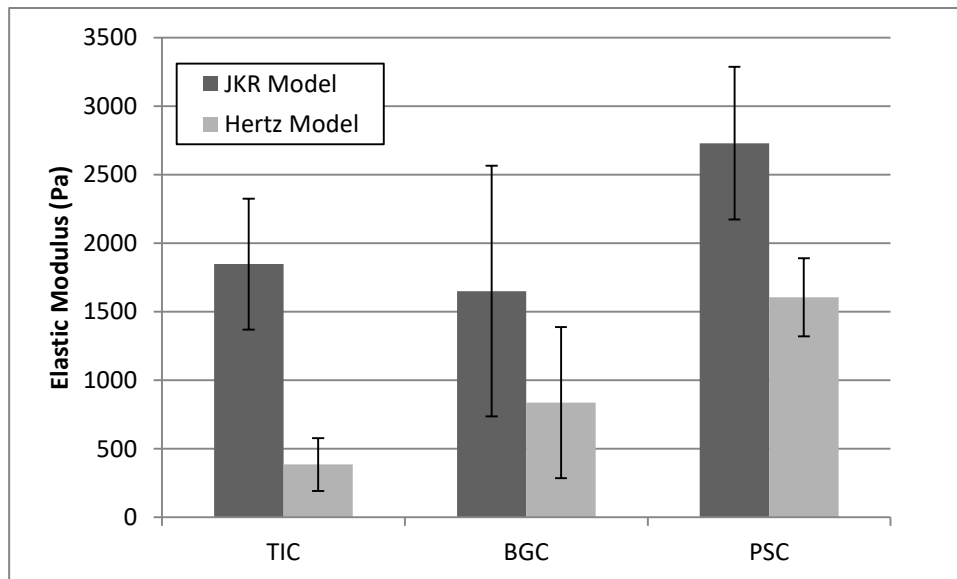


Figure 3.17: Hertz and JKR model fitting results for measurements with different tips

The elastic modulus of the cells was acquired by indentation experiments using TIC, BGC and PSC tips. Both the Hertz model and JKR model were applied and the results compared. (Mean \pm SD, N = 10)

The elastic modulus of the MC3T3 cells is demonstrated in Figure 3.17, where the Hertz model and JKR model fitting results are compared. Generally, the JKR results showed a larger modulus than the Hertz fitted results. During the indentation and retraction process, the energy delivered by the indenter was not completely sent back by the targeted cell. This energy dissipation leads to hysteresis between the extension and retraction force curves (as can be seen in Figure 3.7), thus affecting the measurements of the Hertz model (on the extension curve) and the JKR model (on the retraction curve). The difference between the JKR and Hertz measured modulus could be due to viscous energy dissipation. When comparing the results between different tips, the JKR fitting acquired results with no significant difference ($p > 0.1$). While the Hertz model fitted modulus were larger when indented using a PSC tip than by TIC tip ($p < 0.05$).

This difference could be because of the different areas of cells selected for the indentation experiments, as was discussed in section 3.3.1.

From Figure 3.18 it can be seen that the work of adhesion $\Delta\gamma$ modelled by the JKR fitting corresponds well with the AFM measured pull-off force for all three groups (the difference was insignificant with $p > 0.1$ for all three groups), which indicates accurate fitting of the adhesion phenomena by the JKR model.

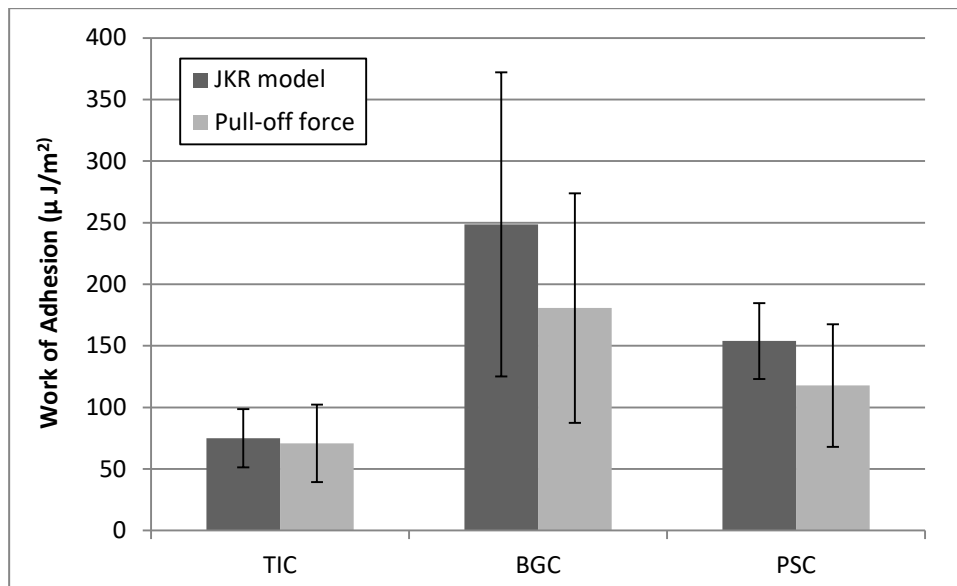


Figure 3.18: JKR fitting work of adhesion compared to the pull off force

Work of adhesion was modelled by JKR fitting and compared to the AFM measured values. Pull-off forces measured by AFM were modified by the equation $\Delta\gamma_{\text{pull-off}} = 2F_{\text{pull-off}}/3\pi R$ to be comparable with the modelled values. (Mean \pm SD, N = 10)

3.4 Summary

In this chapter AFM measurements of live cells have been extensively investigated. Living MC3T3 cells were measured with various test parameters and different probes in order to comprehensively investigate their properties. Indentations with PSC tips were used in measurements on different regions of living cells, and the different properties of the nucleus zones and cytoplasm zones were discussed. The elastic modulus of a cell was calculated by fitting the data to the Hertz model and JKR model using extension

curves and retraction curves, respectively. It was found that MC3T3 cells generally demonstrated a higher Young's modulus and adhesion for the cytoplasm zone compared to the area above the cell nucleus. The JKR model results yielded a higher elastic modulus and greater adhesion than the Hertz model. The classical Hertz contact theory provides guidelines for the elastic deformation of bodies in contact and is valuable as a rough estimation when a new sample is measured for the first time. However, the Hertz model makes several assumptions that are not truly met if living cells are tested, as it assumes absolute elastic behaviour, as well as homogeneity of the tested sample, which is not strictly accurate for biological samples. More importantly, it neglects adhesion force; thus the JKR model should be more realistic in describing the adhesive interaction between a spherical AFM tip and cells.

Different pausing intervals of 1 second, 10 seconds and 30 seconds were added between the extension and retraction process during an indentation cycle. In this way, time-dependent adhesion was created during the pausing intervals, whereby the AFM tip remained in contact with the cell. The results showed a dramatic increase in adhesion between the cell surface and AFM tip after setpoint pausing, which was greater for the cytoplasm zone than the nucleus zone. Ligand-receptor binding and breaking, and membrane tethering were observed with 10 seconds and 30 seconds pausing times.

Finally, different AFM probes were applied to indent MC3T3 cells, including a PSC, BGC, TIC and a parabolic CSC17 tip. PSC and TIC tip testing showed similar time-dependent adhesion increases and ligand-receptor binding, while CSC17 tips did not. A comparison between the AFM results for the different tips showed that the short-term contact between a cell surface and AFM tip generated different levels of adhesion.

The study of the adhesion forces of MC3T3 using AFM has provided evidence that cells react to different surfaces with different adhesion. Consequently, it was necessary to further verify the relationship between the nanoforces of a surface and cell attachment, and this is presented in the following chapters. The AFM measurements for other mechanical properties of living cells and the comparison between the Hertz and JKR models are also useful for other cell studies.

Chapter 4 - Correlation between Surface Nanoforces and Cell Attachment

4.1 Introduction

This chapter presents an investigation of the hypothesis concerning whether the surface nanoforces of substrates play an important role in cell attachment. The finding of this investigation will help people to understand and gain better control over cell attachment, which has knock-on effects on subsequent cell activities. The cells studied in this research are anchorage dependent cells, and the investigation consists of various sets of *in vitro* experiments and the analysis of the results in order to determine the correlation between nanoforces and the rate of cell attachment. The results are also compared to those in the literature. The results of this chapter are expected to expand the understanding of the cell attachment process and could establish an effective approach to estimate how well anchorage dependent cells may attach to a given substrate.

The investigation commences with an examination of the correlation between surface nanoforces (mainly VDW force) and initial cell attachment. The surface adhesion forces of treated borosilicate glass samples were determined by AFM, together with surface characteristics of the attraction force, adhesion energy and surface roughness. *In vitro* cell culture experiments were then conducted directly on top of the measured samples using MC3T3 osteoblast precursor cells, and the number of viable cells after the initial attachment stage measured using the MTT (3-(4, 5-dimethylthiazol-2-yl)-2, 5-diphenyltetrazolium bromide) assay. The measured surface parameters were compared to cell attachment data separately for both the qualitative and quantitative approaches in order to validate the extent of the role of surface adhesion forces.

In the second part of the chapter, chicken tendon fibroblasts (CTF), mouse endothelial cells (MEC) and bone marrow stromal cells (BMSC, extracted from rat tibia and fibula) were utilised in the same experimental setup to test the hypothesis at a broader level.

The hypothesis was then further tested using several other common biomaterials. Al₂O₃ ceramic, PS (untreated), poly-di-methyl-siloxane (PDMS) silicone, borosilicate glass, Ti (treated and untreated), and hydroxyapatite were chosen due to their availability. The surface characteristics of these materials were obtained by AFM and compared to the cell attachment data found in the literature.

4.2 Methodology

The experiments were designed to serve the purpose of establishing whether there is a correlation between the surface adhesion force and cell attachment while eliminating other affecting factors. This was achieved by directly comparing several surface characteristics, including the attraction force, adhesion force, adhesion energy and surface roughness, with the cell attachment data.

The methodology adopted consists of three parts: the measurement of surface mechanical properties, specifically the surface adhesion force, attraction force, surface topography and surface roughness; an assessment of cell attachment; and statistical analysis to quantitatively compare the two sets of findings. The surface properties of the substrates were measured by AFM, and multiple parallel groups were tested in order to achieve more reliable outcome measures. Cell attachment to various samples was assessed by measuring the viable cell numbers one day after seeding, and the details of the experimental methods are provided in the following sections.

4.2.1 Sample Preparation

4.2.1.1 Glass Sample Treatment

Borosilicate glass coverslips (VWR®) were cut into 22 mm ×22 mm squares and cleaned in an ultrasonic cleaner (Jencons-PLS) with deionised water and acetone for 5 minutes separately. Following cleaning, acid-treated samples were submerged in 37% HCl overnight, while alkali-treated samples were submerged in 0.1 M NaOH overnight. The treated glass samples were then rinsed three times using deionised water and dried under a nitrogen gas stream. Different glass samples were observed by SEM (PHILIPS XL-30) to assess their morphology, and their chemical composition was measured using energy dispersive spectroscopy (EDS, Oxford Instruments INCA EDS system). The glass samples were later used for cell attachment experiments.

4.2.1.2 PDMS Base

Thermo Scientific™ BioLite 6-well cell culture plates were chosen to host the cell culture experiments. In order to eliminate the effect of the original base material (treated cell-culture plastic), an inert layer was deposited onto the base of each well. PDMS was chosen as the inert substrate to cover the base of the wells, as it is widely acknowledged to be a material to which cells do not readily attach (164). Also, it is a good reference material which does not react with the various chemical agents that are present within cell culture media (as shown in Table 4.1). In addition, PDMS has excellent transparency, which makes it convenient for light microscopic observation.

Table 4.1: PDMS reaction with different chemicals after immersion (165)

Chemical	Concentration (wt.%)	Time (min)	No	Mild	Medium	Total	Weight gain (%)
Buffered hydrofluoric acid	49.0	10	x				-0.97
Hydrochloric acid	37.9	10	x				-0.34
Potassium hydroxide ^a	86.9	10	x				-0.27
Hydrogen peroxide (H ₂ O ₂)	31.8	10	x				2.01
Piranha	3(H ₂ O ₂) : 1(H ₂ SO ₄)	10, 30	x				0.64
Photoresist developer ^b	100.0	10	x				-0.97
Water (deionized)	100.0	10, 30	x				-0.33
Hexane	99.9	10	x				4.67
Toluene	99.9	10	x				45.51
Acetone	99.7	10, 30	x				2.78
Methanol	100.0	10	x				-0.34
Isopropanol	100.0	10	x				-0.97
Potassium hydroxide ^a	86.9	60		x			0.75
Buffered hydrofluoric acid	49.0	30			x		1.39
Nitric acid	69.8	10			x		4.13
Hydrofluoric acid	49.0	10				x	-1.38
Sulfuric acid (H ₂ SO ₄)	96.0	10				x	-14.00
Potassium hydroxide ^a	86.9	1620				x	-0.90

^a 800 g of Potassium hydroxide were diluted in 4 L of deionized water. Immersion was done at 55°C.

^b Photoresist developer was combined with deionized water at a ratio of 1:4.

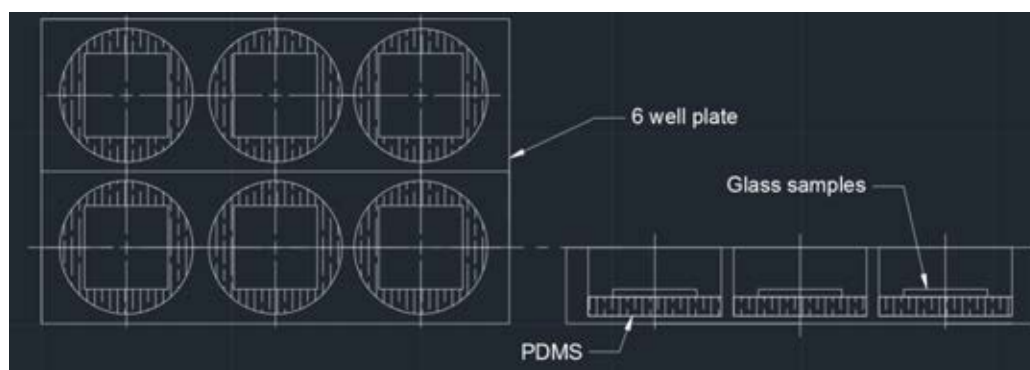


Figure 4.1: Modification of a 6-well cell culture plate to test treated glass samples

PDMS was deposited on the base of each well of the cell culture plate to create an inert layer to which cells do not readily attach. Glass samples were then placed on top of the PDMS layer.

Figure 4.1 shows how the 6-well plate was modified before commencing the experiments. PDMS was synthesised using Sylgard® 184 (Dow Corning Cooperation) in a 10:1 mass ratio for the elastomer base and curing agent. Approximately 1.5 ml of the mixture was injected into each well using a clean syringe, and the PDMS gel in the 6-well plate was cured at room temperature for 24 hours to reach a semi-cured gel status. The treated glass coverslips were then placed on top of the semi-cured PDMS mixture, and the samples were further cured at room temperature for a further 24 hours,

in order to reach the final status whereby the glass samples were secured to the layer of PDMS.

The entire 6-well plate, together with the attached glass samples, was immersed in 70% ethanol for 40 minutes and then air-dried in a biosafety level 2 cabinet. UV treatment was not chosen for these modified plates as from our unpublished experimental results it has been observed that UV treatment significantly modifies cell attachment on PDMS in our experimental setup (Figure 4.2).

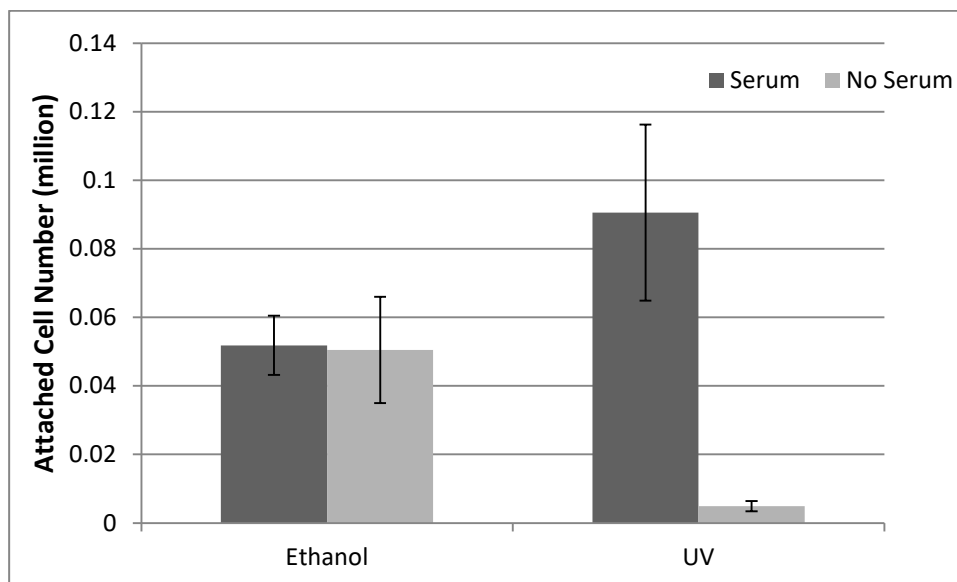


Figure 4.2: Effects of ethanol treatment and UV treatment on PDMS cell attachment

MC3T3 cells were cultured on ethanol treated and UV treated PDMS samples separately. PDMS was cured on the bottom of 6-well plates and 2×10^5 cells were seeded onto each sample. Attached cell numbers were assessed via an MTT assay one day after cell seeding. Two parallel groups of experiments were carried out at the same time, one supplemented with serum and the other one without serum. Each group contained three repetitions. (Mean \pm SD, N = 3)

Attached cell numbers on PDMS surfaces were assessed via an MTT assay one day after cell seeding with MC3T3. The effect of UV treatment on PDMS was studied for serum supplemented and no serum culturing conditions separately, and three parallel groups were assessed for each test condition. From Figure 4.2 it can be seen that UV treatment of PDMS significantly enhanced ($p < 0.05$) MC3T3 cell attachment in the serum-supplemented culture medium, while in non-supplemented cell culture medium

the initial attachment of MC3T3 cells decreased ($p < 0.01$). UV treatment of PDMS is believed to make modifications to PDMS surface chemical groups and thus lead to increased surface hydrophilicity (166). The difference between serum-supplemented culture and serum-free culture is believed to be due to alterations in protein adsorption. These results are in agreement with the published findings of other researchers (167, 168).

4.2.1.3 Titanium Surface Treatment

Ti samples were sintered by Dr Jian Liu at Sichuan University, and the samples were grown and polished using sand papers and diamond suspensions to a 1 μm finish. Pure Ti samples were immersed in 5M NaOH overnight and marked as alkali treated Ti. Alkali-treated Ti samples were placed in a nitrogen gas furnace, heat treated at 600°C for 1 hour and then cooled to room temperature in the furnace. These samples were marked as alkali-heat treated Ti samples. The surface structure of the treated samples was observed by SEM (PHILIPS XL-30 SEM).

4.2.1.4 Preparation of Other Substrates

Stainless steel, glass and PS substrates were polished to 0.5 μm in R_a roughness using SiC papers and a diamond suspension. Alumina ceramic was sintered by Dr Liu at Sichuan University using a pressure-less sintering technique and polished to a 0.5 μm in R_a using diamond suspension. PDMS silicone was synthesised using the same raw materials as described in section 4.2.1.2 and cured at room temperature for 48 hours.

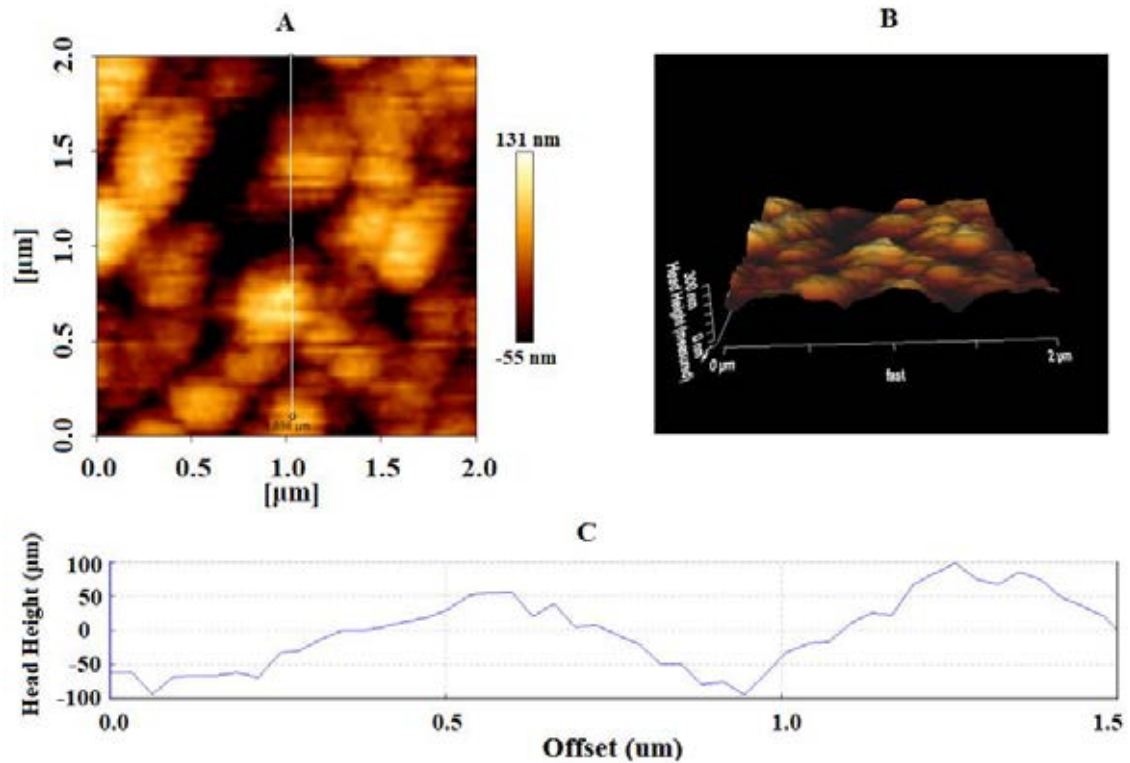


Figure 4.3: AFM measurement of the hydroxyapatite layer deposited onto treated Ti with a measurement area of 2 µm × 2 µm
 (A) 2D topographical view acquired by the AFM scan; (B) 3D topographical maps generated by software; and (C) cross-sectional height profile indicated by the white line in (A).

Hydroxyapatite samples were synthesised by immersing the alkali-heat treated Ti samples into cell culture medium for one week. All the samples were cleaned in deionised water for 5 minutes in an ultrasonic cleaner and then dried under a nitrogen gas stream. Samples were then examined by AFM for surface characteristics, and as shown in Figure 4.3, a layer of half-spherical hydroxyapatite with a radius of around 0.5 µm was formed on the original treated Ti surface.

4.2.2 AFM Testing

The surface characteristic data in this chapter was acquired using a JPK NanoWizard®II Atomic Force Microscope system. The set point for the solid surface measurements was set as 10 nN, the sampling rate was 10,000 Hz, and the cantilever movement speed was 200 µm /s.

Parabolic silicon tips (MikroMasch HQ csc17/no Al) with a median tip radius curvature of 8 nm were chosen to scan the sample surfaces, and schematics of the probe dimensions and images of a typical probe are shown in Figure 4.4. The spring constant of the AFM tips was calibrated at the start of each test using a two-step method developed by Bowen et al. (153).

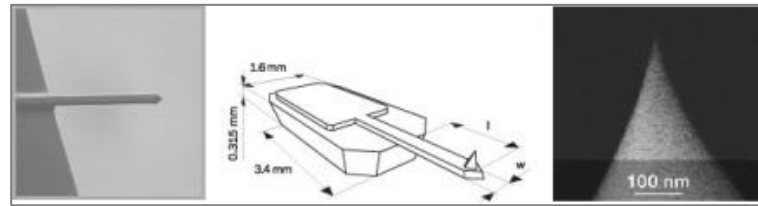


Figure 4.4: AFM tip, MikroMasch HQ csc17/no Al

AFM indentation tests were carried out under ambient conditions. Samples were cleaned in a clean room and packed into a sample box in order to minimise contamination, then immobilised onto a coverslip and fixed to the sample holder before testing. The temperature of the laboratory was controlled by an air conditioning system and was at a constant 17°C, while humidity varied between 30% and 40%.

Five different test points were chosen randomly for each sample surface. For each test point, a $10 \mu\text{m} \times 10 \mu\text{m}$ area was scanned in the contact mode and the AFM probe indented the scanning area through a 16×16 mesh matrix. This resulted in 256 sets of data for each testing point (Figure 4.5).

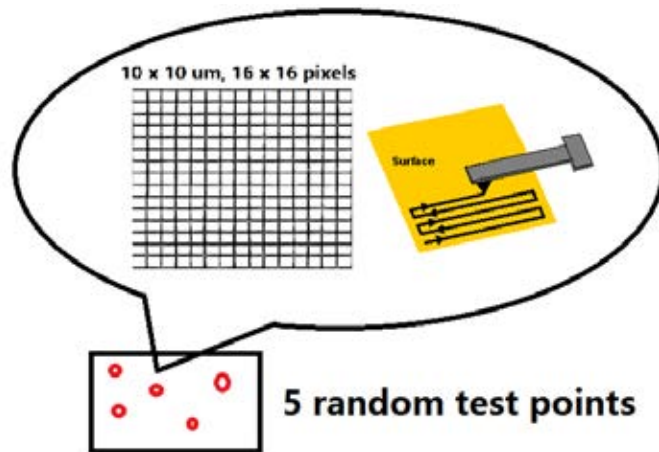


Figure 4.5: Schematic of how the sample surface was scanned by AFM

Five different test points were randomly chosen for each sample surface. Each test point contains a $10\ \mu\text{m} \times 10\ \mu\text{m}$ scanning area and was marked by AFM as a 16×16 mesh matrix. The AFM probe indented the target area pixel by pixel, line by line.

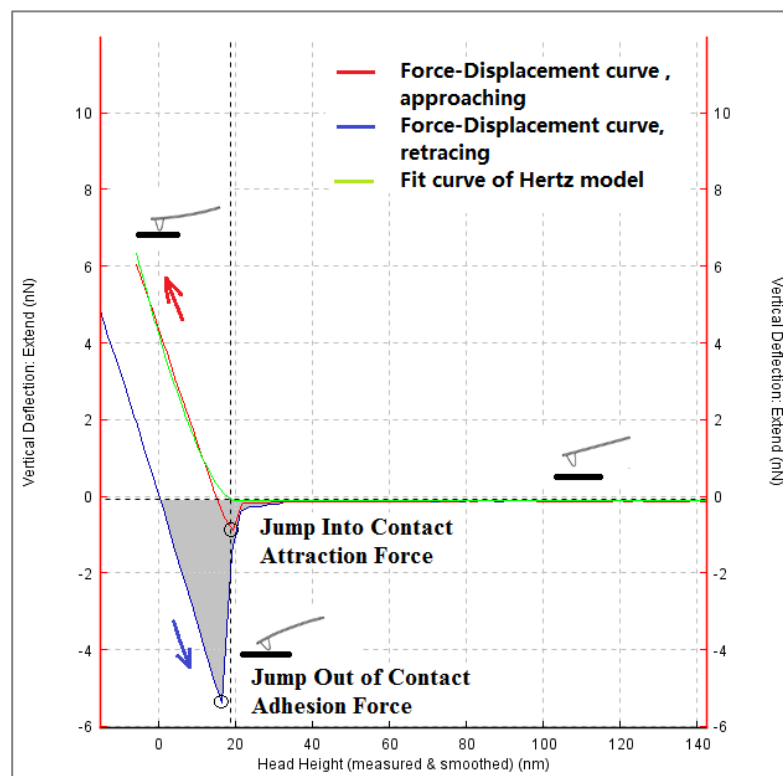


Figure 4.6: An example of force-displacement curves as measured using the AFM contact mode

F-D curves were processed by JPK data processing software, and the extracted data processed in the order of baseline alignment, contact point fixation, and data capturing. Topographical contour data were processed using a low-pass filter to remove noise

signals. A typical set of F-D curves is shown in Figure 4.6, where the maximum attraction force and maximum adhesion force were captured from the approaching curve (red) and retraction curve (blue), respectively, as indicated by the circles. The adhesion energy is the enclosed area between the baseline and the retraction curve (grey shaded) and represents the work required to remove the tip from the surface. The surface roughness was calculated from the surface height data of the whole tested area. Surface topographical features and surface roughness data were acquired at the same time using the AFM ‘force map’ testing mode. For example, in Figure 4.7 a surface map was captured with groove features on a nanometre scale.

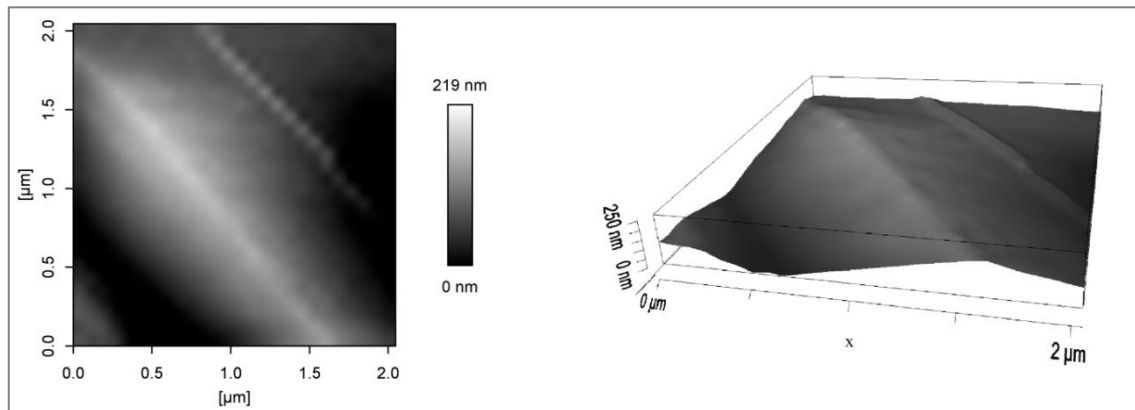


Figure 4.7: Example AFM topographical measurements of a graphene composite material

4.2.3 Cell Preparation and Culture

Four different types of cells were utilised: MC3T3, CTF, MEC, and BMSC. MC3T3, CTF, and MEC cells were thawed from liquid nitrogen stocks obtained from the TRAILab, University of Birmingham. The thawed cells were cultured in FBS supplemented DMEM at 37°C, in a 5% CO₂ incubator. The cell culture medium consisted of the base DMEM (Sigma D6546) which was supplemented with 10% FBS, 2% L-glutamine (200mM, Sigma G7513), 1% penicillin-streptomycin (10,000 units penicillin and 10 mg streptomycin per mL, Sigma P0781) and 2.4% HEPES buffer (1M, Sigma 59205C). Mouse BMSCs were extracted from rat tibia and fibula by Dr Jumbu

and then cultured in alpha minimal essential media (MEM) (Sigma M4526, supplementation was the same as for DMEM) and incubated at 37°C in a humidified incubator with 5% CO₂. Incubated cells were ready to be used in the cultured experiments after reaching around 80% confluence.

At the beginning of the cell seeding procedure, cells were detached using TrypLE™ Express (Gibco®). The detached cells harvested by centrifugation and then re-suspended in phosphate-buffered saline (PBS) twice to remove serum proteins as much as possible. The cell density of the suspension was assessed using an Invitrogen™ Countess™ cell counter, and cells were seeded onto sample surfaces at a density of 1×10^5 cells per well. For some experimental setups, a density of 2×10^5 cells per well was used. Serum-free DMEM (supplemented with 2% L-glutamine, 1% penicillin-streptomycin and 22mM HEPES buffer) was added to every well as the culture medium, and seeded samples were returned to the incubator to enable attachment.

4.2.4 MTT Assay

The MTT assay is a widely used colourimetric assay to examine cell viability. During the assay, MTT is added to cells where it is absorbed by living cells and transformed into insoluble formazan crystals. Purple formazan crystals dissolve in 0.1N HCl / 2-propanol, and purple light absorption of the solution (wavelength 540nm) is linearly correlated with cellular metabolic activity (169). As a result, a viable cell number can be quantitatively assessed through measurement of the purple light absorbance using a GloMax®-Multi Microplate Reader (Promega).

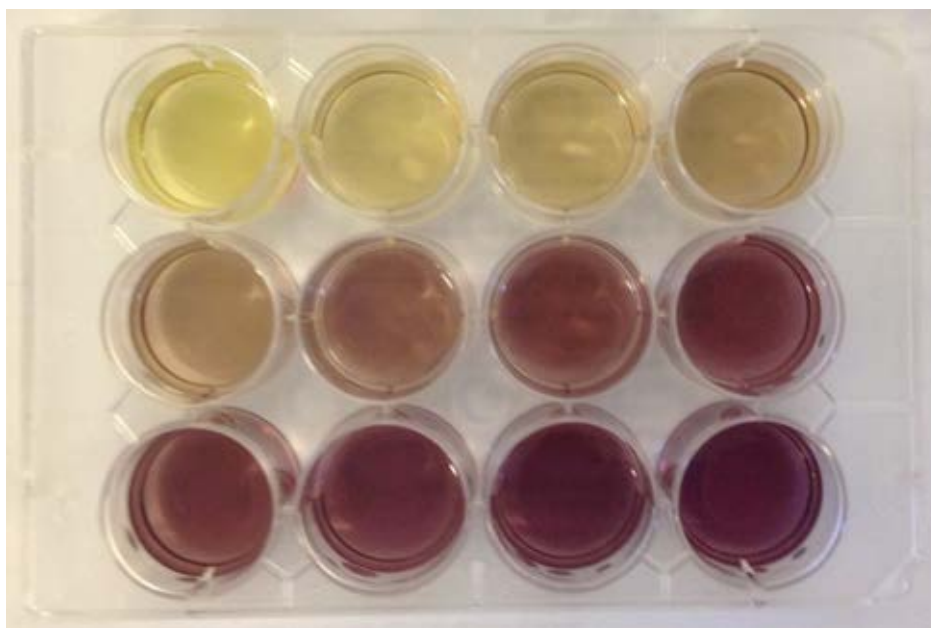


Figure 4.8: Formazan crystals dissolved in MTT solution

The optical density of purple light indicates the viable cell number in each well.

Before performing an MTT assay, the relationship between the specific cell number and MTT absorbance was established through a calibration process. A series of wells with cell numbers ranging from 1×10^3 to 1×10^6 were cultured in a standard 12-well culture plate; one well contained only the cell culture medium and acted as the background control. Cells were incubated under appropriate conditions for 24 hours and the MTT assay performed for each well. Stock MTT solution (5 mg MTT powder [Sigma] per 1 ml PBS) was added to each well and mixed with the culture media at a concentration of 100 μ l per 1 ml media. After adding MTT, the cell culture plate was returned to the incubator for 4 hours at 37°C. Next, 1 ml of formazan solvent (0.1N HCl in isopropanol) was added to each well and then mixed for 2 minutes to dissolve the formazan crystals. The example shown in Figure 4.8 demonstrates that the purple colour was darker when there was a higher density of viable cells. The formazan solution was transferred to a 96 well plate, and absorbance data were acquired via a plate reader. Values from triplicate readings were averaged, and the average absorbance value from the control well was subtracted. Absorbance readings were then plotted

against the known cell number density. An example MTT calibration curve for CTF cells is shown in Figure 4.9.

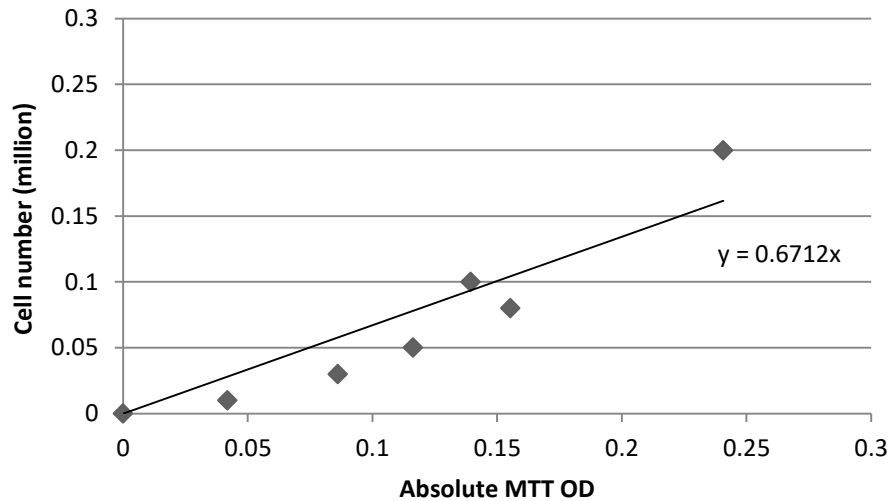


Figure 4.9: Example MTT calibration curve for CTF cells

The MTT assay for the actual experiments was performed 24 hours after cell seeding on the substrates. Seeded sample substrates were taken from the incubator, and washed gently with PBS to remove unattached cells, and an MTT assay was then performed following the standard procedure as described in the calibration process. Cell viability data were calculated using the measured absorbance data and the MTT calibration curve for the corresponding cell type.

4.2.5 Statistical Analysis

In addition to a qualitative comparison between surface characteristics and cell attachment, a statistical analysis was applied to establish a quantitative correlation. In the statistical analysis cell numbers calculated from the MTT assay were chosen as the dependent variable, representing the initial cell attachment for different samples. The attraction force, adhesion force, adhesion energy and surface roughness of different samples were selected as parameters to be assessed. A linear regression was performed using Stata 12 software, and the significance of the correlation between the attached cell

numbers and different parameters (adhesion force, attraction force, adhesion energy and surface roughness) is presented as p -values.

4.3 Results and Discussion

4.3.1 Treated Glass

Treated glass samples were tested repeatedly using both qualitative and quantitative approaches for an in-depth exploration of the hypothesis. Averaged EDS results from three repeating tests for the treated glass samples are shown in Figure 4.10. As can be seen, there was no statistically significant difference ($p > 0.1$) between the three groups, which meant the treatment of the glass sample surface minimally affected the atomic composition.

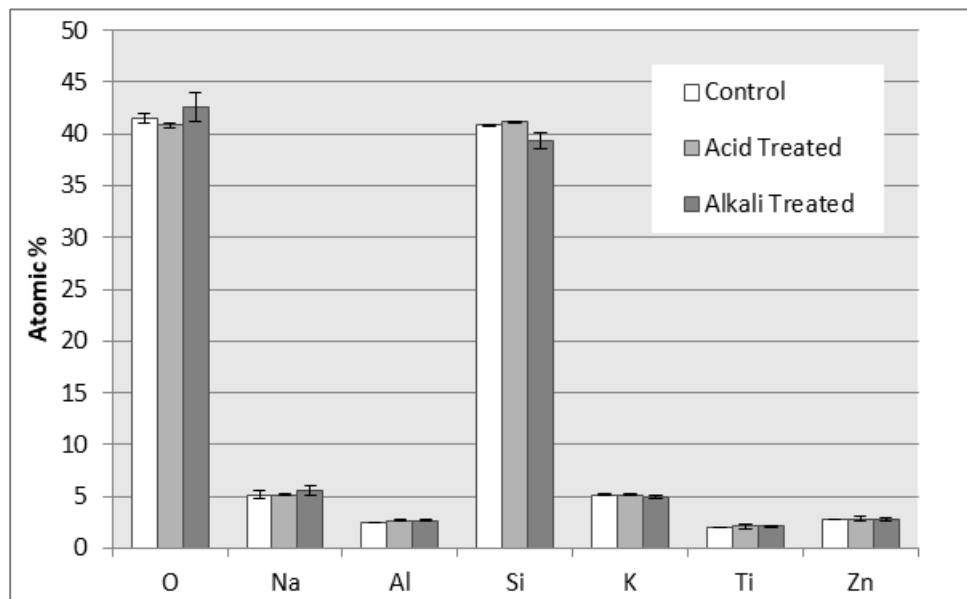


Figure 4.10: EDS results for the chemical composition of treated glass sample surfaces

The chemical composition of the glass samples were examined by EDS. The averaged atomic percentage is presented. (Mean \pm SD, N = 3)

The surface mechanical characteristics of the glass samples were measured by the AFM indentation method. Two different samples were selected for each group (control, acid treated and alkali treated separately). Five random testing positions with a $10 \mu\text{m} \times 10$

μm area each were selected on each sample, and 256 indentations were performed on each testing position. The measured adhesion force and RMS roughness are presented in Figure 4.11. On average, both treatments to the glass slide increased the surface adhesion force dramatically, from 14.45 nN to 208.88 nN for acid treated samples and to 97.35 nN for alkali treated samples. Both surface treatments also reduced the surface roughness to about half that of an untreated sample, and there was no significant difference between acid treated samples and alkali treated samples regarding surface roughness.

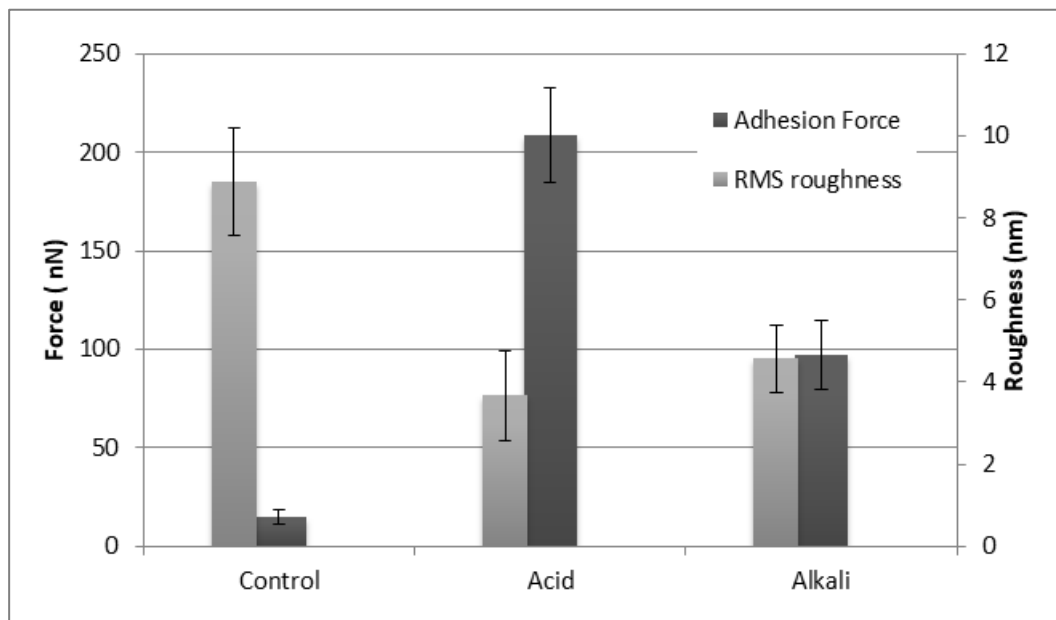


Figure 4.11: Adhesion forces and surface roughness of glass samples

The measurements were taken by AFM in the contact mode. Two samples were prepared for each group, and five random test positions were chosen on each sample. Each test position was divided by a 16×16 matrix, i.e. 256 measurements were taken at each test position. (Mean \pm SD, N = 2560) For roughness, each test position has one measurement. (Mean \pm SD, N = 10)

Following the mechanical tests of the glass samples, cell culture experiments were conducted. MC3T3 cells were cultured on glass samples for 24 hours, and the cultured samples were gently washed to remove unattached cells. An MTT assay was performed to determine attached viable cell numbers for each sample. Because the immobilised glass samples did not cover the entire base of the culture wells (Figure 4.1), the actual

cell number on the glass samples was calculated by subtracting the projected cell numbers on the remaining PDMS surfaces from the total cell number, as shown in Figure 4.12. Cell attachment density on the PDMS surface can be calculated from the attached cell number on the PDMS negative control group, using equation 4.1:

$$\text{Cell density on PDMS} = \text{Cell number on PDMS} / \text{cell culture well area} \quad (4.1)$$

$$\text{Attached cell number on glass sample} = \text{Total cell number} - \text{PDMS cell density} \times (9.6 - 4.84) \quad (4.2)$$

Assuming that the cell attachment density on PDMS surfaces remains the same, the cell number on the exposed PDMS zone was calculated using the PDMS cell density multiplied by the PDMS area (whole well area 9.6 cm² minus glass sample area 4.84 cm²). The attached cell number on the glass sample could then be calculated by subtracting the PDMS cell number from the total cell number (equation 4.2).

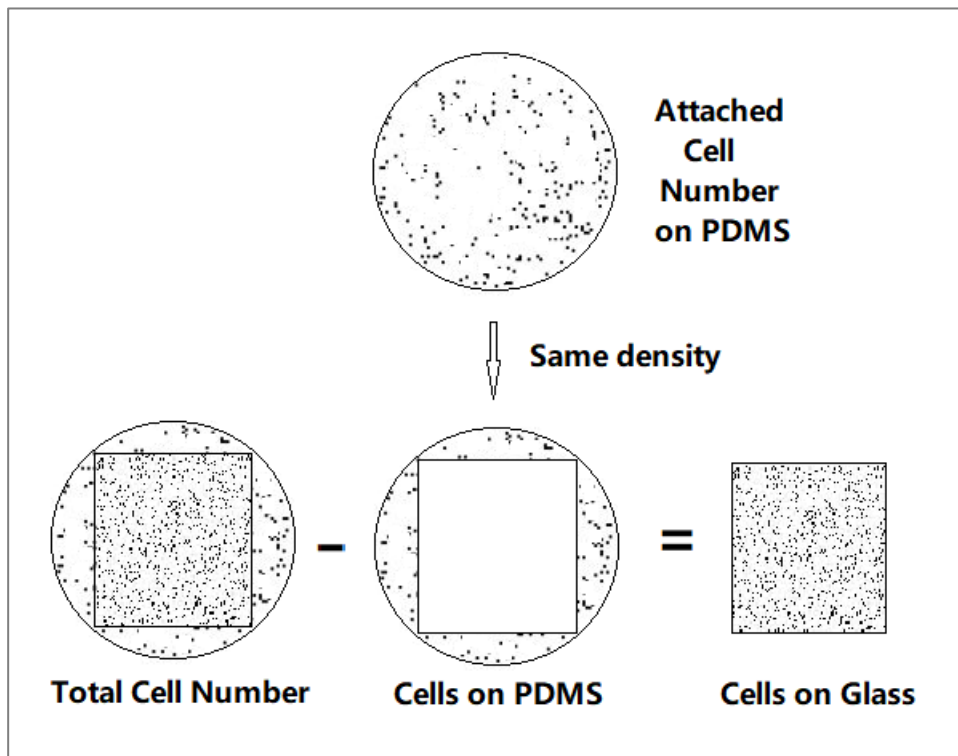


Figure 4.12: Cell number calculation for the glass samples

To make a comparison between different test conditions, cell attachment data was presented as a percentage rather than cell numbers. The cell attachment percentage was calculated as the attached viable cell number divided by the initial seeding cell number. Figure 4.13, Figure 4.14, Figure 4.15 and Figure 4.16 present the comparisons between the different surface characteristic parameters and two sets of MC3T3 initial cell attachment results, one for a high seeding density and one for a low seeding density. It can be observed that cell attachment after one day was generally low for both groups, and it could be due to the serum-free culturing condition and the PBS wash off before the MTT assay. Between 18% and 40% of MC3T3 cells attached to the glass samples after 24 hours with the high seeding density group resulting in higher cell attachment than the low seeding density group for all the glass samples.

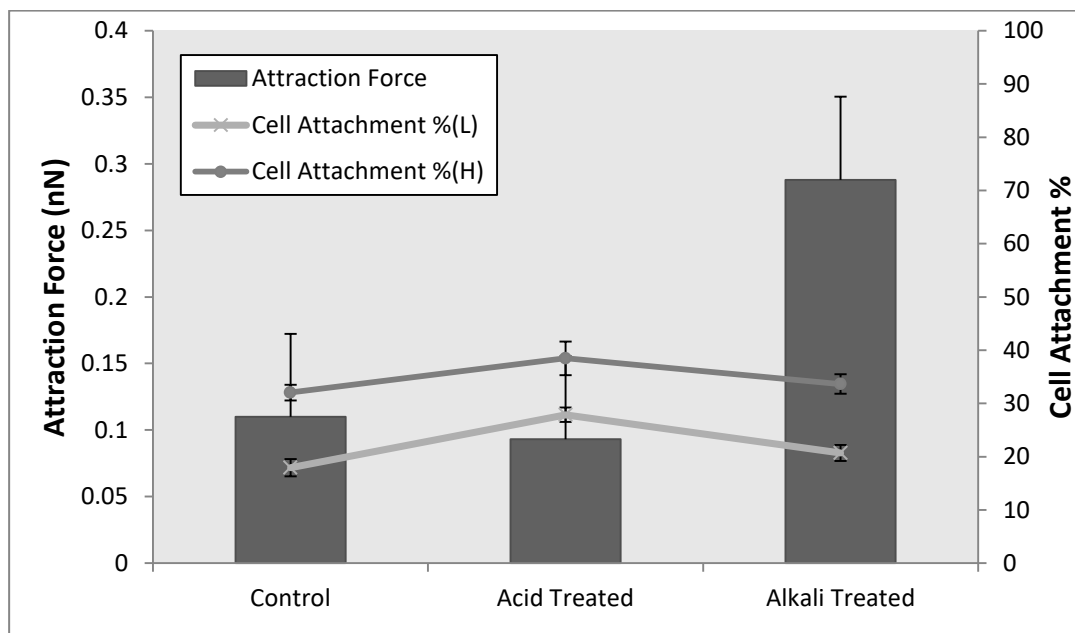


Figure 4.13: Surface attraction force and cell attachment percentage for treated glass samples

Surface attraction forces (bars) were measured by AFM. (Mean \pm SD, N = 2560) MC3T3 cell attachment percentages (lines) were calculated via an MTT assay, and two sets of results are presented: one for a high seeding density (marked as H group) and one for a low seeding density (marked as L group). For the cell attachment experiments, three samples were prepared for each group and were cultured under the same conditions at the same time. During the MTT assay, optical density measurements were repeated three times for each sample. (Mean \pm SD, N = 9)

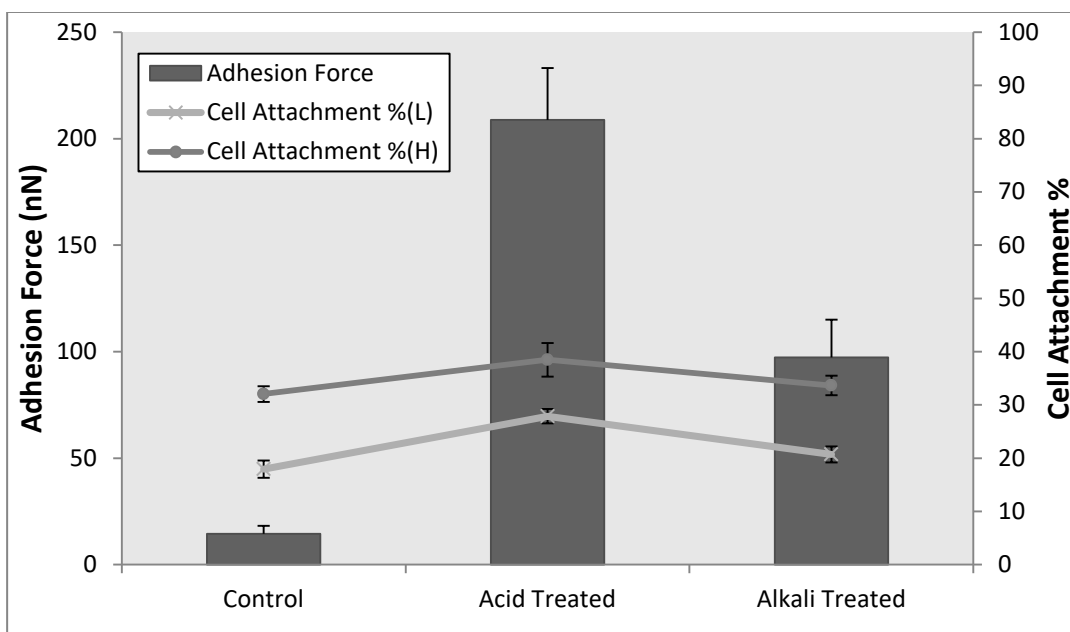


Figure 4.14: Surface adhesion force and cell attachment percentage for treated glass samples

Surface adhesion forces (bars) were measured by AFM. (Mean \pm SD, N = 2560) MC3T3 cell attachment data (lines) was calculated via an MTT assay. (Mean \pm SD, N = 9)

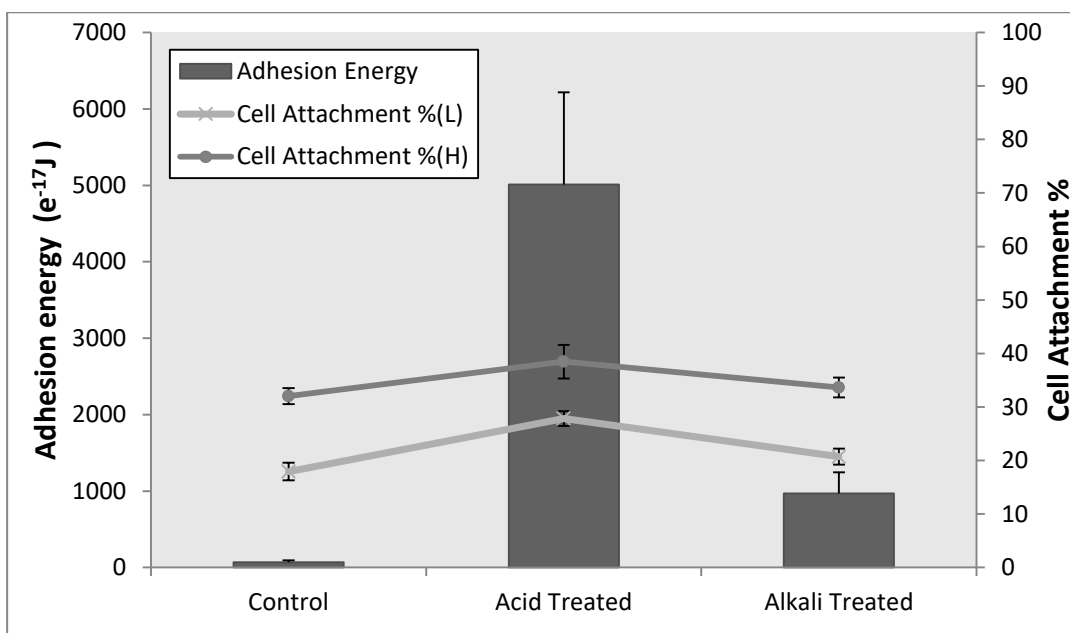


Figure 4.15: Surface adhesion energy and cell attachment percentage for treated glass samples

Surface adhesion energy data (bars) was measured by AFM. (Mean \pm SD, N = 2560) MC3T3 cell attachment data (lines) was calculated via an MTT assay. (Mean \pm SD, N = 9)

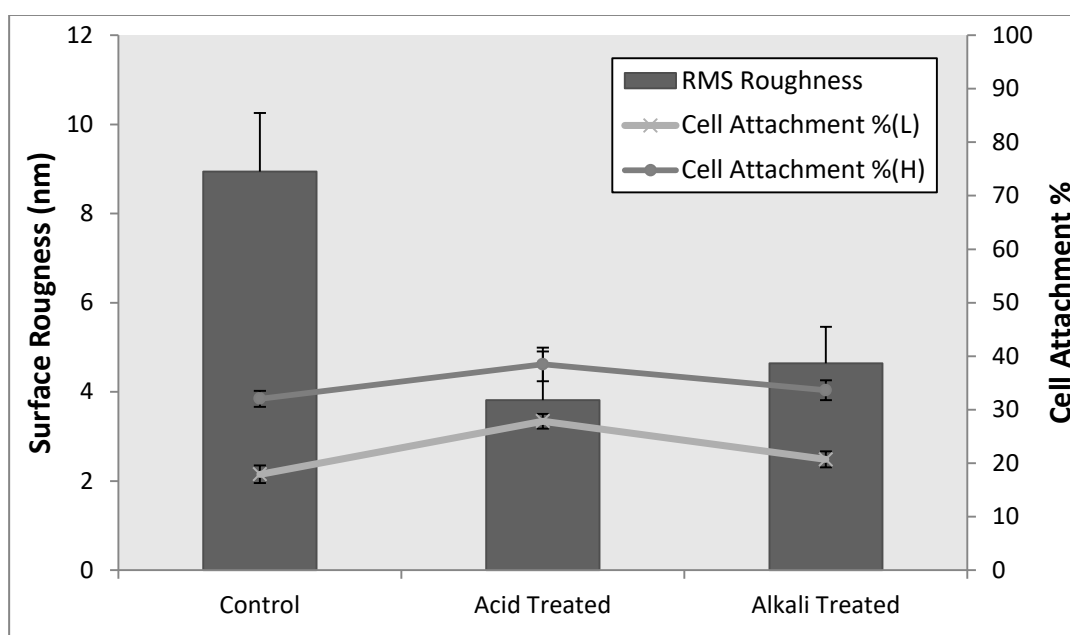


Figure 4.16: Surface roughness and cell attachment percentage for treated glass samples
 The surface roughness (bars) was measured by AFM. (Mean \pm SD, N = 2560) MC3T3 cell attachment data (lines) was calculated via an MTT assay. (Mean \pm SD, N = 9)

The four surface characteristics measured for glass samples were surface attraction force, surface adhesion force, surface adhesion energy, and surface roughness, and these were compared to the initial cell attachment percentage as shown in Figures 4.13, 4.14, 4.15, and 4.16. It can be observed that the adhesion force and adhesion energy are correlated to each other, but not to the attraction force. Samples in both the treated groups showed a greatly increased adhesion force and adhesion energy compared to the control group. Acid treated samples showed the largest adhesion force and adhesion energy of 208.88 nN and 5.012×10^{-14} J, respectively. Meanwhile alkali treated samples had an adhesion force roughly half that of the acid treated samples and an adhesion energy one-fifth of the acid treated samples. The untreated glass sample had a small adhesion force of 14.45 nN and an adhesion energy of 6.9×10^{-16} J. It can be noted from Figure 4.14 and Figure 4.15 that the average cell attachment percentage values between different glass samples follows the adhesion force and adhesion energy, as

these increase or decrease in both the high and low density seeding groups. However, cell attachment values did not follow the qualitative trend in changes to the attraction force as shown in Figure 4.13. The alkali treated samples had larger attraction forces with an average of 288 pN, whereas the control and acid treated samples were about 100 pN, while cell attachment was lower than for the other groups. Therefore, it can be said that attraction force contributes little to cell attachment. From Figure 4.16 it can be seen that cell attachment varies with the value of surface roughness. From this qualitative comparison, it was concluded that MC3T3 cell attachment corresponds with the surface adhesion force and adhesion energy of glass substrates under serum-free culture conditions.

In addition to the qualitative comparison, a quantitative assessment was performed by statistical regression analyses, in which the correlation between several measured surface characteristics and the cell attachment percentage was tested. The *p*-value is a statistical parameter which determines the significance of the hypothesis, and in this case it indicates the correlation between dependent and independent variables. The *p*-value is a number between 0 and 1, and a small *p*-value (typically ≤ 0.05) indicates strong evidence of a correlation between the dependant and independent parameters. The statistical analyses are shown in Table 4.2, from which it can be seen that the adhesion force was the only tested parameter that was significantly correlated with the dependent variable ($p < 0.01$); adhesion energy was only weakly correlated with cell attachment.

Table 4.2: Statistical correlation between the tested surface parameters and the independent variable cell attachment

	<i>p</i> -value
Adhesion force	$p < 0.01$,strongly correlated
Attraction force	Non-significant
Adhesion energy	$p < 0.1$,weakly correlated
RMS roughness	Non-significant
Other untested factors	Non-significant

Another set of AFM tests was performed on treated glass samples immersed in DMEM solution. As shown in Figure 4.17, the adhesion forces decreased by around three orders of magnitude compared to those measured under ambient conditions due to the screening effect of the electrolyte. However, the trend in adhesion force changes remained similar to under ambient conditions (Figure 4.14). The cell attachment of both high-density and low-density seeding also followed the adhesion force change.

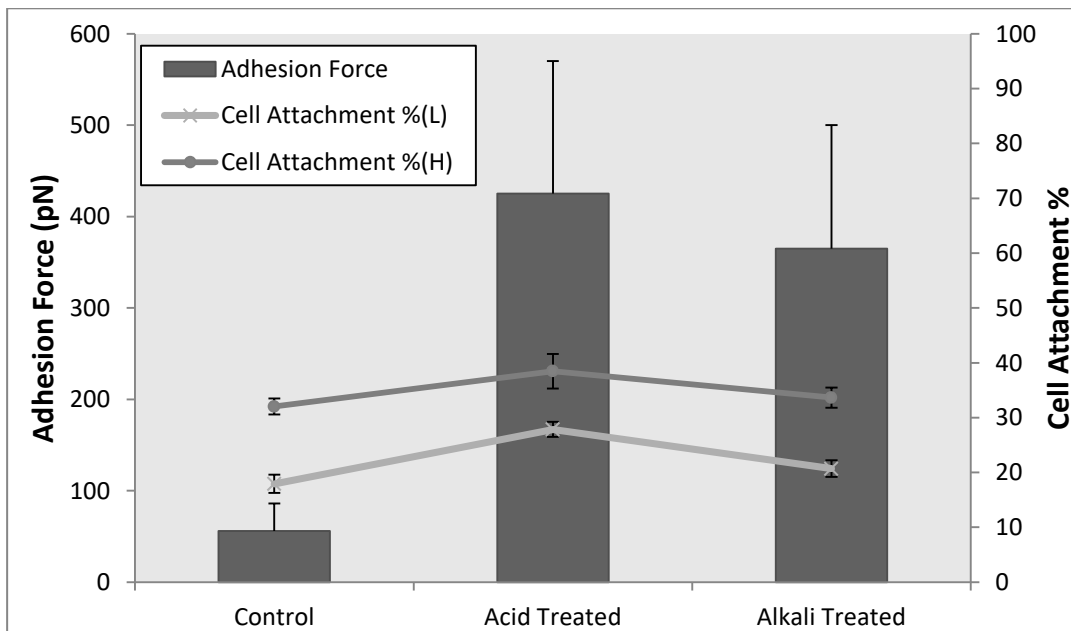


Figure 4.17: Surface adhesion forces when treated glass samples were immersed in DMEM and associated cell attachment data

Surface adhesion forces (bars) were measured by AFM. (Mean \pm SD, N = 2560) MC3T3 cell attachment data (lines) was calculated via an MTT assay. (Mean \pm SD, N = 9)

4.3.2 Cell Attachment of Other Cell Types

Further tests were carried out by seeding three more types of cells onto the treated glass samples under the same conditions as in the previous tests with MC3T3. MEC and CTF were cultured using a high seeding density (2×10^5 cells per well) and a low seeding density (1×10^5 cells per well) separately. Similar to the MC3T3 experiments, each test condition had three repeats carried out in parallel. In contrast, the cell seeding experiment using BMSC was performed only once due to their limited availability.

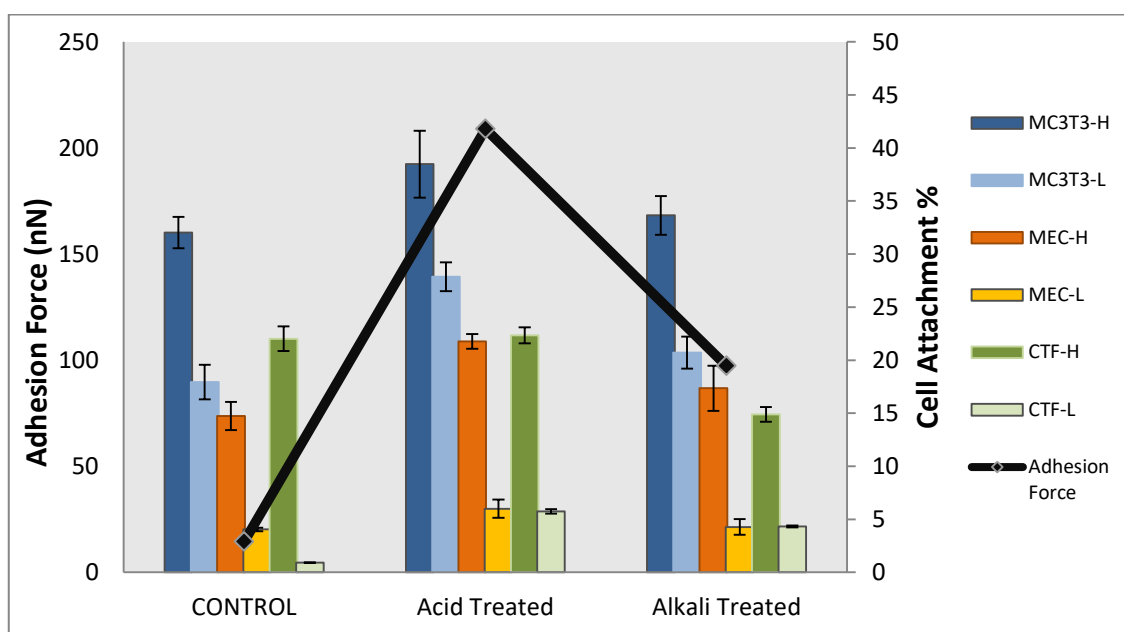


Figure 4.18: Surface adhesion forces and cell attachment of MC3T3, MEC and CTF on treated glass samples

Averaged surface adhesion forces (line) were measured by AFM. (N = 2560) Cell attachment percentages (bars) were calculated via an MTT assay. Two sets of results are presented for each cell type: one with high seeding density (marked H) and one with low seeding density (marked L). For the cell attachment experiments, three repeat tests were carried out, while the MTT assay optical density measurements were repeated three times for each sample. (Mean \pm SD, N = 9)

Generally, the cell attachment percentage on the glass samples was not high (below 40 % in every test), which is possibly due to the serum-free culture conditions and the PBS wash before performing the MTT assay. From Figure 4.18 it can be seen that a high seeding density had a higher likelihood of attachment, and this holds true for all

MC3T3, MEC and CTF experiments. The correlation between the cell attachment of different cell types and surface adhesion forces can be qualitatively observed from Figure 4.18, where the cell attachment percentages of MC3T3 and MEC on different glass substrates follows the trend of the adhesion forces as they increase or decrease. Similar patterns exist in both the high and low density seeding groups; however, the results for the high density seeding of CTF cells differed. On the control glass sample tests, there was increased attachment following high density CTF seeding (dark green, Figure 4.18) compared to the treated samples; while low density CTF seeding (light green, Figure 4.18) yielded similar findings to other cells.

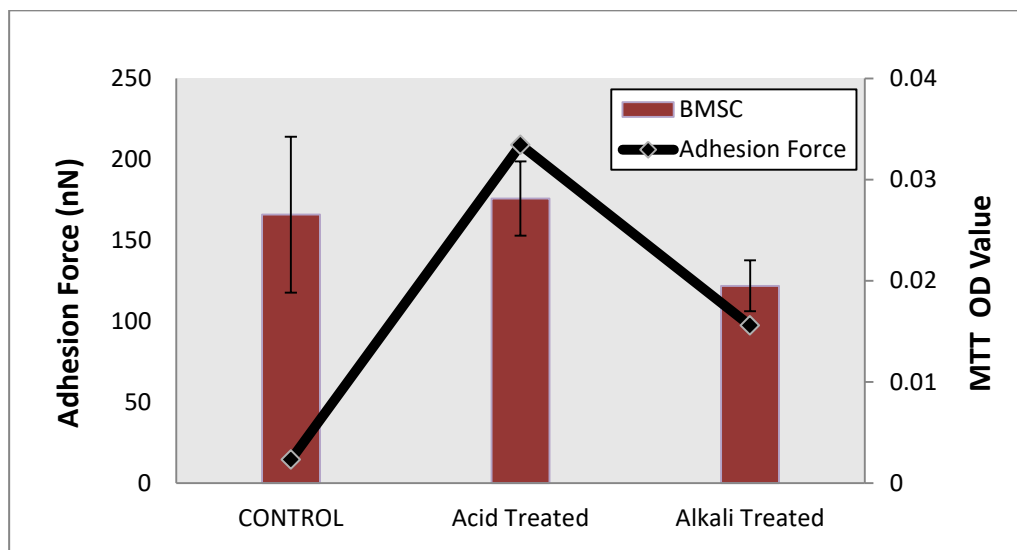


Figure 4.19: Surface adhesion forces and cell attachment of BMSC on treated glass samples

Averaged surface adhesion forces (line) were measured by AFM. (N = 2560) Cell attachment (bars) of BMSC is shown as the MTT assay optical density value. (Mean \pm SD, N = 9)

Due to the limited availability of BMSC, an MTT calibration curve for this cell type was not obtained. Consequently, MTT OD values represented in Figure 4.19 as a linear estimation of viable cell numbers. The cell seeding experiment using BMSC was performed only once with three repeating samples. From Figure 4.19 the MTT results for BMSC did not follow the changes in surface adhesion force for the different glass

samples. This could have been due to the unstable attachment of primary cells which were more sensitive to external stimuli (large error bars). What is more, prior experience with BMSC attachment *in vitro* has shown low attachment under serum-free conditions.

4.3.3 Initial Cell Attachment on Treated Titanium Samples

Ti and its alloys have been widely adopted in dental and bone implantations. Alkali and heat treatment were methods developed by Kim et al. (170) to modify the Ti surface for enhancement of bone-bonding, potentially for bone replacement applications. This section presents the assessment of treated Ti surfaces from the surface adhesion force aspects and the effect on cell attachment.

SEM images of treated Ti sample surfaces are shown in Figure 4.20 for (a) alkali treated Ti, and (b) alkali-heat treated Ti. Kim et al. (171) found that by reacting with NaOH, a layer of sodium titanate hydrogel formed on the surface of the sample with a porous interconnected surface structure, and after alkali and heat treatment the surface sodium titanate had reached an amorphous densified state. In his research thin-film X-ray diffraction and Raman spectroscopy were applied to assess the surface composites. Figure 4.20 shows the surface structures of the treated Ti samples manufactured in this project, and these match the experimental results of other researchers well (170-172).

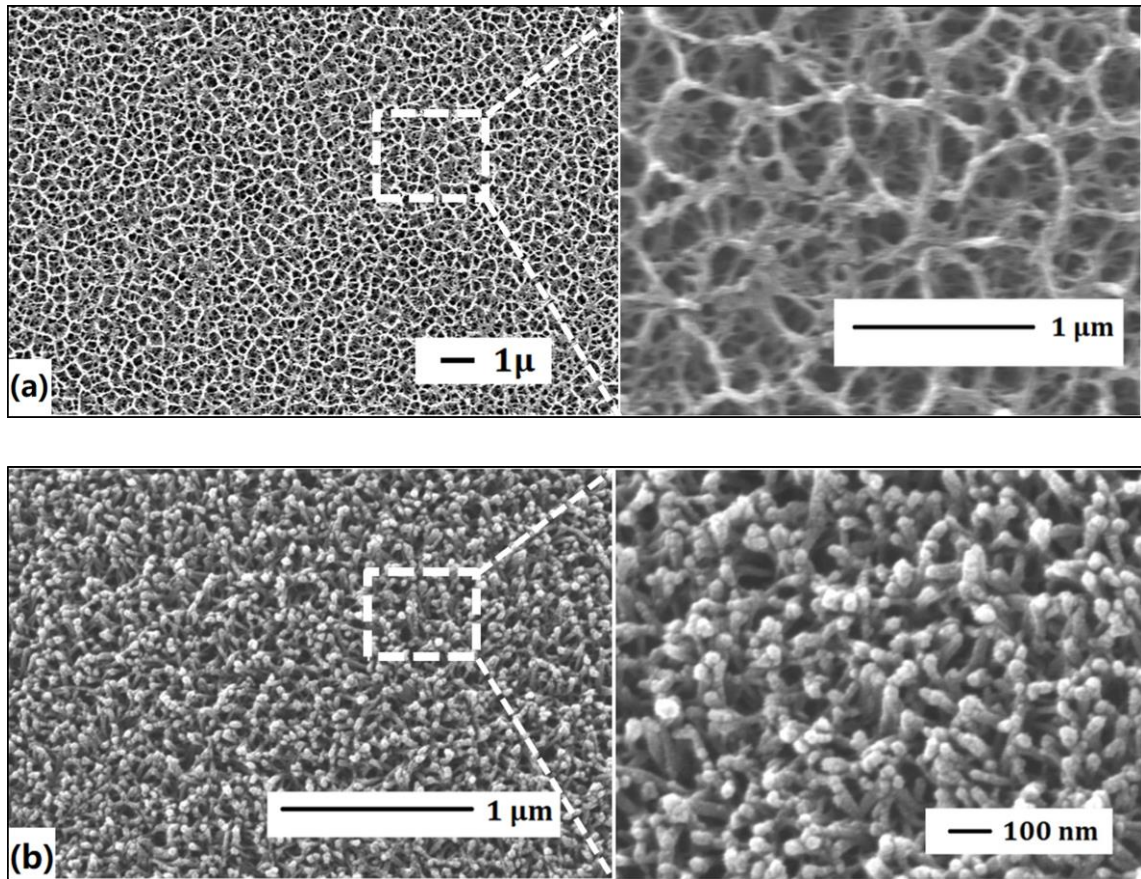


Figure 4.20: SEM images of the treated titanium surfaces

(a) alkali treated Ti; (b) alkali and heat treated Ti

The adhesion forces and surface roughness of the treated Ti samples were studied using the AFM indentation technique, and the results are shown in Figure 4.21. The surface characteristics of the control and alkali treated samples were measured one day after the treatment, whereas measurement of the alkali-heat treated samples was delayed for two weeks after the treatment due to a fault with the AFM system rendering it unusable.

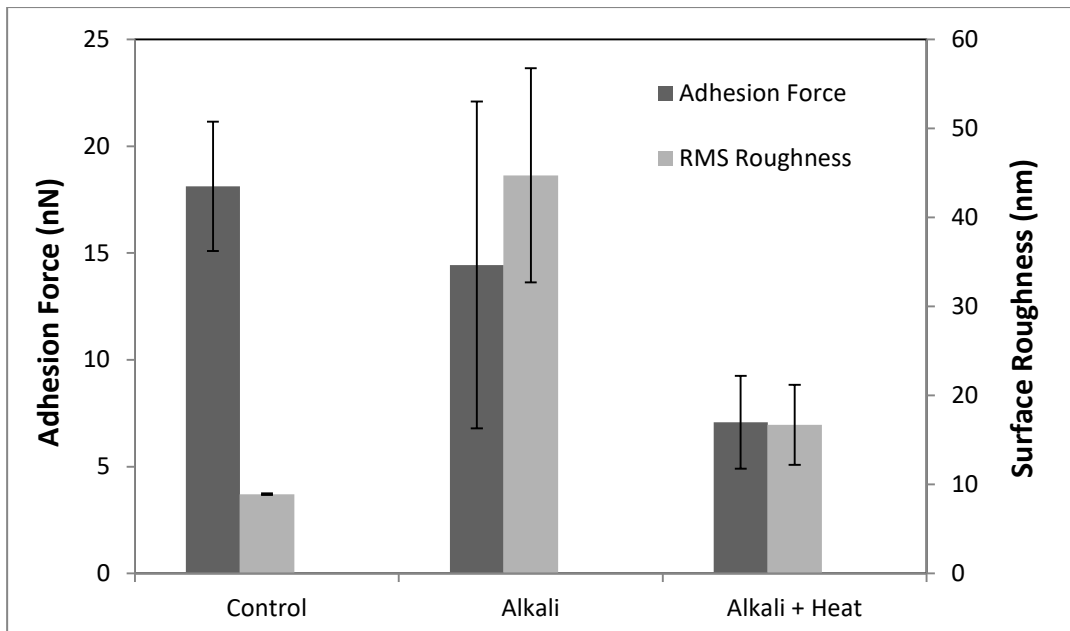


Figure 4.21: AFM measurements of the surface adhesion force and surface roughness of treated titanium samples

Measurements were taken by AFM in the contact mode. Two samples were prepared for each group, and five random test positions were chosen on each sample. Each test position was divided by a 16×16 matrix, i.e. 256 measurements were taken at each test position. (Mean \pm SD, N = 2560) For roughness tests, each test position has one roughness measurement. (Mean \pm SD, N = 10)

By comparing the surface adhesion forces for the control and both treated groups, it can be noted that the adhesion force was reduced following treatment. The average surface adhesion force of the control Ti surface (18.12 nN) was slightly higher than that of the alkali treated samples (14.44 nN); however, the difference was insignificant due to the large variance in the measurements for the alkali treated sample surface. The standard deviation of the adhesion force was 53% of the mean, which suggests a wide distribution of values on the porous surface structure, as shown in Figure 4.22. It can be observed from Figure 4.22(a) the AFM topography and (b) surface adhesion map that the porous surface structure caused peaks and valleys of adhesion forces (shown as red circles). A histogram of the surface force value distribution showed a long tail (Figure 4.22d). The surface roughness of the alkali treated samples was nearly five times the value of untreated Ti, which was as expected.

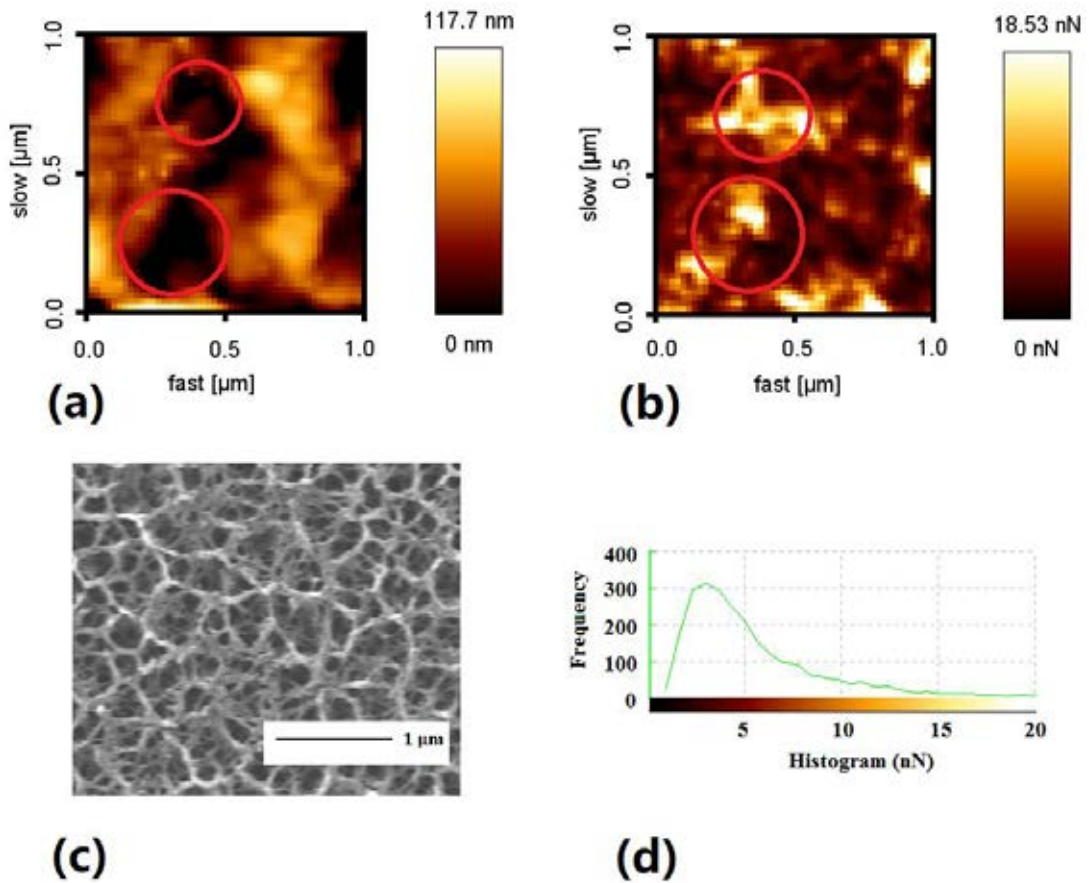


Figure 4.22: Surface characteristics of the alkali treated Ti surface

Alkali treated Ti samples were tested by AFM in the contact mode and an SEM scan separately. AFM results were acquired from the same $1\ \mu\text{m} \times 1\ \mu\text{m}$ scanning area while the SEM image was taken from another spot. (a) AFM measured surface topography; (b) AFM measured surface adhesion force map; (c) SEM image; (d) Histogram of surface adhesion force distribution.

For the alkali-heat treated samples (Figure 4.23), the average surface adhesion decreased further to 7.07 nN, while the variance in the adhesion force also decreased after furnace heating, as reflected by the standard deviation decreasing to 31% of the mean value. The surface roughness (16.7 nm) reflects that the surface topographical structures are less complicated than those of the alkali (60.57 nm) treated samples, but it was still rougher than that of the control samples (8.9 nm).

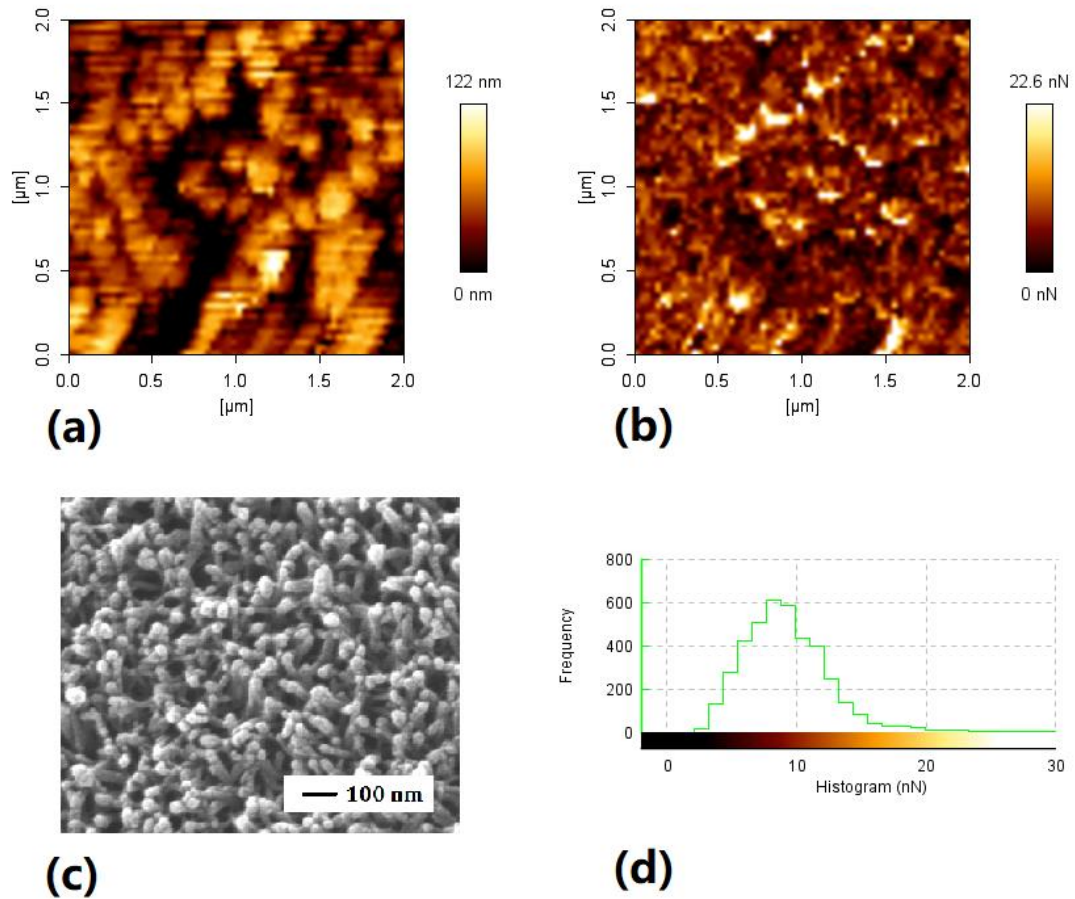


Figure 4.23: Surface characteristics of alkali-heat treated Ti surface

Alkali-heat treated Ti samples were tested by AFM in the contact mode and an SEM scan separately. AFM results were acquired from the same $2\ \mu\text{m} \times 2\ \mu\text{m}$ scanning area while the SEM image was taken from another spot. (a) AFM measured surface topography; (b) AFM measured surface adhesion force map; (c) SEM image; (d) Histogram of surface adhesion force distribution.

In vivo bone bonding experiments of treated Ti were performed by Nishiguchi et al. (47) in 8 and 16 weeks implantation experiments. The results showed that long-term osseointegration properties were greatly enhanced by alkali-heat treatment compared to only alkali treated samples; the commercially pure Ti group showed the poorest bone bonding. Regardless of the *in vivo* long-term performance reported in the literature, it remains worthwhile to examine the hypothesis of this chapter concerning whether the surface adhesion force plays a dominant role during the initial cell attachment stage. To examine the correlation between surface adhesion force and initial cell attachment,

biological data for treated Ti surfaces are required. Unfortunately, these experiments could not be carried out during this project due to the limited experimental conditions and time. A literature review was therefore undertaken to find data for comparison. Due to the unique experimental design of this project, it is difficult to find experiments carried out by other researchers with the same experimental design, for example, cell type, cell culturing conditions, medium composition, cell measurement techniques etc. Consequently, the literature on attached viable cells with similar test conditions was searched, and the results were used for comparison with the surface adhesion data acquired in this project.

In the work of Maitz et al. (173), the lactate dehydrogenase (LDH) activity of rat bone marrow cells cultured on Ti and alkali treated Ti surfaces for 5 hours using serum-free medium was measured. The authors calculated the ratio of cytolytic cells to the whole seeding population as determined by LDH release, and the attached viable cell percentage could thus be estimated through subtraction of the cytolysis percentage from 100%. From Figure 4.24, it can be seen that the viable cells on the alkali treated samples decreased slightly from around 94% to 92% in comparison to the pure Ti group (cytolysis increased from around 6% to 8% of the mean value). Compared to the surface forces, the average adhesion force of alkali treated Ti is around 80% of the Ti group.

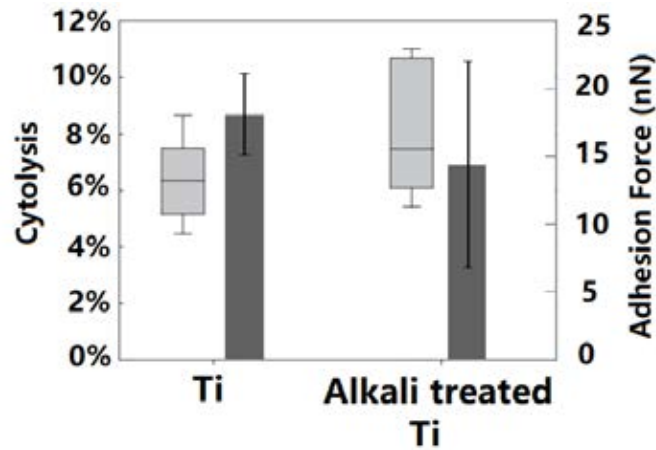


Figure 4.24: Surface adhesion force and cytolysis of rat bone marrow cells seeded on Ti and alkali treated Ti surfaces (173)

The surface adhesion forces (bars) were measured by AFM in the contact mode. The cytolysis data of rat bone marrow cells are shown as a boxplot, with the box representing the lower and upper quartiles, the whiskers the 90% range, and the band inside the box indicating the median.

The comparison using the above literature data is not perfect, due to the difficulty in identifying cell culture data under the same testing conditions. Thus, cell seeding experiments using a consistent methodology is suggested for future work in order to establish systematic testing of the hypothesis.

4.3.4 Tests of Other Biomaterials

Finally, to further examine the correlation between surface adhesion force and initial cell attachment more broadly, several other biomaterials were investigated. The materials studied were PDMS, glass, polystyrene, Ti, hydroxyapatite and Al₂O₃ ceramic. Surface adhesion forces were measured for these biomaterials under standard ambient conditions and then compared to cell attachment data.

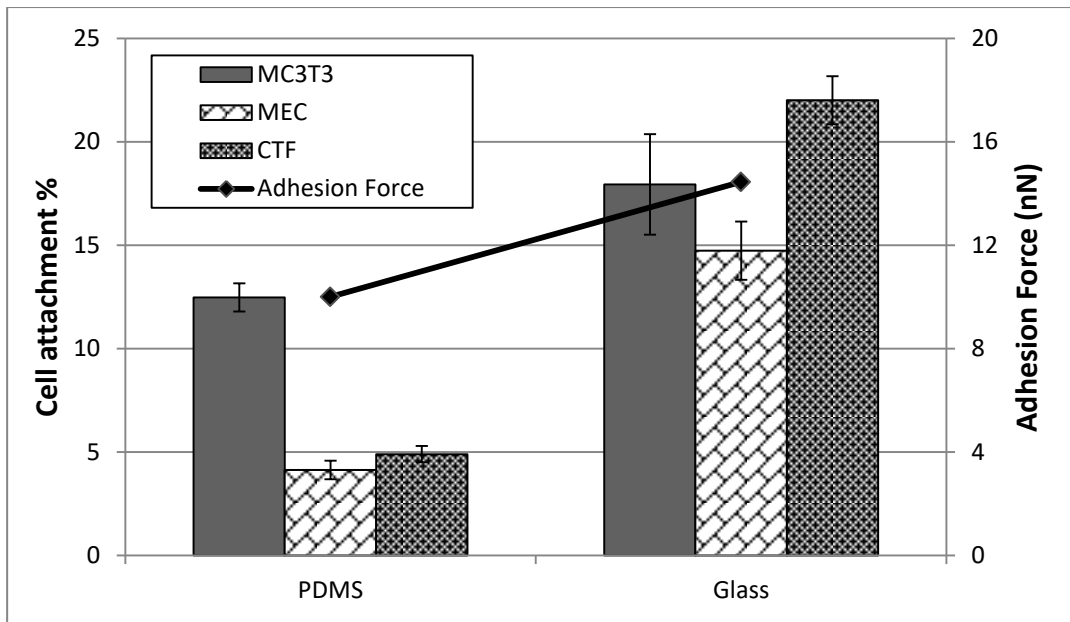


Figure 4.25: Surface adhesion forces and initial cell attachment percentage of MC3T3, MEC and CTF on PDMS and glass surfaces

Averaged surface adhesion forces (line) were measured by AFM. (N = 2560) Cell attachment percentages (bars) were calculated via an MTT assay. (Mean ± SD, N = 9)

Initially, a comparison was made between PDMS and borosilicate glass. PDMS had been used as a negative control in the cell seeding experiments in section 4.3.1, and viable attached cell numbers on PDMS were measured via an MTT assay and compared to those for borosilicate glass. Figure 4.25 presents the initial cell attachment of MC3T3, MEC and CTF on PDMS and glass surfaces. All three cell types showed significantly more ($p < 0.1$ for MC3T3 groups, $p < 0.01$ for MEC and CTF) cell attachment on glass samples than PDMS, and the average adhesion force on glass also showed an increase of 44% compared to that on PDMS samples.

In the following sections, cell attachment results are extracted from the literature. As discussed in section 4.3.3, the data from the literature is not perfectly suited because other researchers have applied non-identical experimental conditions. However, their results can still be used as a comparison and can provide directions for future work. To make the comparison as realistic as possible, several criteria were applied in the

literature searching process: firstly, cell attachment data must have been extracted from experiments using serum-free culture; secondly, cell attachment data must have been acquired through direct cell seeding experiments; and finally, the initial cell attachment time must have been no longer than one day.

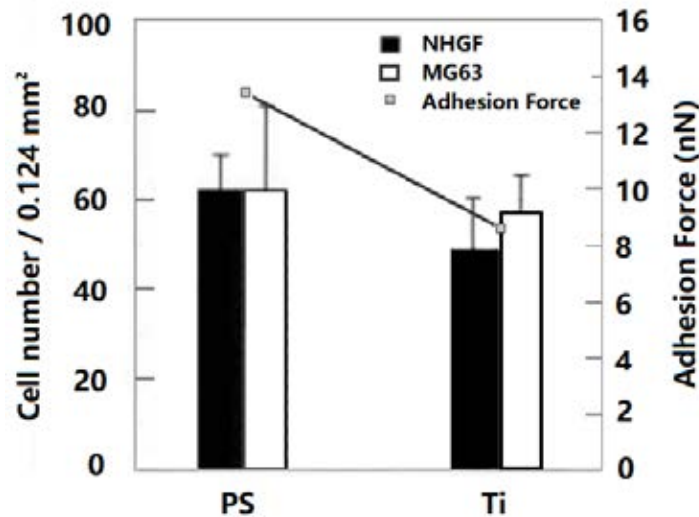


Figure 4.26: Initial cell attachment of NHGF and MG63 cells on PS and Ti surfaces, compared with surface adhesion forces (174)

Normal human gingival fibroblasts (NHGF) and osteoblast-like MG63 initial attachment on PS and Ti surfaces were reported by Park et al. (174), where cell attachment was measured via SEM cell counting 30 minutes after seeding in serum-free medium. Combined with the surface adhesion forces measured in this chapter, the results are shown in Figure 4.26, and as can be seen, initial attached cell numbers for both cell types were higher on the PS surface (NHGF: 62, MG63: 62) compared to the Ti surface (NHGF: 49, MG63: 57). The change in cell attachment between different surfaces generally followed the surface adhesion force values. The experiments carried out by Nebe et al. (175) showed a similar trend, but there was less attachment time, and a different assessment technique was utilised. In their work, 27% of human osteoblasts

attached to PS after 15 minutes of culture in serum-free DMEM, while only 15% remained on the Ti surface.

Okamoto et al. (176) showed how human osteoblast-like cells (HOS) attached to hydroxyapatite and Ti with or without surface treatment. Initial attachment of osteoblasts was measured by radioactive labelling 30 minutes after seeding, and as shown in Figure 4.27, cell attachment on Ti was 21% higher than on hydroxyapatite and approximately matched the change in surface adhesion force (27% higher).

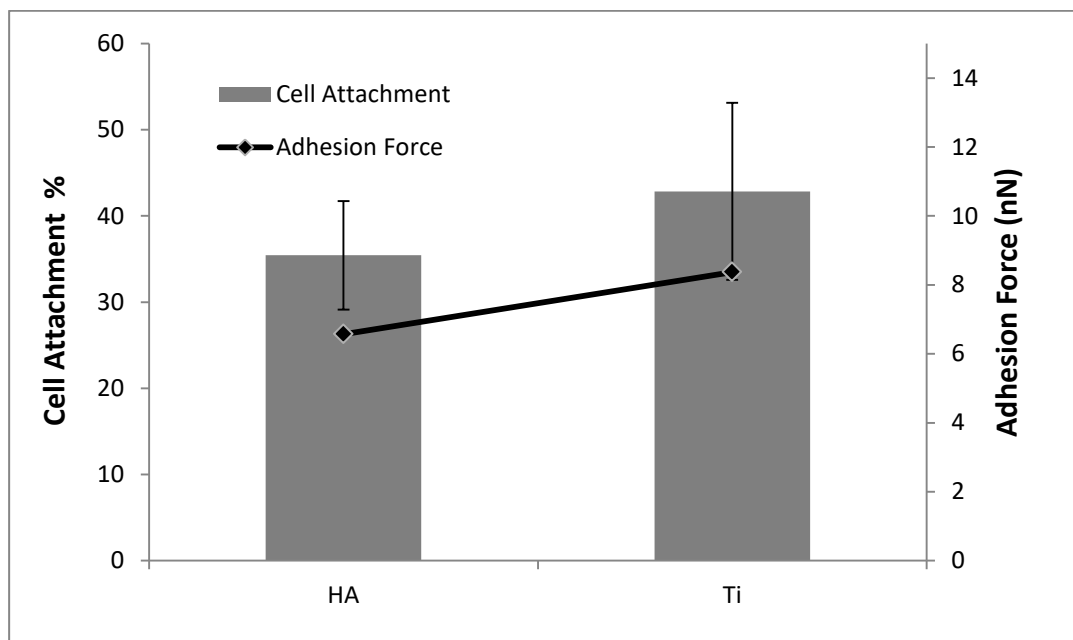


Figure 4.27: Surface adhesion forces and initial cell attachment of osteoblasts on hydroxyapatite and Ti (176)

Averaged surface adhesion forces (line) were measured by AFM. (N = 2560) Cell attachment percentages (bars) were calculated by counting radioactively labelled cells. (Mean \pm SD, N = 5)

Liu et al. (177) performed cell culture experiments on top of PDMS and Al₂O₃ ceramic, and initial attachment of MC3T3 cells was measured via an MTT assay one day after seeding. From Figure 4.28 it can be seen that alumina had a greater surface adhesion force (20 nN) compared to PDMS (10 nN), while cell attachment was insignificantly higher.

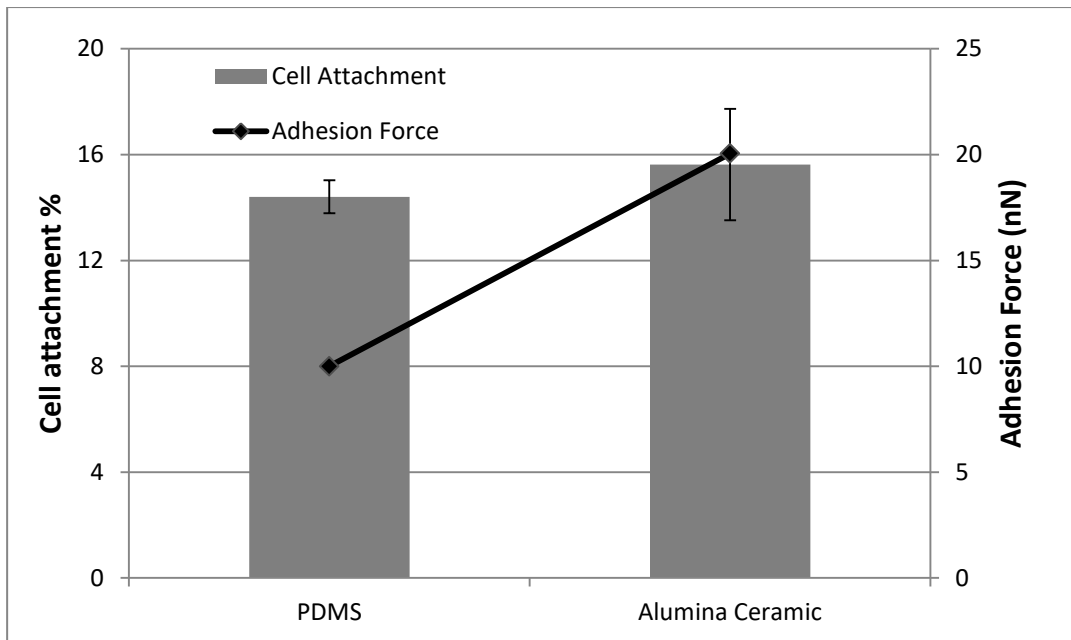


Figure 4.28: Surface adhesion forces and initial cell attachment percentage of MC3T3 on PDMS and alumina surfaces

Averaged surface adhesion forces (line) were measured by AFM. (N = 2560) Cell attachment percentages (bars) were calculated via an MTT assay. (Mean \pm SD, N = 9)

It can be summarised from the above comparisons that initial cell attachment in serum-free conditions is very loosely correlated to the surface adhesion force, which is supported by the data both from the author's experiments and from the literature.

Because of the unique design of these experiments, only limited experimental data were located within the literature. Although the available data are not perfect for comparison purposes due to different cell types and culture conditions used, they have been utilised as a reference for examining the hypothesis. These comparisons are in agreement with the experimental findings of this research and support the hypothesis to some extent.

4.4 Summary

Chapter 4 has presented an initial investigation into the correlation between the nanoforces on the substrate and cell attachment. A series of qualitative tests, comparing the AFM measured surface nanoforces and surface cell attachment have been carried

out. The first set of experiments was performed on treated glass samples. The AFM measured surface properties, including surface attraction force, surface adhesion force, surface adhesion energy, and surface roughness were qualitatively compared to MC3T3 cell attachment data as assessed via MTT assays. The comparison using bar charts showed that the initial cell attachment data generally follows the surface adhesion force, in other words, cell attachment will increase or decrease if the surface adhesion force increases or decreases. A further quantitative comparison between the cell attachment data and the surface characteristics was performed using regression analysis. The qualitative results show that the cell attachment data significantly correlates with the surface adhesion force and weakly correlates with adhesion energy; other parameters were not significantly correlated.

Further cell attachment experiments were conducted on treated glass samples using three more cell types, MEC, CTF and BMSC. Experiments using different cell seeding densities were tested separately for MC3T3, CTF and MEC, while only one seeding density experiment was carried out for BMSC. Cell attachment data were generally correlated with the values of surface adhesion force; however, the magnitude of the value change was not linear in some testing conditions. BMSC attachment experiments showed results with large standard deviations, which could have been caused by the unstable attachment of primary cells.

Experiments were then conducted on treated Ti samples. The alkali and heat treatment of Ti are approaches utilised to improve the bone bonding performance in medical applications, such as dental and bone implantations. *In vivo* experiments demonstrated that alkali and heat-treated Ti have significantly better bone bonding in long-term implantations. The SEM and AFM data acquired for alkali and alkali-heat treated Ti samples showed complex surface structures and corresponding adhesion force

distribution. With data extracted from other researchers' work, Ti showed better initial cell attachment than alkali treated Ti.

Finally, a survey of the literature was carried out for commonly utilised biomaterials, i.e. PS, Ti, PDMS, glass, hydroxyapatite and alumina ceramic surfaces. AFM indentations were performed on the surfaces of these biomaterials, and then cell attachment data from previously published studies were qualitatively compared with the AFM results. The data indicated that a possible correlation between surface nanoforces and cell attachment exists across a broad range of different materials.

Overall, the results showed some correlation between surface adhesion and initial cell attachment for common biological materials, which also held true for different types of cells. The results serve as an initial indication that in serum-free culture conditions the nanoforces on a substrate's surface may be an important factor for cell attachment. However, further experiments are needed on a broader range of materials and surface treatments to verify this hypothesis.

The findings in this chapter provide a convenient methodology to estimate how well cells can attach to a surface, and this methodology is further explored and tested using two novel graphene composite materials in the next chapter.

Chapter 5 - Cell Attachment to Graphene Composite

Materials

5.1 Introduction

This chapter presents the tests of the proposed hypothesis on relatively new nanomaterials. A graphene platelet based ceramic composite ($\text{Al}_2\text{O}_3/\text{GPL}$) was fabricated, and a porous three-dimensional graphene foam (3DGF) was obtained from the Department of Materials Science and Metallurgy, University of Cambridge. Several mechanical properties were assessed to establish the influence of graphene, and cell seeding experiments were conducted to check their potential for use in biological applications. As part of the biological assessment of these two new materials, the correlation between material surface nanoforces and cell attachment was examined. In the experiments, AFM was used to obtain a general idea of how well cells can attach to these new materials before *in vitro* tests were conducted. Based on the experimental findings, time-efficiency and cost-efficiency could be improved in the development of biomedical materials and devices.

The contents of this chapter are organised as follows. Firstly, background knowledge on the graphene and relevant composite materials is briefly introduced, and the potential applications of graphene in ceramics implantation and tissue engineering are discussed. The fabrication process of $\text{Al}_2\text{O}_3/\text{GPL}$ and 3DGF are then introduced in detail, followed by measurements of the mechanical properties of the new materials using AFM (JPK NanoWizard®II) and a universal testing system (Instron 6025). SEM images are presented in order to study the microstructural details of the materials and then finally direct cell seeding experiments are presented and discussed with quantitative

measurements from an MTT assay and a qualitative approach using live/dead fluorescence microscopy.

In the final section of this chapter, an empirical methodology developed from the results of Chapter 4 is discussed. In this methodology, the AFM-measured surface nanoforces are used as parameters to assess the initial cell attachment to these new materials. Currently, this methodology could not provide a precise prediction of how well cells can attach to a material; however, it can provide a general tendency concerning cell attachment for a group of materials without conducting any biological tests. Surface nanoforces of new graphene composite materials were measured and by comparison to the cell attachment results presented in this chapter, initial proof of feasibility for this methodology was established.

5.1.1 Background to Graphene Composite Materials

Graphene, an elemental monolayer of graphite, has drawn the attention of many material scientists and engineers since it was first fabricated in 2004 (178). It has been reported that graphene has some extraordinary physical properties compared to traditional materials, for example, Young's modulus of 1.0 TPa was measured by Lee et al. (179), while Bolotin et al. (180) recorded an electron mobility of $200,000 \text{ cm}^2\text{V}^{-1}\text{s}^{-1}$ at low temperature, and a thermal conductivity of $4.84 - 5.30 \times 10^3 \text{ W/mK}$ was reported by Balandin et al. (181)

The unique mechanical, electronic and optical properties of graphene have also been of interest to biologists. From enhancing traditional inert materials for supportive body structures to recently popular regenerative tissue engineering treatments, graphene has been tested as a biomaterial for use in many applications. Biological tests on graphene, have revealed that graphene-based materials either enhance mammalian cells' *in vitro*

viability (182) or caused a slight decrease during *in vitro* tests (183, 184), although several studies have reported that graphene-based materials caused a significant viability decrease (185-187). Limited *in vivo* testing has also yielded contradictory results depending on the dose and length of time the graphene material was applied (188-190). Stem cell differentiation behaviour was tested on graphene by Park et al. (191) using human neural stem cells and by Nayak et al. (192) using human mesenchymal stem cells (hMSC).

Graphene has been used to develop novel biological devices, for example, the possibility of applying graphene-based materials during regenerative tissue engineering has been explored (193-195). Drug delivery devices are another promising application, and many results have been generated, especially for the targeting of cancer cells (196-201). Based on graphene's functional surface and sensitive electrical properties, state-of-the-art biosensors have been developed to detect important biomolecules, such as growth factors (202) and proteins (203, 204). Graphene oxide is also a biosensor material for hormones (205), DNA (206) and toxic metal ion (207, 208) detection.

In this chapter, the potential applications of combining graphene with alumina ceramic and tissue engineering scaffolds were examined. Two materials were fabricated and investigated, Al₂O₃/GPL and porous 3DGF. A brief introduction to these two materials is given in the following sections.

5.1.2 Alumina Ceramic and Graphene Platelet

Alumina ceramic (Al₂O₃) has been extensively studied and utilised in biomedical applications due to its superior mechanical properties and chemical inertness (209-211). Ceramics and their composites are particularly well suited to dental treatments, such as dental implants (212-214), in orthopaedic surgery for joint prostheses, such as hip joints

(215) or knee joints (216), and in some other applications, including drug delivery devices, ocular implants and heart valves, etc. Table 5.1 shows some of the biological applications of ceramics and their composites.

Table 5.1: Biomedical applications of ceramics and composites
(210)

Applications	Biomaterial	Function
Artificial total hip, knee, shoulder, elbow, wrist	High-density alumina, metal bioglass coatings	Reconstructing arthritic or fractured joints
Bone plates, screws, wires	Bioglass-metal fibre composite, Polysulfone-carbon fibre composite	Repairing fractures
Intramedullary rods	Bioglass-metal fibre composite, Polysulfone-carbon fibre composite	Aligning fractures
Harrington rods	Bioglass-metal fibre composite, Polysulfone-carbon fibre composite	Correcting chronic spinal curvature
Permanently implanted artificial limbs	Bioglass-metal fibre composite, Polysulfone-carbon fibre composite	Replacing missing extremities
Vertebrae spacers and extensors	Al ₂ O ₃	Correcting congenital deformity
Spinal fusion	Bioglass	Immobilising vertebrae to protect the spinal cord
Alveolar bone replacements, mandibular reconstruction	Polytetra fluoro ethylene (PTFE) - carbon composite, Porous Al ₂ O ₃ , Bioglass, dense-apatite	Restoring the alveolar ridge to improve denture fit
Endosseous tooth replacement implants	Al ₂ O ₃ , Bioglass, dense hydroxyapatite, vitreous carbon	Replacing diseased, damaged or loosened teeth
Orthodontic anchors	Bioglass-coated Al ₂ O ₃ , Bioglass coated vitallium	Providing posts for stress application required to change deformities

Although ceramic materials have many advantages, such as chemical inertness, high wear resistance and compressive stiffness, the further development of ceramics is limited due to the intrinsic brittleness. In recent decades there have been many attempts to improve the properties of ceramics, or trying to increase the positive interaction with tissues which led to the development of bioactive ceramics (217). Nanostructures and nanoreinforcements have been used to achieve intrinsic grain boundaries or extrinsic interfaces, which prohibit dislocation movement and create a long path for crack propagation (218-220). GPL have a Young's modulus of around 0.5 TPa under a tensile

load within the direction of the layer, which is higher than that of typical alumina ceramics at 300-380 GPa (221), while its thickness of only 2-8 nm (222) makes it a promising candidate as a bridging material for strengthening ceramic matrices.

5.1.3 Tissue Engineering Scaffold and 3D Graphene Foam

Scaffolds play a critical role in tissue engineering treatments. Developed from a subdivision research field of biomaterials, tissue engineering has constantly been growing in scale and gaining significance through successful medical cases which cannot otherwise be solved using traditional treatments (223). Today, tissue engineering is widely recognised as an indispensable area within biological sciences and a technology in itself. A common tissue engineering application consists of the sequential process of seeding host cells within an engineered porous scaffold, growing seeded cells into a designed tissue, and implantation into a host body to enable a repair or replacement. Common examples are dermal wound healing treatments, cartilage repairs and blood vessel replacements.

A scaffold acts as the supportive structure for the seeded cells and later the growing tissue, and a successful scaffold is usually constructed with a well-defined porous structure for nutrient intake and waste diffusion. It must be mechanically strong and sufficiently stable to not only hold the cells and tissue growing inside, but also facilitate the subsequent medical treatment. Besides, the scaffold must go through various biological tests to demonstrate that cells can adhere to and carry out their normal activities within the scaffold matrix. After being implanted into a host body, a scaffold should not cause a severe immune reaction, and finally, scaffolds are preferably gradually degraded into harmless residuals and then exit the human body via normal metabolic processes.

Due to its unique electrical conductivity, graphene was tested by neurobiologists as a potential material for a neural interface (224) and as a scaffold for neural stem cell differentiation (225, 226). However, its applications could be much wider than simply within neurobiology, and pioneers have been exploring the potential of using 3DGF as a tissue scaffold for other cells (227-229). Through measurements of mechanical properties and biological experiments, the potential of 3DGF to be used as a tissue engineering scaffold for MC3T3 cells is explored in this chapter.

5.2 Methodology

5.2.1 Fabrication Process for the Al₂O₃/GPL Composite

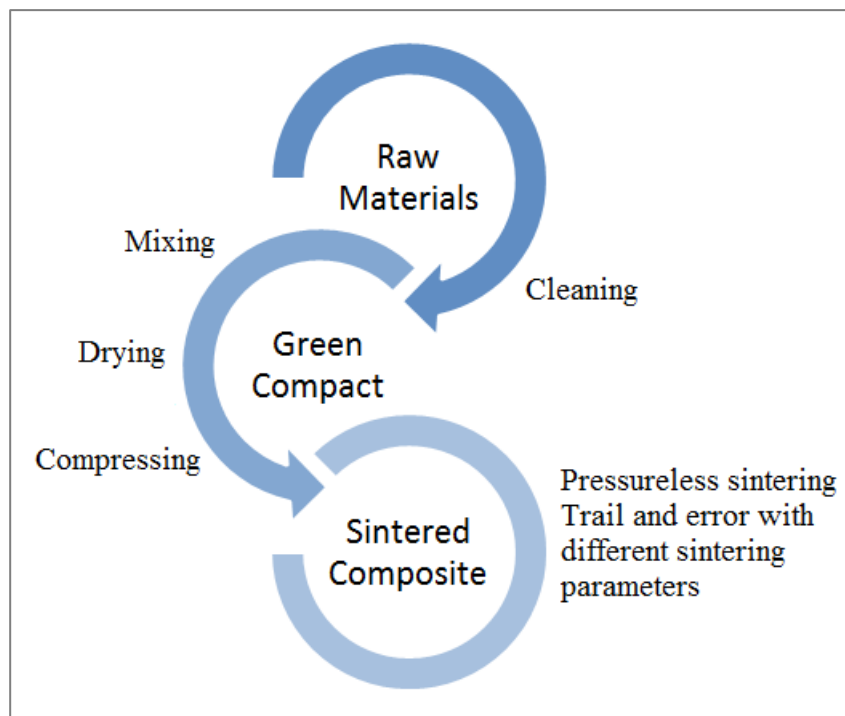


Figure 5.1: Schematic diagram of the manufacturing process for Al₂O₃/GPL

The fabrication process for Al₂O₃/GPL composites requires the preparation of raw materials, powder mixing, green compact formation, and last but not least, pressureless sintering. A schematic of the composite manufacturing process is shown in Figure 5.1. The ultimate purpose is to utilise GPL's superior in-plane mechanical strength by

uniformly blending GPL into a refined ceramic matrix. Previous studies [226, 227] have indicated that in order to form a proper composite GPL should be uniformly distributed inside a ceramic matrix, while retaining its unique two-dimensional structures during high-temperature processing. Another important requirement during the manufacturing process is to reach as high densification as possible.

Alumina powder was purchased from Inframat Advanced Materials, CT, the USA as α - Al_2O_3 powder (99.85%, 150 nm), and graphene platelets were purchased from Graphene Industries Ltd, Manchester, UK. Raw GPL was supplied in the form of stacks of graphene sheets, approximately 6-8 nm in thickness and 15-25 μm in diameter. Before the sintering process, raw GPLs were ultrasonically dispersed in N-methylpyrrolidone to prevent agglomeration. SEM images of the raw materials are presented in Figure 5.2. Next, Al_2O_3 powder was added to the suspension and mixed in a ball miller, as shown in Figure 5.3, and the mixture was then dried in an oven, and filled in a mould for cold isostatic pressing to form green compacts.

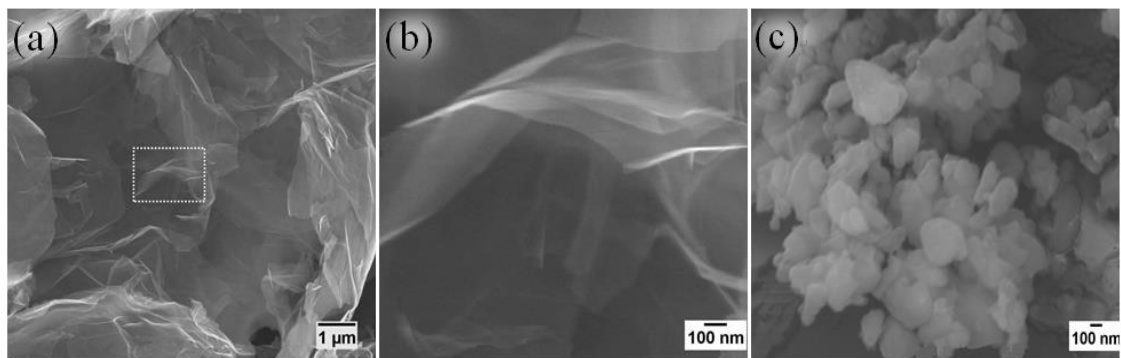


Figure 5.2: SEM images of raw materials before mixing

(a, b) graphene platelets; (c) Al_2O_3 nanopowder.

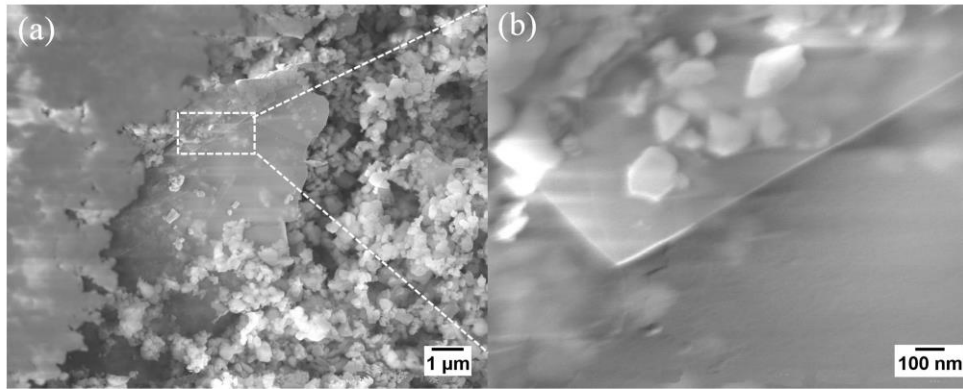


Figure 5.3: SEM images of the GPL/ Al_2O_3 powder mixture

Pressureless sintering is key to forming the desired composite, and nitrogen or forming gas was introduced into a tube furnace during sintering to protect the GPL within the powder compacts. Through a process of trial and error, sintering with various processing parameters was carried out using green compacts with 0.45% by volume GPL. The optimum processing parameters were chosen by assessing the microstructures and densities of the sintered composites. Via this optimisation process the sintering parameters, i.e. temperature, soaking time and flow rate, were determined.

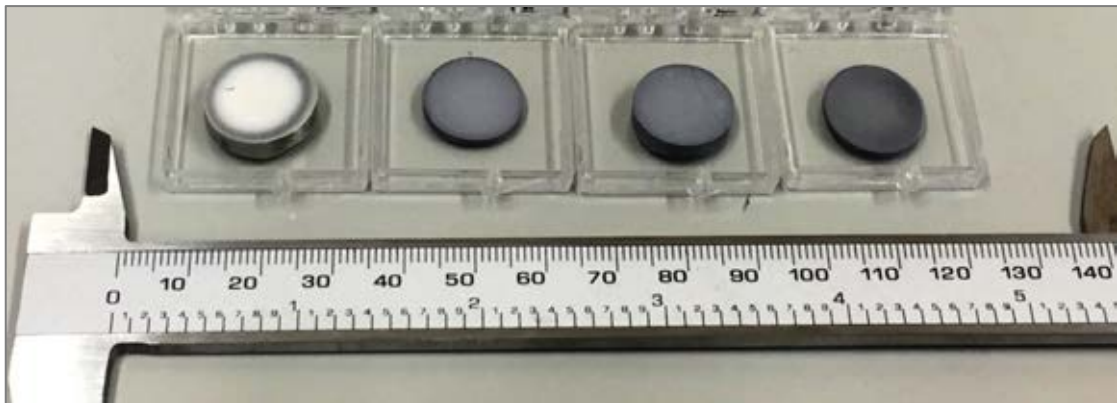


Figure 5.4: Sintered and polished Al_2O_3 /GPL samples
GPL concentration (from left to right): 0%, 0.75%, 1.3% and 1.48%

Three sets of composites with GPL volume concentrations of 0.75%, 1.3% and 1.48% were manufactured using the optimised parameters. Sintered samples are shown in Figure 5.4, and it can be seen that the sample surfaces appeared darker in colour with

increasing concentrations of GPLs from 0.75% to 1.48%. Further technical details concerning the fabrication process of this composite can be found in (177).

5.2.2 Fabrication of 3D Graphene Foam

3DGF was synthesised by Xi et al. (230) through growing 2D graphene layers on a 3D nickel matrix template. Through chemical vapour deposition (CVD) graphene was deposited onto the porous nickel foam template before it was cut along the edge to create an entrance for the etchant. The FeCl_3 solution was then applied to etch the nickel skeleton, and this process was accompanied by repeated washing with deionised water. Afterwards, the free-standing graphene foam was given a final clean with 10% HCl in order to eliminate any Fe contamination. Details of the process and the operating parameters can be found in the research of Xi et al. (230).

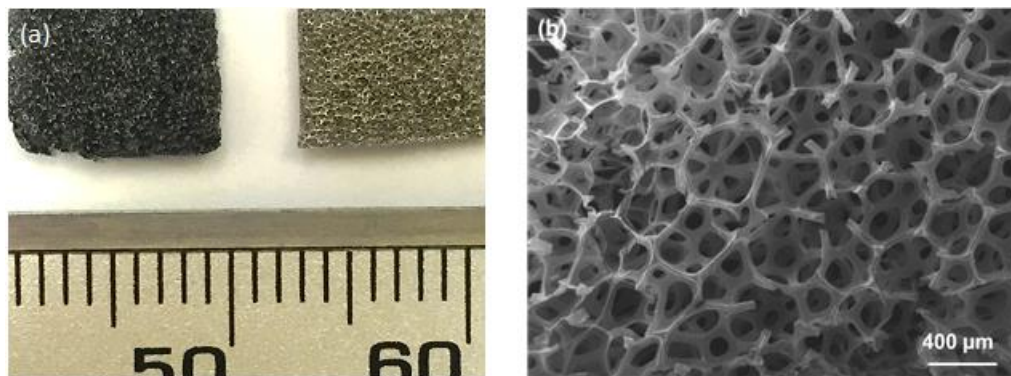


Figure 5.5: Images of 3DGF samples

(a) photo of 3DGF (left) and Ni template (right); (b) SEM image of 3DGF

As can be seen in Figure 5.5, the 3DGF used in the experiments was a free-standing porous matrix with a thickness of around 1.6 mm, perfectly masking the shape of the nickel template. The sample in this study had an average pore size of $450 \mu\text{m}$, which was controllable by adjusting the metal template. All the samples were cleaned by submerging them in deionised water and then in acetone for 15 minutes, followed by air drying in a clean room.

5.2.3 Measurement of the Mechanical Properties and Microstructure Characterisation of Al₂O₃/GPL

For the ceramic composites, bulk densities of the sintered samples were measured using the Archimedes method. The densities of raw Al₂O₃ and GPL were 3.97 and 2.1 g/cm³, respectively, and the relative density of the composites was calculated by dividing the absolute density of a sample by the theoretical density of the powder mixture. Flexural strength and fracture toughness of the sintered samples were obtained using an Instron 6025 test machine in the four-point bending test mode. The microstructure of the composite samples was observed by SEM.

5.2.4 AFM Indentation of 3DGF and Al₂O₃/GPL

Local mechanical properties and surface topography information for 3DGF and Al₂O₃/GPL were measured using the AFM nano-indentation method. A JPK NanoWizard®II with TopViewOptics™ was used as the measurement rig in these experiments, and a MikroMasch CSC17 NoAl parabolic probe was chosen as the indenter. Before the test, the cantilever (tip) was calibrated by indenting a benchmarked silicon plate using the method developed by Bowen et al. (153). The spring constant and sensitivity of the tip were obtained during the calibration procedure.

Cleaned 3DGF samples and Al₂O₃/GPL ceramic samples were carefully immobilised onto petri dishes and then loaded onto the AFM sample stage for measurement separately. Three different testing locations on the upper surface of the foam or ceramic surface were randomly chosen. Each test target had an area of 10 μm × 10 μm and was divided into 16 × 16 pixels; thus 256 pairs of force curves were acquired. During each loop of the indentation test two F-D curves were obtained, one

approaching and the other retracting, and key points (such as maximum force, contact point, etc.) were also captured.

To measure the elastic modulus, the Hertz contact model (155) for a sphere and a half-space was adopted to fit the F-D curves between the AFM tip and the 3DGF sample surface during an indentation process. For an elastic sphere with a radius R making contact with an elastic half-space, the relationship between displacement δ and the contact area a is described as:

$$a = \sqrt{R\delta} \quad (5.1)$$

The relationship between force F and the elastic modulus E^* and displacement are described as:

$$F = \frac{3}{4} E^* R^{1/2} \delta \quad (5.2)$$

$$E^* = \frac{1-\nu_1^2}{E_1} + \frac{1-\nu_2^2}{E_2} \quad (5.3)$$

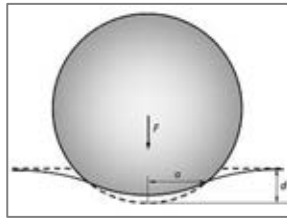


Figure 5.6: Schematic of the Hertz Contact Model

Approaching curves were fitted using the Hertz contact model to determine Young's modulus for each testing point. Other mechanical properties obtained during the measurements included maximum adhesion, maximum attraction and surface roughness. Standard deviations were taken as the error for each averaged parameter.

5.2.5 Cell Culture

In addition to mechanical tests, the application of any newly discovered biomaterial requires a series of complex biological assessments depending on the specific application scenario, and including but not restricted to cell adhesion, protein adsorption, thrombus formation, immune system reactions, inflammatory reactions, etc. In this study, the focus is on the essential assessment of how different mammalian cells react directly with $\text{Al}_2\text{O}_3/\text{GPL}$ and 3DGF.

Two types of cells were used in these experiments. MC3T3 cells (from passage numbers 10 to 20) were thawed from liquid nitrogen stocks supplied by TRAILab, University of Birmingham. The thawed cells were cultured in supplemented DMEM and incubated at 37°C in a humidified incubator with 5% CO_2 . The cell culture medium consisted of the base DMEM (Sigma D6546) supplemented with 10% FBS, 2% L-glutamine (200mM, Sigma), 1% penicillin-streptomycin (10,000 units penicillin and 10 mg streptomycin per mL, Sigma) and 2.4% HEPES buffer (1M, Sigma). BMSCs were also used in the cell adhesion tests, and primary BMSCs were extracted from rat tibias and fibulas, then cultured in alpha-MEM (supplemented with the same concentrations as DMEM) and incubated at 37°C in a humidified incubator with 5% CO_2 .

For cell culture on $\text{Al}_2\text{O}_3/\text{GPL}$ samples, sintered ceramic composite samples with different concentrations of GPL were ground and polished to $0.5\mu\text{m}$ using SiC papers and then a diamond suspension. All the samples were ultrasonically cleaned in acetone and then deionised water for 15 minutes. A 12-well cell culture plate was modified with PDMS (SYLGARD 186) cured on the base of each well as an inert layer. Ceramic composite samples were then placed on top of the PDMS layer, and samples, as well as the substrate, were then immersed in 70% ethanol for 40 minutes, before being dried in

a laminar airflow hood. After reaching 80% confluence, MC3T3 cells were trypsinised, subjected to centrifugation and re-suspended, before being seeded onto the prepared ceramic samples at a density of 5×10^4 cells/cm², and cultured in an incubator. Two types of medium were used in the experiments for the ceramic samples; DMEM supplemented with 10% FBS was used to culture MC3T3 cells and BMSC for standard biomaterial reaction tests, while serum-free DMEM was used for the culture of MC3T3 cells to assess the initial cell attachment on ceramics.

The cell culture setup for 3DGF samples was similar to that used for Al₂O₃/GPL. 3DGF and the Ni-foam template (as a control) were ultrasonically cleaned in acetone and then deionised water for 15 minutes before being air dried. Samples were then placed on top of PDMS modified cell culture plates and immersed in 70% ethanol for 40 minutes, and dried in a laminar airflow hood. Only serum-free DMEM was used in the MC3T3 cell seeding experiments.

5.2.6 *In vitro* MTT Assay

The MTT assay was chosen as the methodology to quantitatively assess attached viable cells on Al₂O₃/GPL composites and 3DGF matrix separately. For Al₂O₃/GPL composites, MTT assays were carried out for the MC3T3 cultured cells after 3 hours, 1 day and 3 days separately. Pure Al₂O₃ ceramic and PDMS substrate were used as controls.

Another set of MTT assays were performed one day after cell seeding using non-supplemented DMEM, in order to assess the initial cell attachment on Al₂O₃/GPL and 3DGF without being affected by serum proteins.

5.2.7 Fluorescence Microscopy

Fluorescence microscopy was utilised to obtain qualitative results on how cells reacted to the graphene composite materials. Two microscope systems were applied in these experiments, as can be seen in Figure 5.7. Calcein AM and propidium iodide (PI) were used to stain live/dead cells in the fluorescence assay. Live cells are able to convert the non-fluorescent calcein AM dye to fluorescent calcein dye through intracellular esterase activity, while PI is membrane impermeable and does not enter living cells with intact cell membranes. When PI can gain access into a cell it intercalates with nucleic acids and the DNA is stained; therefore, PI is used to identify dead cells. Calcein and PI were used together to visualise both live and dead cells.

The fluorescence live/dead assay on Al₂O₃/GPL composites was performed as follows. After 80% confluence, pre-cultured BMSC were treated with TrypLE™ Express (Life Technology) in order to detach them from the culture flask. Cells were seeded onto the sintered samples, and tissue culture plastic and PDMS substrates were utilised as positive and negative controls, respectively. Cells were cultured in an incubator at 37°C with 5% CO₂, supplemented with alpha-MEM. After 3 days the cell culture medium was removed and replaced with 37°C PBS. Next, calcein AM and PI (1 µl/ml medium) were added to each cell culture well, and the cells were returned to the incubator for a further 30 minutes. The samples were then observed using a Carl Zeiss™ Axiolab Fluorescence microscope.



Figure 5.7: Fluorescence microscopes used in this study

An Olympus ix81 confocal microscope system integrated with FluoView™ FV1000 (left) and a Carl Zeiss™ Axiolab Fluorescence microscope (right)

For the live/dead assay on 3DGF, graphene foam samples and the nickel template foam (for comparison) were cut into cuboids of 10 mm × 5 mm × 1.5 mm. After cleaning, samples were immobilised on top of PDMS in a 12-well cell culture plate and immersed in 70% ethanol. MC3T3 cells were then seeded onto 3DGF and nickel foam at a density of 1×10^5 cells per well and the seeded samples were observed by fluorescence microscopy after 1 day and 3 days separately. Cells were stained with calcein AM and PI using the same protocol as described above. Due to the porous nature of the matrix, multiple focus layers of the samples were observed using an Olympus ix81 fluorescence confocal microscope.

5.3 Results and Discussion

5.3.1 Enhanced Mechanical Properties and *In vitro* Experiments of Al₂O₃/GPL Composites

The density test on sintered GPL/Al₂O₃ composites showed that the relative density of the composites decreased with an increasing concentration of GPL. Pure Al₂O₃ samples had the highest density of 99.2%, while the relative density of GPL/Al₂O₃ composites

decreased from 98.1% to 95.6% when increasing the GPL concentration from 0.75% to 1.48% vol. This suggests that the addition of GPLs hindered the densification during pressureless sintering, and a higher sintering temperature or longer sintering time may be needed in order to obtain fully densified samples with a high concentration of GPLs added.

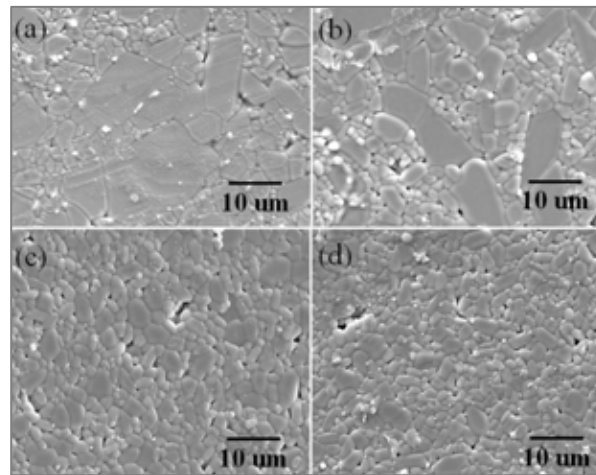


Figure 5.8: SEM images of sintered and polished ceramic surfaces

(a) Al_2O_3 ; (b) 0.75 % GPL/ Al_2O_3 composite; (c) 1.3 % GPL/ Al_2O_3 composite; (d) 1.48 % GPL/ Al_2O_3 composite.

Figure 5.8 shows the SEM images of the polished surfaces of the sintered samples with different concentrations of GPL, and it can be seen that with more GPL added into the ceramic matrix, smaller grain size was obtained. Figure 5.9 shows the grain sizes of the sintered samples measured using software (UTSHCSA, USA). The averaged grain size decreased from 4.31 to 2.87 μm when increasing the concentration of GPLs from 0 to 1.48% vol. The error bars are smaller for the composites with more GPLs, which was in agreement with the refined microstructures shown in Figure 5.8. With a higher concentration of GPL, the composite formed a more refined matrix microstructure with smaller ceramic grains and uniformly distributed GPL. The refined microstructure was believed to have a positive impact on the bulk mechanical strength of the composites.

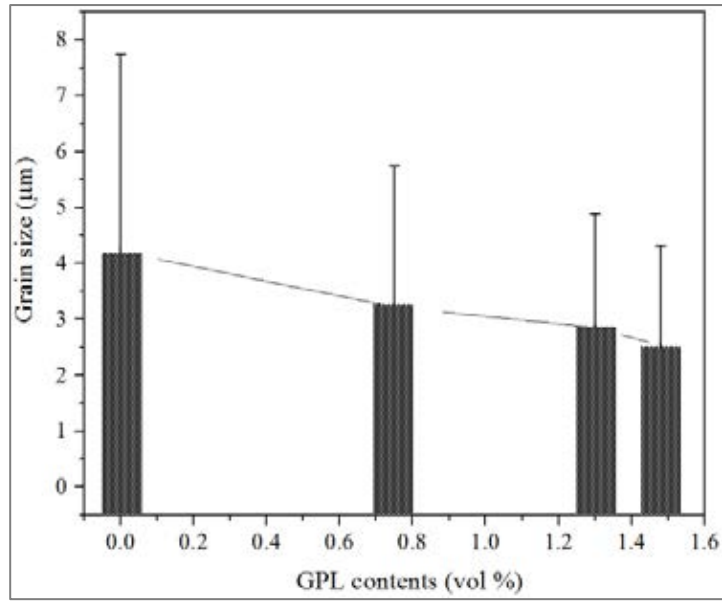
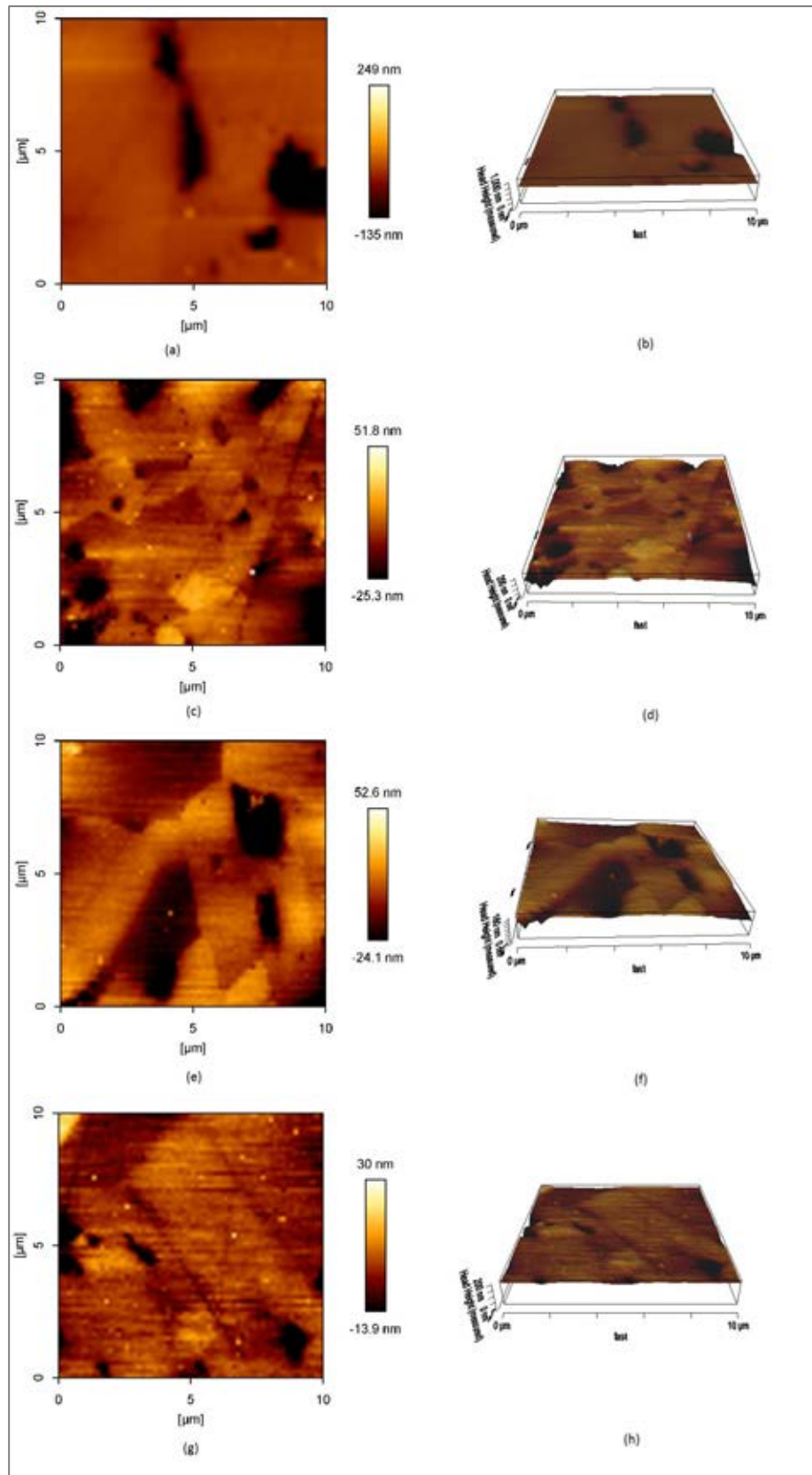


Figure 5.9: Grain sizes of GPL/ Al_2O_3 composites matrices

Grain sizes of sintered ceramic samples were measured by software and presented in the figure. (Mean \pm SD, N = 200)

AFM indentation tests were performed on sintered samples, and as can be seen in Figure 5.10, the trend in grain size refinement agreed with the results obtained from the SEM images. Large gaps and holes of 2-5 μm were present on the surface of the pure Al_2O_3 samples. When GPL was added to the composite, the surface microstructure immediately improved (Figure 5.10c-f). However, several small gaps and hollow structures could still be observed, which were possibly to be the positions where GPL was exposed. The AFM topography confirmed that the Al_2O_3 /GPL composites had a better grain formation when more GPL was added.



**Figure 5.10: Surface topography of $\text{Al}_2\text{O}_3/\text{GPL}$ measured by AFM indentation
2D and 3D views**

(a-b) Al_2O_3 ; (c-d) 0.75 % GPL/ Al_2O_3 composite; (e-f) 1.3 % GPL/ Al_2O_3 composite; (g-h) 1.48 % GPL/ Al_2O_3 composite.

Although the GPLs in the ceramic matrix were designed to be evenly distributed, some platelets were clustered, and as can be seen in Figure 5.11d-e, there was a site where GPLs were gathered in irregular patterns and exposed on the sample surface, where both the flat body and sharp edges of GPLs could be seen. Due to the limitations of the methodology, AFM testing on the exposure site could not show the fine details revealed by SEM. The exposure site was apparent as irregular holes with non-uniform local mechanical properties during indentation, and an example is shown in Figure 5.11a-c. The irregular assembly and exposure of GPLs in ceramic matrices was considered a defect of the material, and further enhancement is needed in order to reduce it.

Bulk material flexural strength and fracture toughness of Al₂O₃/GPL composites were tested and compared to pure alumina ceramic. Table 5.2 shows that the flexural strength and fracture toughness of Al₂O₃ were significantly improved by adding just a small amount of GPL, and the maximum property improvement occurred following the addition of 0.75% GPL; however, a further increase in GPL led to a decrease in these properties. Mechanical strength improvement may have been achieved due to the solid anchorage between GPL and the ceramic matrix established during the long sintering process. Also, GPL could act as either bridging particles when a crack tried to propagate, or by toughening barriers to deflect crack propagation.

Table 5.2: Flexural strength and fracture toughness of Al₂O₃/GPL composites with different compositions of GPL

GPL vol. percentage	0%	0.75%	1.3%	1.48%
Flexural Strength (MPa)	340	548	503	460
Fracture Toughness (MPa)m ^{1/2}	2.80	4.33	4.03	3.61

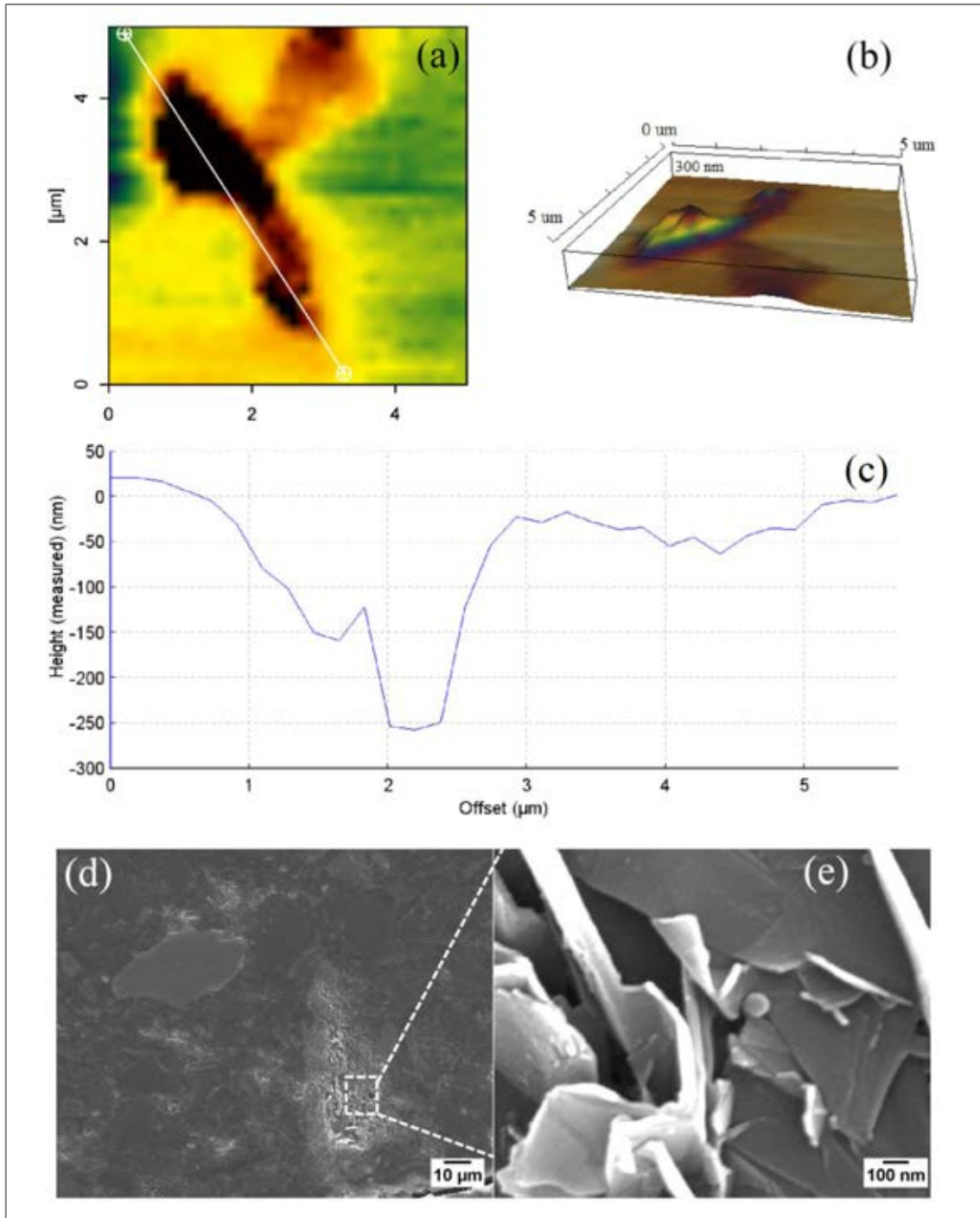


Figure 5.11: GPL exposure on $\text{Al}_2\text{O}_3/\text{GPL}$ composites surfaces

(a) $5\ \mu\text{m} \times 5\ \mu\text{m}$ area AFM topography of 1.48 % GPL/ Al_2O_3 composite surface showing a possible GPL exposure site; (b) inverse 3D structure showing the irregular hole structure; (c) cross-sectional depth along the marker line; (d-e) SEM images of a GPL exposure site

Surface adhesion force and surface roughness were acquired during the AFM indentation test, and are presented in Figure 5.12. Only one set of samples were tested with five randomly selected positions on each sample surface. Surface adhesion forces

are presented as the mean and standard deviation, while surface roughness values are for the whole sample surface. As can be seen, adding GPLs reduced the surface roughness to around a third the level of pure Al_2O_3 ; however, the 1.3% Al_2O_3 /GPL sample had an abnormal surface roughness increase from 69.0 nm to 103.8 nm compared to the control group, which may suggest that the 1.3% Al_2O_3 /GPL sample had a large portion of GPL exposure sites present on the surface. The average surface adhesion force of ceramic composites decreased from 27.69 nN (GPL 0.75%) to 24.31 nN (GPL 1.3%), and 16.39 nN (GPL 1.48%). Surface adhesion forces were used later in section 5.3.3 as part of the test for the proposed methodology.

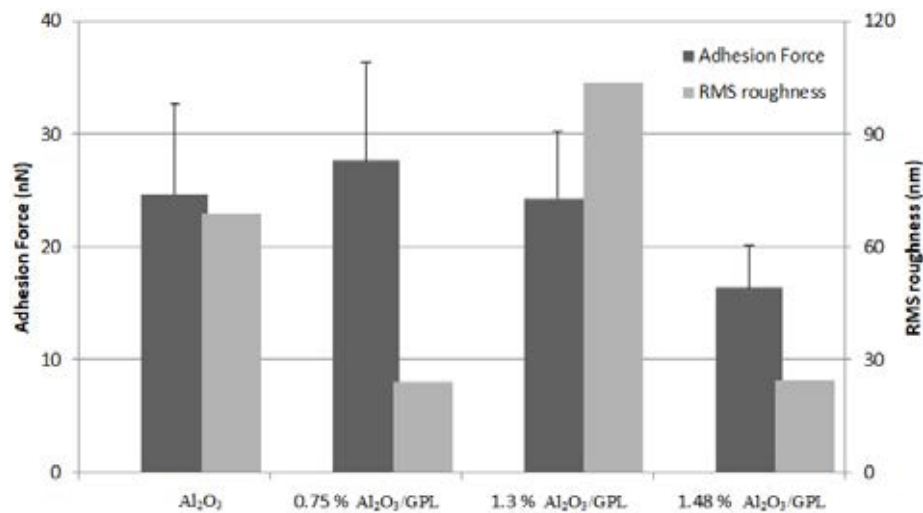


Figure 5.12: Surface mechanical properties of Al_2O_3 /GPL composites with different GPL concentrations

Measurements were taken by AFM in the contact mode. One sample was prepared for each group, and three random test positions were chosen on each sample. Each test position was divided by a 16×16 matrix, i.e. 256 measurements were taken at each test position. (Mean \pm SD, N = 768)

Experiments were designed to test the potential for use in biological applications. Three parallel groups of cell seeding experiments were carried out on Al_2O_3 /GPL composites. MC3T3 and BMSC were cultured on ceramic samples in a standard *in vitro* cell attachment test in which serum-supplemented medium was applied; then an MTT assay was performed on MC3T3 groups after 3 hours, 1 day and 3 days separately to

quantitatively assess cell attachment on ceramic composites; each assay contained three repeats (N=3). A single (N=1) live/dead assay was carried out on the BMSC samples using fluorescence microscopy. Finally, MC3T3 cells were cultured on ceramic composites without serum supplementation (N=3), and an MTT assay performed afterwards to assess the initial cell attachment on ceramic composites, which was then later used to validate the correlation with surface nanoforces.

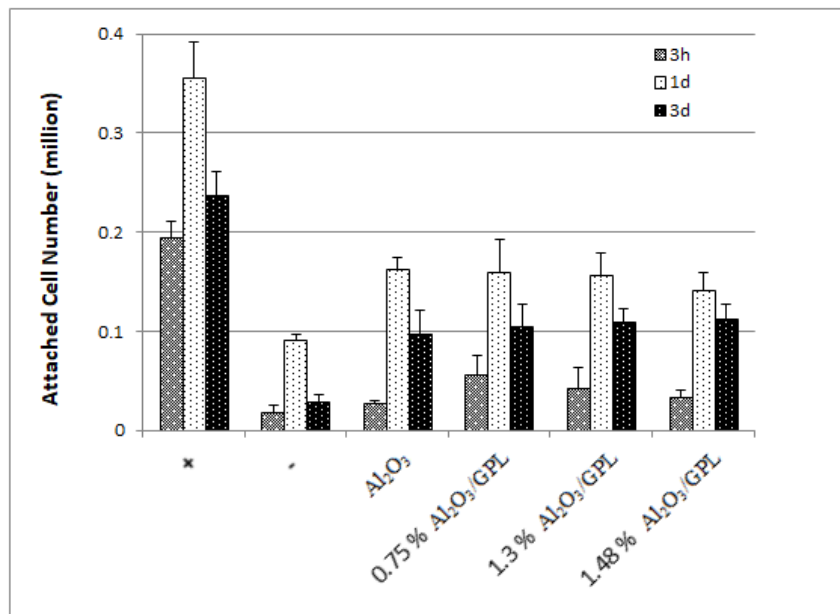


Figure 5.13: MTT results for different ceramics composites using serum-supplemented culture medium

The attachment of MC3T3 cells on ceramic/GPL composite samples was investigated after 3 hours, 1 day and 3 days of incubation. (Mean \pm SD, N = 3) The positive control is a cell culture disk; the negative control is PDMS.

The attachment of MC3T3 cells to GPL composite samples was first investigated via an MTT assay after 3 hours, 1 day and 3 days incubation and the results are shown in Figure 5.13. As expected, the least and most viable cells were found in the negative and positive control groups, respectively, for all the tested conditions. After 3 hours incubation, the viable cell number for Al₂O₃/GPL composites was higher than that for monolithic Al₂O₃, which was similar to the negative control. This meant that the addition of GPL into the ceramic matrix aided cells during the initial attachment stage,

which was in agreement with the reported work on graphene reinforced hydroxyapatite composites (228). After 1 day of incubation, cells were attached to the substrate and subject to exponential growth. In this set of results, the $\text{Al}_2\text{O}_3/\text{GPL}$ samples exhibited slightly lower cell viability compared to pure Al_2O_3 , and the cell number was insignificantly decreased between the 0.75% and 1.48% samples. This might have been caused by the sharp edges of the GPL clusters exposed on the surfaces of the ceramic composites, which were detrimental to cell proliferation, and so caused a delay in cell proliferation on these surfaces. After 3 days of incubation decreased viable cell numbers were observed in all the sample groups compared to the results for day one, which could be due to the apoptosis of cells. The difference between pure alumina and the $\text{Al}_2\text{O}_3/\text{GPL}$ samples was negligible. One possible explanation is that every sample had reached confluence and the surface areas were the same for pure alumina and GPL supplemented groups. Further experiments are suggested in order to understand better whether GPLs affect cell apoptosis.

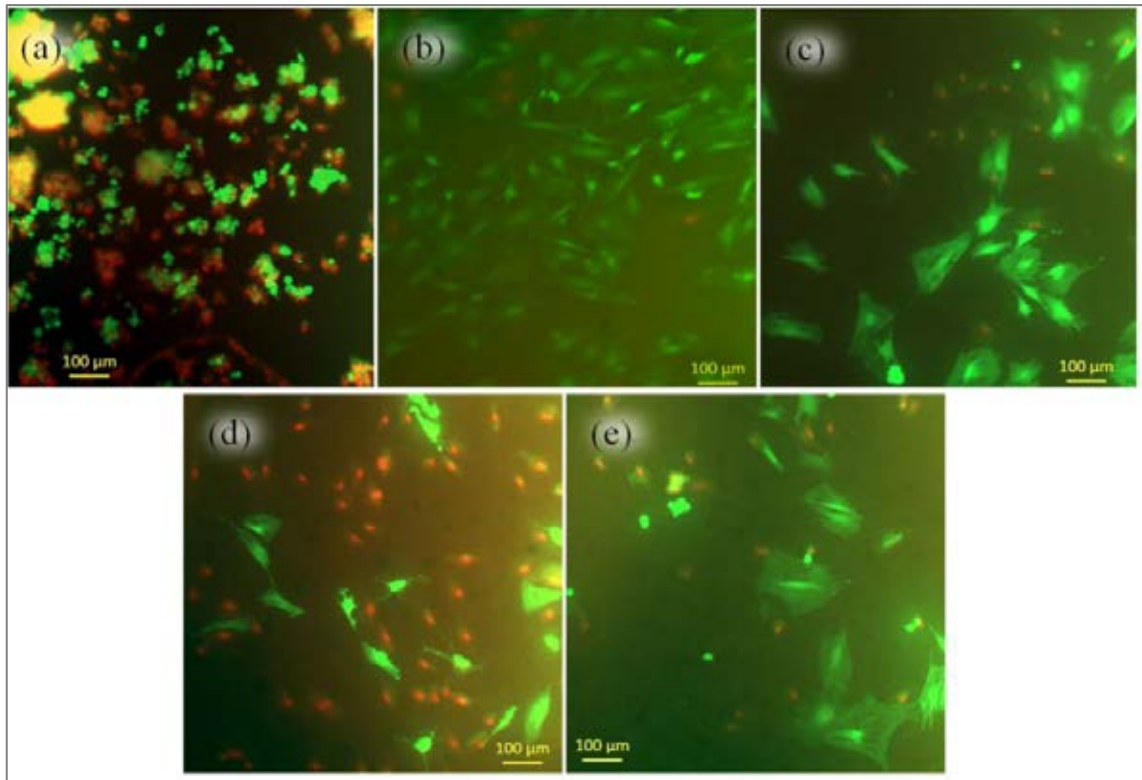


Figure 5.14: Fluorescence microscopy images of BMSC present on the sample surfaces (a) PDMS; (b) Al₂O₃; (c) 0.75 % Al₂O₃/GPL composite; (d) 1.3 % Al₂O₃/GPL composite; (e) 1.48 % Al₂O₃/GPL composite.

BMSC was chosen for the live/dead fluorescence assay in order to observe the effect of Al₂O₃/GPL on cell growth and differentiation. Live cells were stained green, and dead cell nuclei red, and sample images can be seen in Figure 5.14. It can be seen from Figure 5.14 that cells in the PDMS negative control group showed no expansion and both live and dead cells were gathered in clusters floating in the medium; it could be that some live cells were loosely attached to the PDMS surface but were shaken off during the assay. Cells with varied morphologies were present on the pure alumina and composites, which could be caused by cell differentiation. As suggested in Figure 5.14c-e, cells on the surface of the Al₂O₃/GPL composites were larger with better spreading and elongation. Phenotyping of the cells in the different samples is beyond the scope of this research; however, it could be an interesting direction to explore in the future. The results suggest that other factors also play an important role in the

interaction between BMSCs and ceramics, as previous studies have noted that surface topography (231), porosity, surface chemistry, and the accumulation of charge (223) can affect cell growth and differentiation.

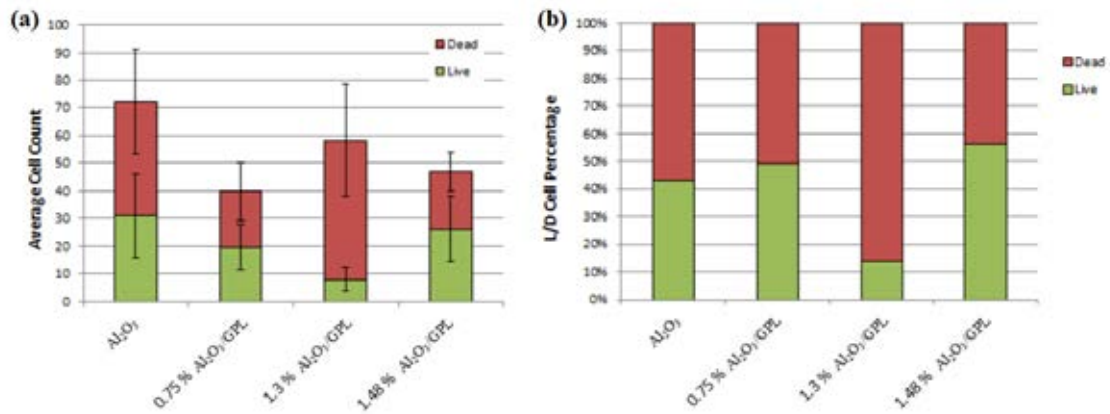


Figure 5.15: Live/dead cell counts of BMSC on ceramic composites

Cells stained with fluorescent dyes were counted after three days of cell culture. Five cell counting positions of $950 \mu\text{m} \times 950 \mu\text{m}$ were randomly selected for each sample. (a) live/dead cell count (Mean \pm SD, N = 5) and (b) live/dead cell percentage.

Aside from the morphological observations, a cell count was conducted for all the fluorescent images of Al₂O₃/GPL sample, and the results are shown in Figure 5.15 as the live/dead cell number count and live/dead percentage. The total number of attached cells was reduced in the Al₂O₃/GPL samples, indicating a negative effect of GPL on the proliferation of BMSCs. The 1.3% Al₂O₃/GPL samples exhibited a particularly low live/dead ratio, which again was in agreement with the presence of exposed GPL sites as shown in Figure 5.12.

Finally, to further test the correlation between surface nanoforces and cell attachment proposed in Chapter 4, the initial cell attachment of MC3T3 on Al₂O₃/GPL composites was also assessed via an MTT assay one day after initial cell seeding in non-serum containing culture medium. After washing off the non-attached cells, the viable cell number for each sample was determined (Figure 5.16), and the results show that GPL/alumina ceramics exhibit more favourable conditions for the initial attachment of

osteoblast precursor cells, which is in agreement with the 3 hour group results shown in Figure 5.13. This suggests that the effect of adding GPL on the initial cell attachment could be achieved in as soon as three hours following seeding. The 1.3% GPL/alumina samples showed the lowest cell attachment, which may be due to the high proportion of exposed GPL sites, as suggested in Figure 5.12. The initial cell attachment result for the ceramic composites is used later in section 5.3.3, as part of the initial proof of concept for the empirical methodology.

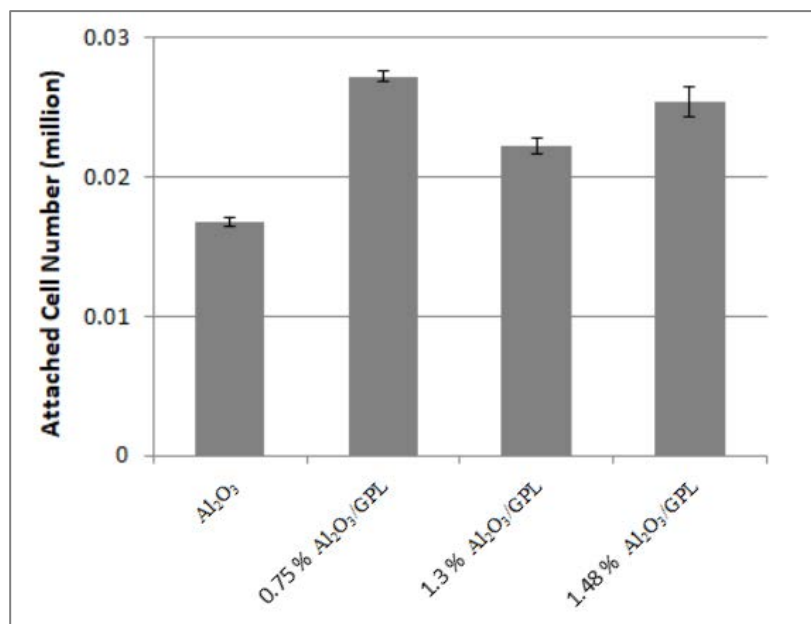


Figure 5.16: Viable MC3T3 cell attachment on Al₂O₃/GPL composites using non-serum culture medium

Cell attachment of MC3T3 cells on ceramic/GPL composite samples was investigated after 1 day incubation. Attached cell numbers were calculated via an MTT assay. (Mean \pm SD, N = 3)

5.3.2 Mechanical Properties and *In vitro* Biocompatibility of 3DGF

In order to test the mechanical properties, AFM indentation experiments were performed on 3DGF. Seven testing positions were randomly selected on the scaffold frame of the foam, and each testing position had an area of 10 μm \times 10 μm . Positions 1-5 were selected on one 3DGF sample, while positions 6-7 were on another. Table 5.3 shows the measured mechanical properties of 3DGF; attraction force and adhesion

force are the averaged maximum forces from the approaching curves and retracting curves, respectively. Surface roughness was calculated by the software using surface topography data.

Table 5.3: Mechanical properties of 3DGF by AFM indentation

Position	1	2	3	4	5	6	7
Attraction (nN)	3.816	4.608	4.68	4.428	5.652	7.884	7.884
	±0.9	±1.152	±1.152	±1.368	±2.052	±1.944	±0.648
Adhesion (nN)	15.012	41.904	40.68	30.564	25.092	81.108	21.528
	±7.092	±34.416	±30.924	±27.432	±19.404	±44.748	±0.684
Elastic Modulus (MPa)	11.1	12.4	12.6	12.31	12.26	20.23	6.15
	±1.04	±0.9	±0.91	±1.08	±1.22	±7.2	±1.13
RMS Roughness (nm)	26.74	54.47	189.7	157.1	219.7	n/a	n/a

In Table 5.3 it should be noted that the adhesion force and attraction force at position 1 were smaller than at the other positions. Surface roughness and deviation of force values were also low compared to other positions, which suggest a relatively uniform surface. Similar results were also found for position 7, while the adhesion force at positions 2 – 6 demonstrated high variance, which was believed to be caused by the rim/groove structure formed by the overlaid graphene layers, as can be seen in Figure 5.17. These rim structures were found to be present in test positions 2, 3, 4 and 5, and were believed to be formed during the CVD process (225). When the AFM tip was pulled away near the rim/groove, then multiple layers of atoms will have interacted with the tip. Thus a larger VDW interaction existed around these areas, which led to a larger adhesion force. From the results shown in Figure 5.17, it can be seen that the adhesion force distribution (Figure 5.17 b) was aligned with the rim/groove structure (Figure 5.17a).

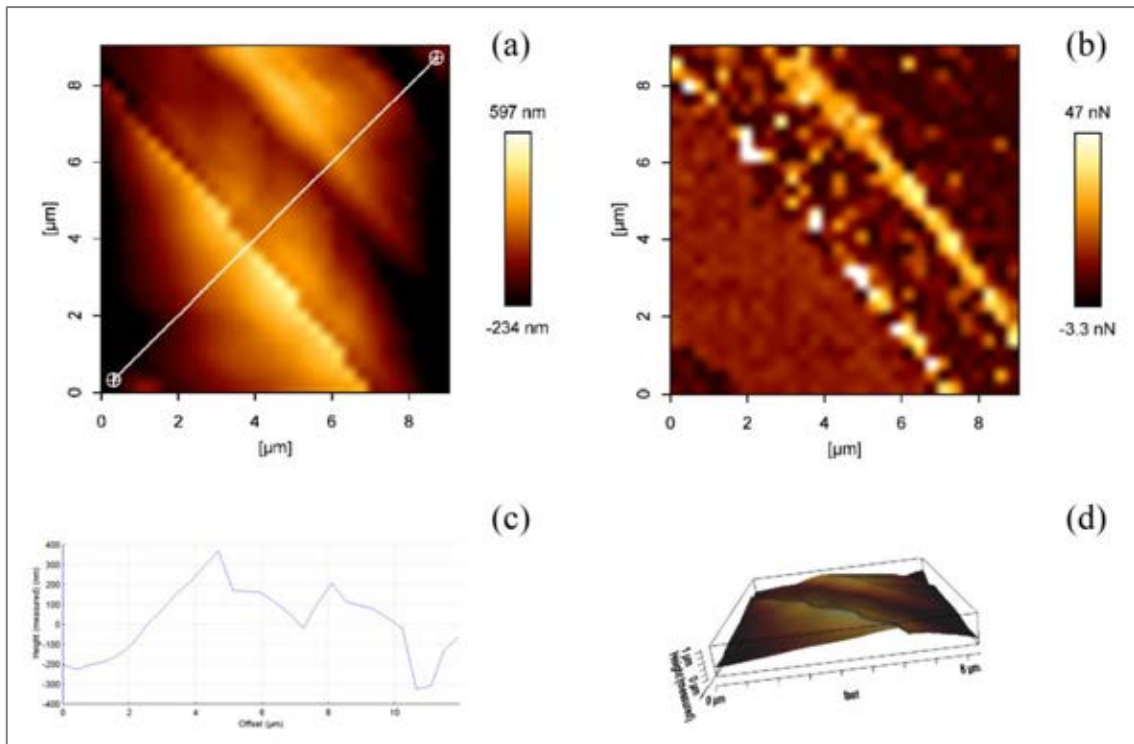


Figure 5.17: AFM surface topographical measurement of a 3DGF rim structure
 (a) Top view of the rim structure; (b) Surface adhesion force map; (c) Cross-section height; (d) 3D view of the rim structure.

Young's modulus from each testing point was obtained by fitting the force curves to the Hertz model, and the results are compared to common biological materials in Figure 5.18 (232). Hertz fitting of the 3DGF surface force curves showed that the elastic modulus of the 3DGF matrix mostly lies in the range of 10 MPa to 20 MPa. In Figure 5.18 it can be seen that the elastic modulus of 3DGF is similar to those of gelatin and cartilage, which have Young's modulus of 0.01 - 10 MPa and 1 - 10 MPa, respectively. As a result, cells grown on top of the 3DGF surface should sense a similar elastic modulus from the substrate as a gelatin matrix or cartilage tissue. It is well known that anchorage-dependent cells are able to sense and interact with their external environment through mechanical channels and transducers, such as ion channels, primary cilia and integrin. Through these channels, cells are constantly regulated by mechanical signals from attachment until apoptosis. It has been reported that fibroblasts (10), neurons (233), myoblasts (234) and endothelial cells (235) demonstrate sensitive reactions against

substrate stiffness changes, and in this aspect, 3DGF can provide similar stiffness to gelatin or cartilage to the cells growing on it.

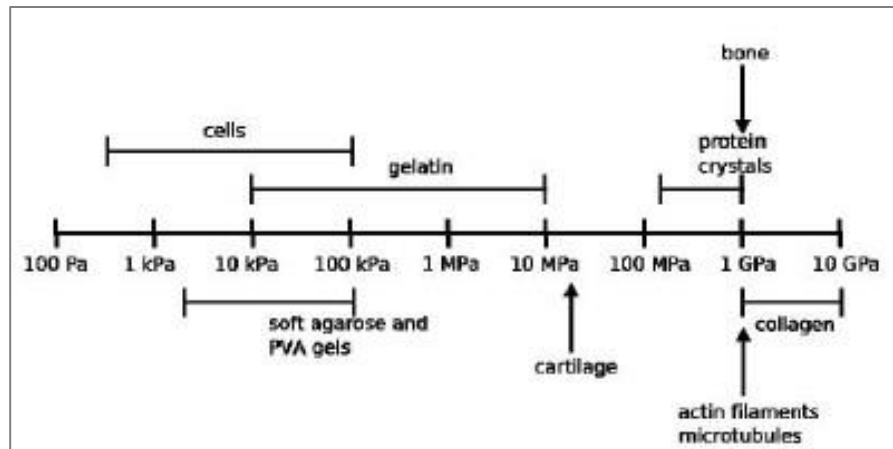


Figure 5.18: Overview of Young's modulus for common biological materials (232)

To test the potential of 3DGF being used in biological applications, MC3T3 cells were chosen to carry out *in vitro* direct seeding experiments. Two sets of experiments were conducted with cells cultured in serum-free medium for one day and three days, separately. Confocal fluorescence microscopy was utilised to explore the cell attachment and spreading among multiple focus layers within the foams, in which living cells were stained green and dead ones red.

One group of samples were observed one day after seeding in order to study initial cell attachment, and by moving the focus layer, the foams were thoroughly observed. The results show that most of the cells had not penetrated into the foam after one day of serum-free culture, although as can be seen in Figure 5.19 (left panel), some cells had attached to the 3DGF circumference layer surface. In contrast, cells on the nickel-foam appeared only to be loosely attached in a spherical shape in a cluster or to be dead and floating around.

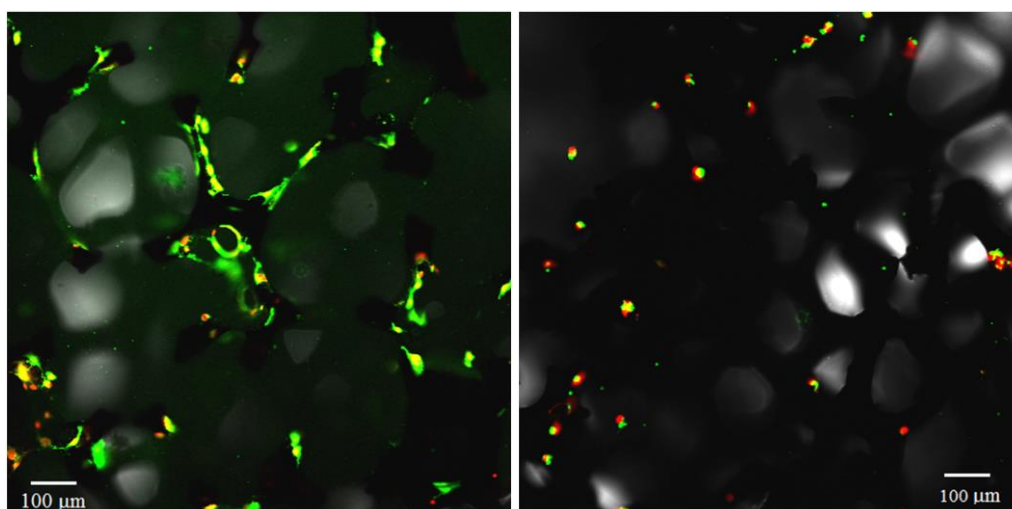


Figure 5.19: Fluorescence microscopy images of MC3T3 cells attached to the outer layer of 3DGF (left) and the nickel template (right) one day after cell seeding in non-serum cell culture medium

Cells were observed after three days of culturing, and increased cell penetration was found via fluorescence microscopy. Cells had attached and spread from the top to the bottom of the matrix in both the 3DGF and nickel foam samples. Most of the cells had attached to the edges or corners around small holes and had then elongated along the frame of the matrix. However, there were cells anchored on both sides of a pore which had formed cellular bridges, and an example is shown in Figure 5.20 (white arrow). A similar structure has been observed by other researchers when epithelial cells experience external tension during cell growth and migration (236). These bridges were only found in 3DGF sample and not the nickel sample, but the reason for this is not understood, although the difference in stiffness or surface adhesion between the two scaffolds might play a role.

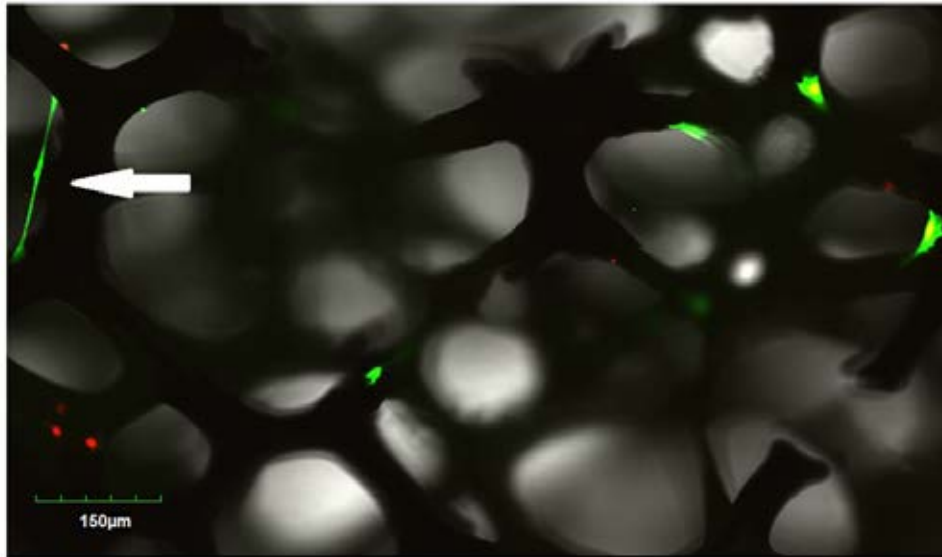


Figure 5.20: Fluorescence microscopy images of MC3T3 cells growing inside the 3DGF matrix

A cell bridge is present in the top left corner indicated by the white arrow.

After the morphology observations, a cell count was performed using fluorescence microscopy for both the 3DGF and nickel samples. Three cuboid spaces of $1130 \mu\text{m} \times 750 \mu\text{m} \times 490 \mu\text{m}$ were randomly selected in the middle of the foam matrix, and live and dead cell numbers were recorded by hand while the cuboid spaces were scanned by confocal microscope. As shown in Figure 5.21, 3DGF was found to have more cells attached, but nickel foam had a better live/dead ratio.

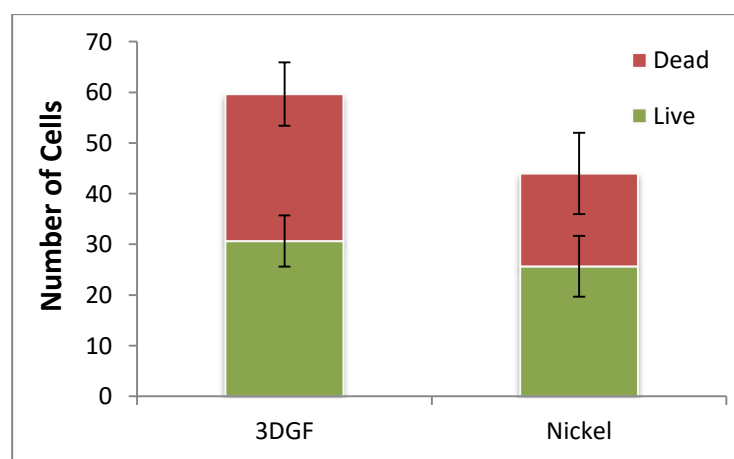


Figure 5.21: Live/dead cell count inside 3DGF and Nickel foam matrix

Three cuboid spaces of $1130 \mu\text{m} \times 750 \mu\text{m} \times 490 \mu\text{m}$ were randomly selected in the middle of the foam matrix for each sample. Fluorescently stained cells were counted using fluorescence microscopy. (Mean \pm SD, N = 3)

Generally, 3DGF performed better than the nickel template in MC3T3 seeding experiments, as there was more cell attachment in both the initial cell attachment experiment (one-day group, only on circumference layer) and also the long-term experiment (three-day group, cells had penetrated through the foam). From Figure 5.20 and Figure 5.21 it can be seen that it took MC3T3 cells more than one day to penetrate through the entire scaffold matrix, and the overall viable cell number after three days of culture was roughly 10% of the seeding cell number (calculated as cell count number \times total volume of scaffold/cell count volume/seeding cell number). This could be caused by an insufficient seeding density or a limitation of the medium flow due to pore size. It may also suggest that serum is essential for MC3T3 cells to penetrate speedily through the 3DGF matrix.

5.3.3 Empirical Methodology for Early Assessment of Initial Cell Attachment on New Materials

From the results of Chapter 4, the positive correlation between surface nanoforces and cell attachment was examined and indicated that there was some influence. Apart from providing a better understanding of cell attachment process, a practical application can be extracted from this correlation. AFM surface measurements generally outperform biological tests regarding time-efficiency and cost-efficiency; thus by measuring the surface nanoforces on the target, initial cell attachment can be quickly estimated according to the conclusions of Chapter 4.

To test this methodology, surface nanoforces were measured for both GPL/Al₂O₃ composites and 3DGF as the target new materials, and these were then compared to the *in vitro* cell attachment results for the new materials. The idea was to examine whether the surface nanoforces can reasonably match the experimental cell attachment results for the different groups of samples. If the results were positive, then the methodology

could be used for a preliminary estimation of cell attachment to new materials, compared to a benchmark.

For GPL/ Al_2O_3 composites the initial cell attachment after the one day of culture in medium with no serum is presented in Figure 5.22. The surface adhesion forces of GPL/ Al_2O_3 composites and the initial cell attachment data extracted from the *in vitro* MTT assay were compared.

It can be seen from this figure that the relative values for the surface forces from different GPL/ Al_2O_3 composites roughly corresponds to the changes in the initial cell attachment data, except for the 1.48% GPL/ Al_2O_3 composite samples, which had a higher cell attachment than the 1.3% group, while the adhesion force was lower.

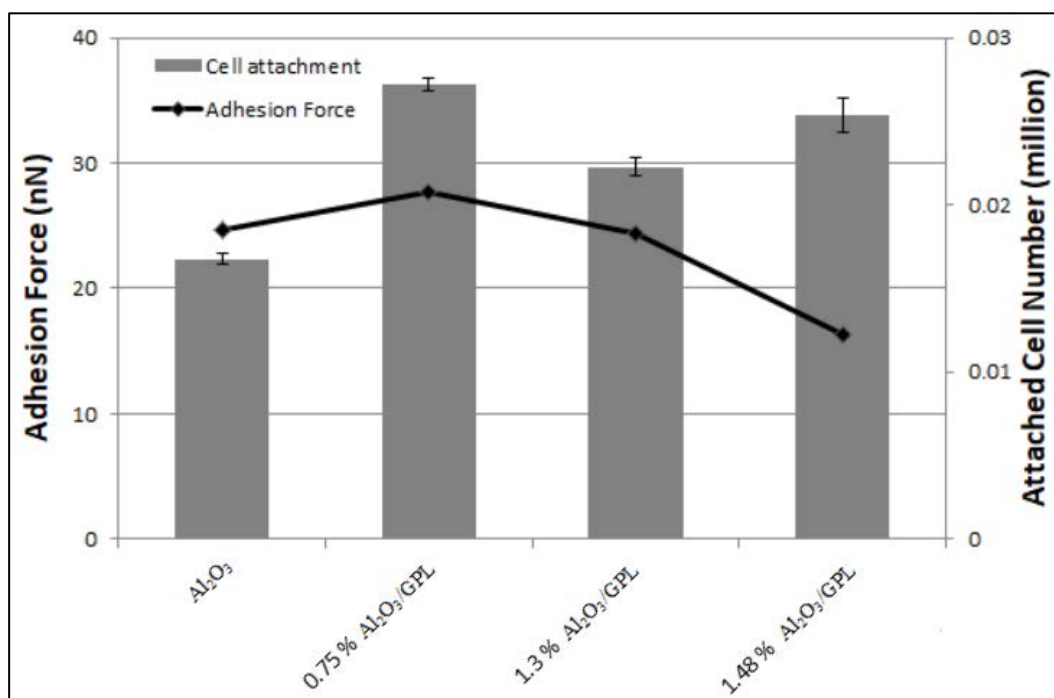


Figure 5.22: Surface adhesion forces and initial cell attachments on GPL/ Al_2O_3 composites Averaged surface adhesion forces (line) were measured by AFM. (N = 768) Attached viable cell numbers (bars) were calculated via an MTT assay. (Mean \pm SD, N = 3)

A similar comparison was performed for 3DGF and the nickel foam template. For the attached cell numbers data were extracted from the live/dead assay cell count results

(calculated as cell count number \times total volume of scaffold /cell count volume), and Figure 5.23 shows the comparison between surface adhesion forces and cell attachment data. As illustrated in Figure 5.23, cell attachments were less on the nickel template than that to 3DGF. Similarly, the surface adhesion of the nickel template (30 nN) was less than that of 3DGF (16 nN).

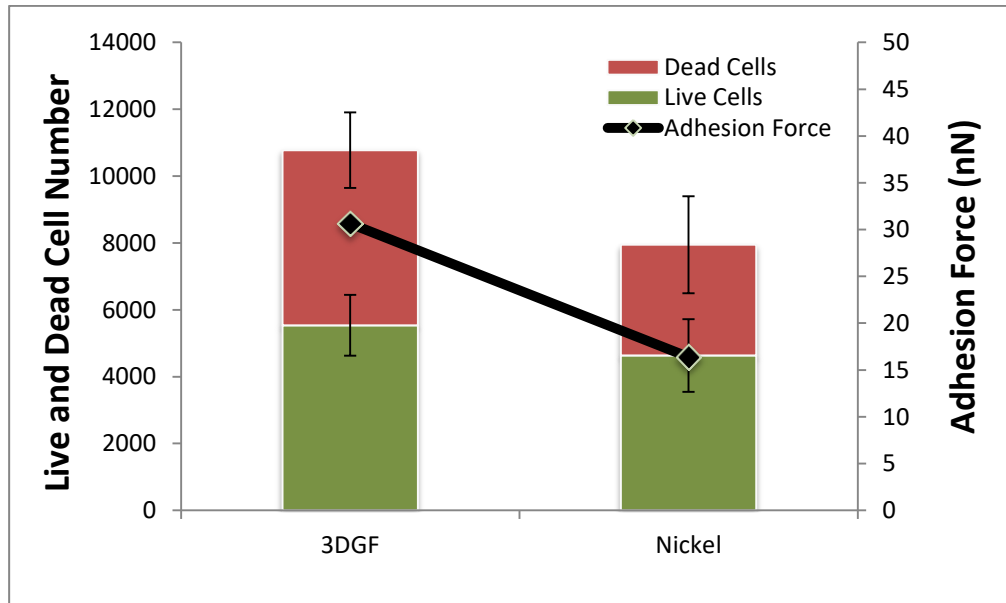


Figure 5.23: Surface adhesion forces and cell attachment on 3DGF vs nickel foam

Averaged surface adhesion forces (line) were measured by AFM. (N = 1280) An estimation of the cell number in the foams (bars) was based on the fluorescence cell count, and calculated by the equation: Total cell number = cell count number \times total volume of scaffold /cell count space volume. (Mean \pm SD, N = 3)

From the above proof-of-concept tests, this methodology has been preliminarily tested using experimental data for two new graphene composite materials, and it can be seen that the likelihood of cell attachment between the different samples could be estimated using simple surface nanoforces measurements. Although this methodology cannot provide a quantitative prediction and the accuracy of the prediction is not fully proven, it does have the potential for applications. By adopting this empirical methodology researchers can obtain a general idea about the initial cell attachment between different candidates, and this methodology can be carried out on target materials in the very early

stages or even during the concept design period. Consequently, this could allow large amounts of resource efforts to be saved.

In the future, the methodology can be further improved by more experiments on standard biomaterials using a consistent test procedure. With enough data and a reasonably accurate benchmark, this method has the potential to be used not only for cell attachment evaluation but also in combination with other technologies. For example, combined with nano-manipulation and molecular simulation it could be used to design and modify the surface molecules of a substrate in order to regulate initial cell attachment.

5.4 Summary of the Chapter

The first part of Chapter 5 presented the fabrication of Al₂O₃/GPL composites using a pressureless sintering approach, and an assessment of their mechanical properties. The results showed that the addition of GPLs to a ceramic matrix efficiently improved the mechanical properties by forming a more compact and refined matrix structure. The MTT assay outcomes demonstrated that Al₂O₃/GPL composites come with overall better cell attachment of MC3T3 cells, enabling them to spread and proliferate more than on the control substrates. However, porosity within the ceramics could increase the likelihood of GPL edges being exposed to the cells, which could lead to the prohibition of cell proliferation during the exponential growth stage. A fluorescent live/dead assay using BMSC yielded complicated results, although these were expected as the vital activities, especially cell differentiation, of BMSC are subject to many other surface conditions.

The second part of Chapter 5 introduced the fabrication process and testing of 3DGF. From the AFM indentation tests, 3DGF showed mechanical strength in a similar range

to other biological tissues, such as cartilage and gelatin. Interesting results were discovered around the rim structures on the graphene foam surface, as proved by the AFM force map, and the groove/rim structures on the 3DGF surface provided additional adhering forces due to the interlocking layers. As a porous matrix, 3DGF can facilitate nutrition intake and can provide an increased surface area for cells to attach. In addition, the similar mechanical stiffness to cartilage may provide similar mechanical stimuli to the cells growing on it. Consequently, it has the potential to support anchorage-dependent cells as a 3D scaffold for tissue engineering. *In vitro* tests were performed using MC3T3 cells and the results were assessed using confocal fluorescence microscopy. For the 3DGF used in this study, it took three days for MC3T3 cells to effectively spread throughout the matrix, which suggests that optimisation of the pore size and surface area is needed. The effect of the porosity of 3DGF on cell penetration was beyond the scope of this study but can certainly be investigated further. When compared to the nickel template matrix, 3DGF showed better cell attachment during both the initial attachment stage and the longer culturing period.

Finally, AFM measurements of both Al₂O₃/GPL composites and 3DGF were compared against the cell attachment data for proof-of-concept of an empirical methodology. The results showed that the methodology could reasonably predict the trend in cell attachment for a set of materials in a cost-saving and time-efficient manner. This part of the experimental results could also be treated as evidence that the correlation works in different conditions.

Chapter 6 - Conclusions and Future Work

6.1 Thesis Conclusions

This thesis presents an investigation of the hypothesis that surface nanoforces play an important role in the initial attachment of anchorage dependent cells.

The first part of the thesis presented how AFM indentations were performed in order to study the mechanical properties of living MC3T3 cells, and it was demonstrated to be an effective technique for evaluating living cells under aqueous conditions. AFM indentation carried out on live cells showed that the cytoplasm zone has on average higher stiffness and adhesion force than the nucleus zone. The Hertz and JKR models fitted well to the approach and detachment F-D curves, separately, and the elastic modulus acquired by the JKR model was generally larger than that of the Hertz model, although the difference was insignificant. After comparing with other researchers' measurements, it was found that MC3T3 cells did not show different elastic moduli when serum was present in the medium or not. The Hertz model is valuable for use as a quick estimation when dealing with a new sample; however, the JKR model better simulates force curves with large adhesion, as presented in the cell measurements. It was then shown that the adhesion force increased between cells and colloidal tips when the contact time was increased. Adhesive interactions between cells and colloidal tips surfaces build up with time, and this was characterised by an overall increased pull-out force and the frequent appearance of ligand-receptor breakup and tethering events in the AFM force curves. Different probes resulted in different levels of adhesion, during both short and long term contact. The JKR fitted elastic modulus between different tips showed no significant differences.

In the second part of this project, *in vitro* cell seeding and AFM measurements were carried out on different substrates. The experimental results initially indicated that the surface adhesive force is an important factor for initial cell attachment in serum-free culture conditions. The surface adhesion force and initial cell attachment data showed a statistically significant correlation when MC3T3 cells were cultured on treated glass substrates. Further experiments carried out using MC3T3, MEC and CTF cells also supported a general correlation between adhesion and attachment. A survey of previous *in vitro* experiments showed that cell attachment was generally correlated with surface adhesion for Al₂O₃ ceramic, PS, PDMS, glass, Ti (treated and untreated), and hydroxyapatite.

Graphene enhanced materials were manufactured and tested. Graphene platelets based ceramic composites (Al₂O₃/GPL) and porous 3DGF showed enhanced mechanical properties when compared to conventional materials. Smaller and more refined grain structures were achieved with increased GPL concentration from 0% to 1.4%. Bulk material flexural strength and fracture toughness of Al₂O₃/GPL composites were also tested and the results showed that the flexural strength and fracture toughness of Al₂O₃ was significantly improved by adding just 0.75% of GPL, which suggested that GPL had successfully been anchored in the ceramic matrix. A further increase in GPL led to a decrease in mechanical properties, which was probably caused by GPL clustering. AFM tests on 3DGF showed that a rim/groove structure had been formed by overlapping graphene layers. This rim structure generated higher local adhesion forces, which led to high surface roughness and more variance in surface adhesion. After Hertz fitting the elastic modulus of 3DGF was determined to be between 10 – 20 MPa, which is similar to that of gelatin and cartilage. Cell seeding of MC3T3 and BMSCs on top of Al₂O₃/GPL showed that adding GPL can lead to more initial cell attachment; however,

GPL clusters present on the ceramic surface could be harmful to cells in long-term culture. MC3T3 seeding experiments on 3DGF showed that cells could spread through the matrix after three days of culture, although general cell attachment was low. The conclusions from Chapter 4 lead to an empirical methodology, in which the adhesion force can be used as an estimation of initial cell attachment. In the final part of this research, surface adhesion forces of the graphene composite materials were acquired and compared to the initial cell attachment. The results showed that cell attachment on $\text{Al}_2\text{O}_3/\text{GPL}$ and 3DGF roughly corresponded to the adhesion force.

6.2 Future Work

In Chapter 3 it was shown that the nano-scale measurement of biological materials is highly case dependent and subtle. AFM measurements on live cells generally have large variance because cells are inhomogeneous and are subject to horizontal movement when under pressure. Therefore attention must be maintained during every step of the experiments. Another issue is that the AFM tips became contaminated after several indentations, which led to unreliable measurements, and these need to be changed for cleaning or replaced. Current research in this field is mostly based on the human processing of a limited amount of data, and standard measurement and analysis protocols, and automated AFM detection of cells are needed for large data throughput.

More studies are required to further validate the hypothesis of Chapter 4. It is well known that surface nano-features can dramatically modify the surface force characteristics of a material, just like the rim structure present on the 3DGF surface. It would be worth validating the correlation between nanoforces and cell attachment on substrates with specific nano-features. Repetition of systematically designed experiments is required, and more cell types and materials need to be tested. Tests with

a similar design could also widen the range where the empirical methodology could be applied.

Serum proteins are currently not considered in this work due to the complex processes involved in protein adsorption on cells and substrates. Protein deformation and reformation are also likely to affect cell attachment processes. It will be highly beneficial to take these proteins into consideration and investigate the relationship between adhesion and attachment under serum supplemented conditions. Time lapse observations are another direction that could be explored, as time lapse cell attachment data would allow a better understanding of how surface adhesion affects cell attachment.

Finally, an interesting direction worth exploring is to combine the nanoforces and attachment correlation with nano-manipulation techniques. Surfaces with artificially created adhesion force distributions could be manufactured and used to control the attachment of cells.

References

1. Homsy CA. Bio-Compatibility in selection of materials for implantation. *Journal of Biomedical Materials Research*. 1970;4(3):341-56.
2. Williams DF. On the mechanisms of biocompatibility. *Biomaterials*. 2008;29(20):2941-53.
3. Williams DF. *The Williams dictionary of biomaterials*: Liverpool University Press; 1999.
4. Porter JA, Von Fraunhofer JA. Success or failure of dental implants? A literature review with treatment considerations. *General Dentistry*. 2004;53(6):423-32; quiz 33, 46.
5. Polikov VS, Tresco PA, Reichert WM. Response of brain tissue to chronically implanted neural electrodes. *Journal of Neuroscience Methods*. 2005;148(1):1-18.
6. Montanaro L, Campoccia D, Arciola CR. Advancements in molecular epidemiology of implant infections and future perspectives. *Biomaterials*. 2007;28(34):5155-68.
7. Gorbet MB, Sefton MV. Endotoxin: the uninvited guest. *Biomaterials*. 2005;26(34):6811-7.
8. Anderson JM. Biological responses to materials. *Annual Review of Materials Research*. 2001;31(1):81-110.
9. Johnson H, Northup S, Seagraves P, Garvin P, Wallin R. Biocompatibility test procedures for materials evaluation *in vitro*. I. Comparative test system sensitivity. *Journal of Biomedical Materials Research*. 1983;17(4):571-86.
10. Pelham RJ, Wang Y-l. Cell locomotion and focal adhesions are regulated by substrate flexibility. *Proceedings of the National Academy of Sciences*. 1997;94(25):13661-5.
11. Lo C-M, Wang H-B, Dembo M, Wang Y-l. Cell movement is guided by the rigidity of the substrate. *Biophysical Journal*. 2000;79(1):144-52.
12. Ataollahi F, Pramanik S, Moradi A, Dalilottojari A, Pinguan - Murphy B, Abas W, et al. Endothelial cell responses in terms of adhesion, proliferation, and morphology to stiffness of polydimethylsiloxane elastomer substrates. *Journal of Biomedical Materials Research Part A*. 2015;103(7):2203-13.
13. Cortizo MS, Molinuevo MS, Cortizo AM. Biocompatibility and biodegradation of polyester and polyfumarate based - scaffolds for bone tissue engineering. *Journal of Tissue Engineering and Regenerative Medicine*. 2008;2(1):33-42.
14. Rezwan K, Chen Q, Blaker J, Boccaccini AR. Biodegradable and bioactive porous polymer/inorganic composite scaffolds for bone tissue engineering. *Biomaterials*. 2006;27(18):3413-31.
15. Hamdan M, Blanco L, Khraisat A, Tresguerres IF. Influence of titanium surface charge on fibroblast adhesion. *Clinical Implant Dentistry and Related Research*. 2006;8(1):32-8.

16. Hallab N, Bundy K, O'connor K, Clark R, Moses R. Cell adhesion to biomaterials: correlations between surface charge, surface roughness, adsorbed protein, and cell morphology. *Journal of Long-term Effects of Medical Implants*. 1994;5(3):209-31.
17. Richards R. The effect of surface roughness on fibroblast adhesion *in vitro*. *Injury*. 1996;27:S/C38-S/C43.
18. Washburn NR, Yamada KM, Simon CG, Kennedy SB, Amis EJ. High-throughput investigation of osteoblast response to polymer crystallinity: influence of nanometer-scale roughness on proliferation. *Biomaterials*. 2004;25(7):1215-24.
19. de Oliveira PT, Zalzal SF, Beloti MM, Rosa AL, Nanci A. Enhancement of *in vitro* osteogenesis on titanium by chemically produced nanotopography. *Journal of Biomedical Materials Research Part A*. 2007;80(3):554-64.
20. Swan EEL, Popat KC, Grimes CA, Desai TA. Fabrication and evaluation of nanoporous alumina membranes for osteoblast culture. *Journal of Biomedical Materials Research Part A*. 2005;72(3):288-95.
21. Richert L, Vetrone F, Yi JH, Zalzal SF, Wuest JD, Rosei F, et al. Surface nanopatterning to control cell growth. *Advanced Materials*. 2008;20(8):1488-92.
22. Webster TJ, Ergun C, Doremus RH, Siegel RW, Bizios R. Enhanced functions of osteoblasts on nanophase ceramics. *Biomaterials*. 2000;21(17):1803-10.
23. Khang D, Lu J, Yao C, Haberstroh KM, Webster TJ. The role of nanometer and sub-micron surface features on vascular and bone cell adhesion on titanium. *Biomaterials*. 2008;29(8):970-83.
24. Park J, Bauer S, von der Mark K, Schmuki P. Nanosize and vitality: TiO₂ nanotube diameter directs cell fate. *Nano Letters*. 2007;7(6):1686-91.
25. Park J, Bauer S, Schlegel KA, Neukam FW, von der Mark K, Schmuki P. TiO₂ nanotube surfaces: 15 nm—an optimal length scale of surface topography for cell adhesion and differentiation. *Small*. 2009;5(6):666-71.
26. Dalby M, Giannaras D, Riehle M, Gadegaard N, Affrossman S, Curtis A. Rapid fibroblast adhesion to 27nm high polymer demixed nano-topography. *Biomaterials*. 2004;25(1):77-83.
27. Dalby M, Pasqui D, Affrossman S, editors. Cell response to nano-islands produced by polymer demixing: a brief review. *IEE Proceedings-Nanobiotechnology*; 2004: IET.
28. Dalby MJ, Riehle MO, Sutherland DS, Agheli H, Curtis AS. Fibroblast response to a controlled nanoenvironment produced by colloidal lithography. *Journal of Biomedical Materials Research Part A*. 2004;69(2):314-22.
29. Brammer KS, Oh S, Cobb CJ, Bjursten LM, van der Heyde H, Jin S. Improved bone-forming functionality on diameter-controlled TiO₂ nanotube surface. *Acta Biomaterialia*. 2009;5(8):3215-23.
30. Oh S, Brammer KS, Li YJ, Teng D, Engler AJ, Chien S, et al. Stem cell fate dictated solely by altered nanotube dimension. *Proceedings of the National Academy of Sciences*. 2009;106(7):2130-5.
31. Walboomers X, Ginsel L, Jansen J. Early spreading events of fibroblasts on microgrooved substrates. *Journal of Biomedical Materials Research*. 2000;51(3):529-34.

32. Teixeira AI, Abrams GA, Bertics PJ, Murphy CJ, Nealey PF. Epithelial contact guidance on well-defined micro-and nanostructured substrates. *Journal of Cell Science*. 2003;116(10):1881-92.
33. Lim JY, Hansen JC, Siedlecki CA, Hengstebeck RW, Cheng J, Winograd N, et al. Osteoblast adhesion on poly (L-lactic acid)/polystyrene demixed thin film blends: effect of nanotopography, surface chemistry, and wettability. *Biomacromolecules*. 2005;6(6):3319-27.
34. Biggs MJ, Richards RG, Gadegaard N, McMurray RJ, Affrossman S, Wilkinson CD, et al. Interactions with nanoscale topography: adhesion quantification and signal transduction in cells of osteogenic and multipotent lineage. *Journal of Biomedical Materials Research Part A*. 2009;91(1):195-208.
35. Dalby MJ, McCloy D, Robertson M, Agheli H, Sutherland D, Affrossman S, et al. Osteoprogenitor response to semi-ordered and random nanotopographies. *Biomaterials*. 2006;27(15):2980-7.
36. Kalbacova M, Broz A, Babchenko O, Kromka A. Study on cellular adhesion of human osteoblasts on nano - structured diamond films. *physica status solidi (b)*. 2009;246(11 - 12):2774-7.
37. Dalby MJ, Gadegaard N, Tare R, Andar A, Riehle MO, Herzyk P, et al. The control of human mesenchymal cell differentiation using nanoscale symmetry and disorder. *Nature Materials*. 2007;6(12):997-1003.
38. Kunzler TP, Huwiler C, Drobek T, Vörös J, Spencer ND. Systematic study of osteoblast response to nanotopography by means of nanoparticle-density gradients. *Biomaterials*. 2007;28(33):5000-6.
39. Arnold M, Hirschfeld-Warneken VC, Lohmüller T, Heil P, Blümmel J, Cavalcanti-Adam EA, et al. Induction of cell polarization and migration by a gradient of nanoscale variations in adhesive ligand spacing. *Nano Letters*. 2008;8(7):2063-9.
40. Ryan JA. Evolution of cell culture surfaces. *BioFiles*. 2008;3:21.
41. Kim CH, Khil MS, Kim HY, Lee HU, Jahng KY. An improved hydrophilicity via electrospinning for enhanced cell attachment and proliferation. *Journal of Biomedical Materials Research Part B: Applied Biomaterials*. 2006;78(2):283-90.
42. Ramsey W, Hertl W, Nowlan E, Binkowski N. Surface treatments and cell attachment. *In Vitro*. 1984;20(10):802-8.
43. Amstein CF, Hartman PA. Adaptation of plastic surfaces for tissue culture by glow discharge. *Journal of Clinical Microbiology*. 1975;2(1):46-54.
44. Grinnell F, Milam M, Sreere PA. Studies on cell adhesion: II. Adhesion of cells to surfaces of diverse chemical composition and inhibition of adhesion by sulfhydryl binding reagents. *Archives of Biochemistry and Biophysics*. 1972;153(1):193-8.
45. Watson PH, Pon RT, Shiu RP. Inhibition of cell adhesion to plastic substratum by phosphorothioate oligonucleotide. *Experimental Cell Research*. 1992;202(2):391-7.
46. Yamagata M, Suzuki S, Akiyama S, Yamada K, Kimata K. Regulation of cell-substrate adhesion by proteoglycans immobilized on extracellular substrates. *Journal of Biological Chemistry*. 1989;264(14):8012-8.

47. Nishiguchi S, Nakamura T, Kobayashi M, Kim H-M, Miyaji F, Kokubo T. The effect of heat treatment on bone-bonding ability of alkali-treated titanium. *Biomaterials*. 1999;20(5):491-500.
48. Nordling S, Penttinen K, Saxen E. The effects of different methods of washing, drying and sterilizing glass surfaces on cell attachment and growth behavior. *Experimental Cell Research*. 1965;37(1):161-8.
49. Rappaport C, Poole JP, Rappaport HP. Studies on properties of surfaces required for growth of mammalian cells in synthetic medium. I. The HeLa cell. *Exp Cell Res*. 1960;20:465-79.
50. Cyster L, Parker K, Parker T, Grant D. The effect of surface chemistry and nanotopography of titanium nitride (TiN) films on 3T3 - L1 fibroblasts. *Journal of Biomedical Materials Research Part A*. 2003;67(1):138-47.
51. Cyster L, Parker K, Parker T, Grant D. The effect of surface chemistry and nanotopography of titanium nitride (TiN) films on primary hippocampal neurones. *Biomaterials*. 2004;25(1):97-107.
52. Schrand AM, Dai L, Schlager JJ, Hussain SM, Osawa E. Differential biocompatibility of carbon nanotubes and nanodiamonds. *Diamond and Related Materials*. 2007;16(12):2118-23.
53. Kim I-Y, Joachim E, Choi H, Kim K. Toxicity of silica nanoparticles depends on size, dose, and cell type. *Nanomedicine: Nanotechnology, Biology and Medicine*. 2015;11(6):1407-16.
54. Hussain M, Kabir M, Sood A. On the cytotoxicity of carbon nanotubes. *Current Science (00113891)*. 2009;96(5).
55. Jinno T, Goldberg VM, Davy D, Stevenson S. Osseointegration of surface - blasted implants made of titanium alloy and cobalt–chromium alloy in a rabbit intramedullary model. *Journal of Biomedical Materials Research Part A*. 1998;42(1):20-9.
56. Puleo DA, Thomas MV. Implant surfaces. *Dental Clinics of North America*. 2006;50(3):323-38.
57. Ingham E, Fisher J. The role of macrophages in osteolysis of total joint replacement. *Biomaterials*. 2005;26(11):1271-86.
58. Bergsma JE, De Bruijn W, Rozema F, Bos R, Boering G. Late degradation tissue response to poly (L-lactide) bone plates and screws. *Biomaterials*. 1995;16(1):25-31.
59. Anderson JM, Shive MS. Biodegradation and biocompatibility of PLA and PLGA microspheres. *Advanced drug delivery reviews*. 2012;64:72-82.
60. Bonzani IC, Adhikari R, Houshyar S, Mayadunne R, Gunatillake P, Stevens MM. Synthesis of two-component injectable polyurethanes for bone tissue engineering. *Biomaterials*. 2007;28(3):423-33.
61. D'Antonio J, Capello W, Manley M, Naughton M, Sutton K. Alumina ceramic bearings for total hip arthroplasty: five-year results of a prospective randomized study. *Clinical Orthopaedics and Related Research*. 2005;436:164-71.

62. Tanzer M, Gollish J, Leighton R, Orrell K, Giacchino A, Welsh P, et al. The effect of adjuvant calcium phosphate coating on a porous-coated femoral stem. *Clinical Orthopaedics and Related Research*. 2004;424:153-60.
63. Geesink R, Hoefnagels N. Six-year results of hydroxyapatite-coated total hip replacement. *Bone & Joint Journal*. 1995;77(4):534-47.
64. Ducheyne P, Qiu Q. Bioactive ceramics: the effect of surface reactivity on bone formation and bone cell function. *Biomaterials*. 1999;20(23):2287-303.
65. Dumbleton J, Manley MT. Hydroxyapatite-coated prostheses in total hip and knee arthroplasty. *Journal of Bone and Joint Surgery*. 2004;86(11):2526-40.
66. Bauer TW, Schils J. The pathology of total joint arthroplasty. *Skeletal Radiology*. 1999;28(8):423-32.
67. Olson RJ, Mamalis N, Werner L, Apple DJ. Cataract treatment in the beginning of the 21st century. *American Journal of Ophthalmology*. 2003;136(1):146-54.
68. Hollick EJ, Spalton DJ, Ursell PG, Pande MV. Biocompatibility of poly (methyl methacrylate), silicone, and AcrySof intraocular lenses: randomized comparison of the cellular reaction on the anterior lens surface. *Journal of Cataract and Refractive Surgery*. 1998;24(3):361-6.
69. Wejde G, Kugelberg M, Zetterström C. Posterior capsule opacification: comparison of 3 intraocular lenses of different materials and design. *Journal of Cataract and Refractive Surgery*. 2003;29(8):1556-9.
70. Hicks C, Crawford G, Lou X, Tan D, Snibson G, Sutton G, et al. Corneal replacement using a synthetic hydrogel cornea, AlphaCor™: device, preliminary outcomes and complications. *Eye*. 2003;17(3):385-92.
71. Van Essen T, Van Zijl L, Possemiers T, Mulder A, Zwart S, Chou C-H, et al. Biocompatibility of a fish scale-derived artificial cornea: Cytotoxicity, cellular adhesion and phenotype, and in vivo immunogenicity. *Biomaterials*. 2016;81:36-45.
72. Wilkoff BL, Rickard J, Tkatchouk E, Padsalgikar AD, Gallagher G, Runt J. The biostability of cardiac lead insulation materials as assessed from long - term human implants. *Journal of Biomedical Materials Research Part B: Applied Biomaterials*. 2016;104(2):411-21.
73. Santerre J, Woodhouse K, Laroche G, Labow R. Understanding the biodegradation of polyurethanes: from classical implants to tissue engineering materials. *Biomaterials*. 2005;26(35):7457-70.
74. Bertrand OF, Sipehia R, Mongrain R, Rodés J, Tardif J-C, Bilodeau L, et al. Biocompatibility aspects of new stent technology. *Journal of the American College of Cardiology*. 1998;32(3):562-71.
75. Mani G, Feldman MD, Patel D, Agrawal CM. Coronary stents: a materials perspective. *Biomaterials*. 2007;28(9):1689-710.
76. Zhang F, Liu X, Mao Y, Huang N, Chen Y, Zheng Z, et al. Artificial heart valves:: improved hemocompatibility by titanium oxide coatings prepared by ion beam assisted deposition. *Surface and Coatings Technology*. 1998;103:146-50.

77. Stamm C, Khosravi A, Grabow N, Schmohl K, Treckmann N, Drechsel A, et al. Biomatrix/polymer composite material for heart valve tissue engineering. *The Annals of Thoracic Surgery*. 2004;78(6):2084-93.
78. Buttafoco L, Kolkman N, Engbers-Buijtenhuijs P, Poot A, Dijkstra P, Vermes I, et al. Electrospinning of collagen and elastin for tissue engineering applications. *Biomaterials*. 2006;27(5):724-34.
79. Simionescu DT, Lu Q, Song Y, Lee J, Rosenbalm TN, Kelley C, et al. Biocompatibility and remodeling potential of pure arterial elastin and collagen scaffolds. *Biomaterials*. 2006;27(5):702-13.
80. Wang Y, Kim H-J, Vunjak-Novakovic G, Kaplan DL. Stem cell-based tissue engineering with silk biomaterials. *Biomaterials*. 2006;27(36):6064-82.
81. Hemmrich K, von Heimburg D, Rendchen R, Di Bartolo C, Milella E, Pallua N. Implantation of preadipocyte-loaded hyaluronic acid-based scaffolds into nude mice to evaluate potential for soft tissue engineering. *Biomaterials*. 2005;26(34):7025-37.
82. Gerecht - Nir S, Cohen S, Ziskind A, Itskovitz - Eldor J. Three - dimensional porous alginate scaffolds provide a conducive environment for generation of well - vascularized embryoid bodies from human embryonic stem cells. *Biotechnology and Bioengineering*. 2004;88(3):313-20.
83. Di Martino A, Sittinger M, Risbud MV. Chitosan: a versatile biopolymer for orthopaedic tissue-engineering. *Biomaterials*. 2005;26(30):5983-90.
84. Badylak S, Kokini K, Tullius B, Simmons-Byrd A, Morff R. Morphologic study of small intestinal submucosa as a body wall repair device. *Journal of Surgical Research*. 2002;103(2):190-202.
85. Taylor PM. Biological matrices and bionanotechnology. *Philosophical Transactions of the Royal Society of London B: Biological Sciences*. 2007;362(1484):1313-20.
86. Ando W, Tateishi K, Hart DA, Katakai D, Tanaka Y, Nakata K, et al. Cartilage repair using an *in vitro* generated scaffold-free tissue-engineered construct derived from porcine synovial mesenchymal stem cells. *Biomaterials*. 2007;28(36):5462-70.
87. Chardack WM, Brueske DA, Santomauro AP, Fazekas G. Experimental studies on synthetic substitutes for skin and their use in the treatment of burns. *Annals of Surgery*. 1962;155(1):127.
88. Rheinwatd JG, Green H. Serial cultivation of strains of human epidermal keratinocytes: the formation keratinizing colonies from single cell is. *Cell*. 1975;6(3):331-43.
89. Green H, Kehinde O, Thomas J. Growth of cultured human epidermal cells into multiple epithelia suitable for grafting. *Proceedings of the National Academy of Sciences*. 1979;76(11):5665-8.
90. Bell E, Ehrlich HP, Buttle DJ, Nakatsuji T. Living tissue formed *in vitro* and accepted as skin-equivalent tissue of full thickness. *Science*. 1981;211(4486):1052-4.
91. Yannas I, Burke J, Orgill D, Skrabut E. Wound tissue can utilize a polymeric template to synthesize a functional extension of skin. *Science*. 1982;215(4529):174-6.

92. Viola J, Lal B, Grad O. The emergence of tissue engineering as a research field. National Science Foundation, Arlington, VA. 2003.
93. Vacanti JP, Morse MA, Saltzman WM, Domb AJ, Perez-Atayde A, Langer R. Selective cell transplantation using bioabsorbable artificial polymers as matrices. *Journal of Pediatric Surgery*. 1988;23(1):3-9.
94. Brittberg M, Lindahl A, Nilsson A, Ohlsson C, Isaksson O, Peterson L. Treatment of deep cartilage defects in the knee with autologous chondrocyte transplantation. *New England Journal of Medicine*. 1994;331(14):889-95.
95. Atala A, Bauer SB, Soker S, Yoo JJ, Retik AB. Tissue-engineered autologous bladders for patients needing cystoplasty. *The Lancet*. 2006;367(9518):1241-6.
96. Macchiarini P, Jungebluth P, Go T, Asnaghi MA, Rees LE, Cogan TA, et al. Clinical transplantation of a tissue-engineered airway. *The Lancet*. 2008;372(9655):2023-30.
97. Post MJ. Cultured meat from stem cells: Challenges and prospects. *Meat Science*. 2012;92(3):297-301.
98. FDA. First artificial pancreas approved for use in the United States 2017. Available from: <https://www.diabetes.org.uk/Research/Research-round-up/First-artificial-pancreas-approved-for-use-in-the-United-States/>.
99. Aydin D, Louban I, Perschmann N, Blümmel J, Lohmüller T, Cavalcanti-Adam EA, et al. Polymeric substrates with tunable elasticity and nanoscopically controlled biomolecule presentation. *Langmuir*. 2010;26(19):15472-80.
100. von der Mark K, Park J, Bauer S, Schmuki P. Nanoscale engineering of biomimetic surfaces: cues from the extracellular matrix. *Cell and Tissue Research*. 2010;339(1):131.
101. Bierman A. Electrostatic forces between nonidentical colloidal particles. *Journal of Colloid Science*. 1955;10(3):231-45.
102. Derjaguin B. A theory of the heterocoagulation, interaction and adhesion of dissimilar particles in solutions of electrolytes. *Discussions of the Faraday Society*. 1954;18:85-98.
103. Overbeek JTG, Kruyt H. *Colloid science*. Elsevier, Amsterdam. 1952:264.
104. Hauser H, Wagner R. *Mammalian cell biotechnology in protein production*: De Gruyter; 1997.
105. Ungersböck A, Pohler O, Perren S. Evaluation of soft tissue reactions at the interface of titanium limited contact dynamic compression plate implants with different surface treatments: an experimental sheep study. *Biomaterials*. 1996;17(8):797-806.
106. Craighead H, Turner S, Davis R, James C, Perez A, John PS, et al. Chemical and topographical surface modification for control of central nervous system cell adhesion. *Biomedical Microdevices*. 1998;1(1):49-64.
107. Thomas WE, Discher DE, Shastri VP. Mechanical regulation of cells by materials and tissues. *MRS bulletin*. 2010;35(08):578-83.
108. Nemir S, West JL. Synthetic materials in the study of cell response to substrate rigidity. *Annals of biomedical engineering*. 2010;38(1):2-20.

109. Buxboim A, Rajagopal K, Andre'EX B, Discher DE. How deeply cells feel: methods for thin gels. *Journal of Physics: Condensed Matter*. 2010;22(19):194116.
110. Van der Valk J, Brunner D, De Smet K, Svenningsen ÅF, Honegger P, Knudsen LE, et al. Optimization of chemically defined cell culture media—replacing fetal bovine serum in mammalian *in vitro* methods. *Toxicology in Vitro*. 2010;24(4):1053-63.
111. Gstraunthaler G. Alternatives to the use of fetal bovine serum: serum-free cell culture. *Altex*. 2003;20(4):275-81.
112. Price PJ, Gregory EA. Relationship between *in vitro* growth promotion and biophysical and biochemical properties of the serum supplement. *In Vitro*. 1982;18(6):576-84.
113. Van der Valk J, Mellor D, Brands R, Fischer R, Gruber F, Gstraunthaler G, et al. The humane collection of fetal bovine serum and possibilities for serum-free cell and tissue culture. *Toxicology in Vitro*. 2004;18(1):1-12.
114. Even MS, Sandusky CB, Barnard ND. Serum-free hybridoma culture: ethical, scientific and safety considerations. *Trends in Biotechnology*. 2006;24(3):105-8.
115. Dormont D. Transmissible spongiform encephalopathy agents and animal sera. *Developments in Biological Standardization*. 1999(99):25-34.
116. Eloit M. Risks of virus transmission associated with animal sera or substitutes and methods of control. *Developments in Biological Standardization*. 1999;99:9.
117. Leckband D, Israelachvili J. Intermolecular forces in biology. *Quarterly Reviews of Biophysics*. 2001;34(02):105-267.
118. London F. The general theory of molecular forces. *Transactions of the Faraday Society*. 1937;33:8b-26.
119. Hamaker H. The London—van der Waals attraction between spherical particles. *Physica*. 1937;4(10):1058-72.
120. Israelachvili JN. *Intermolecular and surface forces*: Academic press; 2011.
121. Derjaguin B, Landau L. Theory of the stability of strongly charged lyophobic sols and of the adhesion of strongly charged particles in solutions of electrolytes. *Acta Physicochim URSS*. 1941;14(6):633-62.
122. Verwey E. Theory of the stability of lyophobic colloids. *The Journal of Physical Chemistry*. 1947;51(3):631-6.
123. Boni L, Hah J, Hui S, Mukherjee P, Ho J, Jung C. Aggregation and fusion of unilamellar vesicles by poly (ethylene glycol). *Biochimica et Biophysica Acta (BBA)-Biomembranes*. 1984;775(3):409-18.
124. Binnig G, Quate CF, Gerber C. Atomic force microscope. *Physical Review Letters*. 1986;56(9):930.
125. Butt H-J, Cappella B, Kappl M. Force measurements with the atomic force microscope: Technique, interpretation and applications. *Surface Science Reports*. 2005;59(1):1-152.
126. Kirmizis D, Logothetidis S. Atomic force microscopy probing in the measurement of cell mechanics. *International Journal of Nanomedicine*. 2010;5(137):e45.

127. Ohnesorge F, Hörber J, Häberle W, Czerny C, Smith D, Binnig G. AFM review study on pox viruses and living cells. *Biophysical Journal*. 1997;73(4):2183-94.
128. Häberle W, Hörber J, Ohnesorge F, Smith D, Binnig G. In situ investigations of single living cells infected by viruses. *Ultramicroscopy*. 1992;42:1161-7.
129. Fritz M, Radmacher M, Gaub HE. *In vitro* activation of human platelets triggered and probed by atomic force microscopy. *Experimental Cell Research*. 1993;205(1):187-90.
130. Maldonado-Valderrama J, Gunning AP, Wilde PJ, Morris VJ. *In vitro* gastric digestion of interfacial protein structures: visualisation by AFM. *Soft Matter*. 2010;6(19):4908-15.
131. Dufrêne YF, Marchal TG, Rouxhet PG. Influence of substratum surface properties on the organization of adsorbed collagen films: in situ characterization by atomic force microscopy. *Langmuir*. 1999;15(8):2871-8.
132. Quist A, Björck L, Reimann C, Oscarsson S, Sundqvist B. A scanning force microscopy study of human serum albumin and porcine pancreas trypsin adsorption on mica surfaces. *Surface Science*. 1995;325(1-2):L406-L12.
133. Evans E, Berk D, Leung A. Detachment of agglutinin-bonded red blood cells. I. Forces to rupture molecular-point attachments. *Biophysical Journal*. 1991;59(4):838-48.
134. Müller D, Schabert FA, Büldt G, Engel A. Imaging purple membranes in aqueous solutions at sub-nanometer resolution by atomic force microscopy. *Biophysical Journal*. 1995;68(5):1681-6.
135. Rief M, Pascual J, Saraste M, Gaub HE. Single molecule force spectroscopy of spectrin repeats: low unfolding forces in helix bundles. *Journal of Molecular Biology*. 1999;286(2):553-61.
136. Carrion-Vazquez M, Oberhauser AF, Fisher TE, Marszalek PE, Li H, Fernandez JM. Mechanical design of proteins studied by single-molecule force spectroscopy and protein engineering. *Progress in Biophysics and Molecular biology*. 2000;74(1):63-91.
137. Lee GU, Chrisey LA, Colton RJ. Direct measurement of the forces between complementary strands of DNA. *Science-New York then Washington*. 1994:771-.
138. André EB, Litvinov RI, Discher DE, Weisel JW. Forced unfolding of coiled-coils in fibrinogen by single-molecule AFM. *Biophysical Journal*. 2007;92(5):L39-L41.
139. Strunz T, Oroszlan K, Schäfer R, Güntherodt H-J. Dynamic force spectroscopy of single DNA molecules. *Proceedings of the National Academy of Sciences*. 1999;96(20):11277-82.
140. Ros R, Schwesinger F, Anselmetti D, Kubon M, Schäfer R, Plückthun A, et al. Antigen binding forces of individually addressed single-chain Fv antibody molecules. *Proceedings of the National Academy of Sciences*. 1998;95(13):7402-5.
141. Franz CM, Taubenberger A, Puech P-H, Muller DJ. Studying integrin-mediated cell adhesion at the single-molecule level using AFM force spectroscopy. *Sci Stke*. 2007;2007(406):pl5-pl.
142. Alsteens D, Beaussart A, El-Kirat-Chatel S, Sullan RMA, Dufre^ˆne YF. Atomic force microscopy: a new look at pathogens. *PLoS Pathog*. 2013;9(9):e1003516.

143. Lekka M, Laidler P, Ignacak J, Łabędź M, Lekki J, Struszczyk H, et al. The effect of chitosan on stiffness and glycolytic activity of human bladder cells. *Biochimica et Biophysica Acta (BBA)-Molecular Cell Research*. 2001;1540(2):127-36.
144. Li Q, Lee G, Ong C, Lim C. AFM indentation study of breast cancer cells. *Biochemical and Biophysical Research Communications*. 2008;374(4):609-13.
145. Cross SE, Jin Y-S, Tondre J, Wong R, Rao J, Gimzewski JK. AFM-based analysis of human metastatic cancer cells. *Nanotechnology*. 2008;19(38):384003.
146. Faria EC, Ma N, Gazi E, Gardner P, Brown M, Clarke NW, et al. Measurement of elastic properties of prostate cancer cells using AFM. *Analyst*. 2008;133(11):1498-500.
147. Hansma H, Vesenka J. Reproducible imaging and dissection of plasmid DNA under liquid with the atomic force microscope. *Science*. 1992;256(5060):1180.
148. Xu X-M, Ikai A. Retrieval and amplification of single-copy genomic DNA from a nanometer region of chromosomes: A new and potential application of atomic force microscopy in genomic research. *Biochemical and biophysical research communications*. 1998;248(3):744-8.
149. Han SW, Nakamura C, Obataya I, Nakamura N, Miyake J. A molecular delivery system by using AFM and nanoneedle. *Biosensors and Bioelectronics*. 2005;20(10):2120-5.
150. Benoit M, Gabriel D, Gerisch G, Gaub HE. Discrete interactions in cell adhesion measured by single-molecule force spectroscopy. *Nature Cell Biology*. 2000;2(6):313-7.
151. Kedrov A, Wegmann S, Smits SH, Goswami P, Baumann H, Muller DJ. Detecting molecular interactions that stabilize, activate and guide ligand-binding of the sodium/proton antiporter MjNhaP1 from *Methanococcus jannaschii*. *Journal of Structural Biology*. 2007;159(2):290-301.
152. Beaussart A, El-Kirat-Chatel S, Herman P, Alsteens D, Mahillon J, Hols P, et al. Single-cell force spectroscopy of probiotic bacteria. *Biophysical Journal*. 2013;104(9):1886-92.
153. Bowen J, Cheneler D, Walliman D, Arkless SG, Zhang Z, Ward MC, et al. On the calibration of rectangular atomic force microscope cantilevers modified by particle attachment and lamination. *Measurement Science and Technology*. 2010;21(11):115106.
154. Franz C, Puech P-H. Atomic force microscopy: a versatile tool for studying cell morphology, adhesion and mechanics. *Cellular and Molecular Bioengineering*. 2008;1(4):289-300.
155. Hertz H. *Hertz's Miscellaneous Papers; Chapters 5 and 6*. ed: Macmillan, London, UK. 1896.
156. Johnson K, Kendall K, Roberts A, editors. *Surface energy and the contact of elastic solids*. Proceedings of the Royal Society of London A: Mathematical, Physical and Engineering Sciences; 1971: The Royal Society.
157. Derjaguin BV, Muller VM, Toporov YP. Effect of contact deformations on the adhesion of particles. *Journal of Colloid and Interface Science*. 1975;53(2):314-26.

158. Tabor D. Surface forces and surface interactions. *Journal of Colloid and Interface Science*. 1977;58(1):2-13.
159. Song Z, Komvopoulos K. Adhesion-induced instabilities in elastic and elastic-plastic contacts during single and repetitive normal loading. *Journal of the Mechanics and Physics of Solids*. 2011;59(4):884-97.
160. Koay EJ, Shieh AC, Athanasiou KA. Creep indentation of single cells. *Journal of Biomechanical Engineering*. 2003;125(3):334-41.
161. Bausch AR, Ziemann F, Boulbitch AA, Jacobson K, Sackmann E. Local measurements of viscoelastic parameters of adherent cell surfaces by magnetic bead microrheometry. *Biophysical Journal*. 1998;75(4):2038-49.
162. Gardinier JD, Majumdar S, Duncan RL, Wang L. Cyclic hydraulic pressure and fluid flow differentially modulate cytoskeleton re-organization in MC3T3 osteoblasts. *Cellular and Molecular Bioengineering*. 2009;2(1):133-43.
163. Takai E, Costa KD, Shaheen A, Hung CT, Guo XE. Osteoblast elastic modulus measured by atomic force microscopy is substrate dependent. *Annals of Biomedical Engineering*. 2005;33(7):963-71.
164. Bélanger MC, Marois Y. Hemocompatibility, biocompatibility, inflammatory and in vivo studies of primary reference materials low - density polyethylene and polydimethylsiloxane: A review. *Journal of Biomedical Materials Research*. 2001;58(5):467-77.
165. Mata A, Fleischman AJ, Roy S. Characterization of polydimethylsiloxane (PDMS) properties for biomedical micro/nanosystems. *Biomedical Microdevices*. 2005;7(4):281-93.
166. Efimenko K, Wallace WE, Genzer J. Surface modification of Sylgard-184 poly (dimethyl siloxane) networks by ultraviolet and ultraviolet/ozone treatment. *Journal of Colloid and Interface Science*. 2002;254(2):306-15.
167. Fuard D, Tzvetkova-Chevolleau T, Decossas S, Tracqui P, Schiavone P. Optimization of poly-di-methyl-siloxane (PDMS) substrates for studying cellular adhesion and motility. *Microelectronic Engineering*. 2008;85(5):1289-93.
168. Bartalena G, Loosli Y, Zambelli T, Snedeker J. Biomaterial surface modifications can dominate cell-substrate mechanics: the impact of PDMS plasma treatment on a quantitative assay of cell stiffness. *Soft Matter*. 2012;8(3):673-81.
169. Mosmann T. Rapid colorimetric assay for cellular growth and survival: application to proliferation and cytotoxicity assays. *Journal of Immunological Methods*. 1983;65(1-2):55-63.
170. Kim HM, Miyaji F, Kokubo T, Nakamura T. Preparation of bioactive Ti and its alloys via simple chemical surface treatment. *Journal of Biomedical Materials Research Part A*. 1996;32(3):409-17.
171. Kim H, Miyaji F, Kokubo T, Nakamura T. Effect of heat treatment on apatite-forming ability of Ti metal induced by alkali treatment. *Journal of Materials Science: Materials in Medicine*. 1997;8(6):341-7.
172. Liu X, Chu PK, Ding C. Surface modification of titanium, titanium alloys, and related materials for biomedical applications. *Materials Science and Engineering: R: Reports*. 2004;47(3):49-121.

173. Maitz M, Poon R, Liu X, Pham M-T, Chu PK. Bioactivity of titanium following sodium plasma immersion ion implantation and deposition. *Biomaterials*. 2005;26(27):5465-73.
174. Park BS, Heo SJ, Kim CS, Oh JE, Kim JM, Lee G, et al. Effects of adhesion molecules on the behavior of osteoblast - like cells and normal human fibroblasts on different titanium surfaces. *Journal of Biomedical Materials Research Part A*. 2005;74(4):640-51.
175. Nebe B, Finke B, Lüthen F, Bergemann C, Schröder K, Rychly J, et al. Improved initial osteoblast functions on amino-functionalized titanium surfaces. *Biomolecular Engineering*. 2007;24(5):447-54.
176. Okamoto K, Matsuura T, Hosokawa R, Akagawa Y. RGD peptides regulate the specific adhesion scheme of osteoblasts to hydroxyapatite but not to titanium. *Journal of Dental Research*. 1998;77(3):481-7.
177. Liu J, Yang Y, Hassanin H, Jumbu N, Deng S, Zuo Q, et al. Graphene–Alumina Nanocomposites with Improved Mechanical Properties for Biomedical Applications. *ACS Applied Materials and Interfaces*. 2016;8(4):2607-16.
178. Geim AK, Novoselov KS. The rise of graphene. *Nature Materials*. 2007;6(3):183-91.
179. Lee C, Wei X, Kysar JW, Hone J. Measurement of the elastic properties and intrinsic strength of monolayer graphene. *Science*. 2008;321(5887):385-8.
180. Bolotin KI, Sikes K, Jiang Z, Klima M, Fudenberg G, Hone J, et al. Ultrahigh electron mobility in suspended graphene. *Solid State Communications*. 2008;146(9):351-5.
181. Balandin AA, Ghosh S, Bao W, Calizo I, Teweldebrhan D, Miao F, et al. Superior thermal conductivity of single-layer graphene. *Nano Letters*. 2008;8(3):902-7.
182. Li N, Zhang X, Song Q, Su R, Zhang Q, Kong T, et al. The promotion of neurite sprouting and outgrowth of mouse hippocampal cells in culture by graphene substrates. *Biomaterials*. 2011;32(35):9374-82.
183. Liao K-H, Lin Y-S, Macosko CW, Haynes CL. Cytotoxicity of graphene oxide and graphene in human erythrocytes and skin fibroblasts. *ACS Applied Materials and Interfaces*. 2011;3(7):2607-15.
184. Yang X, Wang Y, Huang X, Ma Y, Huang Y, Yang R, et al. Multi-functionalized graphene oxide based anticancer drug-carrier with dual-targeting function and pH-sensitivity. *Journal of Materials Chemistry*. 2011;21(10):3448-54.
185. Vallabani N, Mittal S, Shukla RK, Pandey AK, Dhakate SR, Pasricha R, et al. Toxicity of graphene in normal human lung cells (BEAS-2B). *Journal of Biomedical Nanotechnology*. 2011;7(1):106-7.
186. Hu W, Peng C, Lv M, Li X, Zhang Y, Chen N, et al. Protein corona-mediated mitigation of cytotoxicity of graphene oxide. *ACS Nano*. 2011;5(5):3693-700.
187. Sasidharan A, Panchakarla L, Chandran P, Menon D, Nair S, Rao C, et al. Differential nano-bio interactions and toxicity effects of pristine versus functionalized graphene. *Nanoscale*. 2011;3(6):2461-4.

188. Wang K, Ruan J, Song H. Biocompatibility of graphene oxide, *Nanoscale Res Lett*, 6, 1 (2011). Google Scholar.
189. Yang K, Wan J, Zhang S, Zhang Y, Lee S-T, Liu Z. In vivo pharmacokinetics, long-term biodistribution, and toxicology of PEGylated graphene in mice. *ACS Nano*. 2010;5(1):516-22.
190. Zhang X, Yin J, Peng C, Hu W, Zhu Z, Li W, et al. Distribution and biocompatibility studies of graphene oxide in mice after intravenous administration. *Carbon*. 2011;49(3):986-95.
191. Park SY, Park J, Sim SH, Sung MG, Kim KS, Hong BH, et al. Enhanced differentiation of human neural stem cells into neurons on graphene. *Advanced Materials*. 2011;23(36).
192. Nayak TR, Andersen H, Makam VS, Khaw C, Bae S, Xu X, et al. Graphene for controlled and accelerated osteogenic differentiation of human mesenchymal stem cells. *ACS Nano*. 2011;5(6):4670-8.
193. Ding X, Liu H, Fan Y. Graphene - Based Materials in Regenerative Medicine. *Advanced Healthcare Materials*. 2015;4(10):1451-68.
194. Yan Z-Q, Zhang W. The development of graphene-based devices for cell biology research. *Frontiers of Materials Science*. 2014;8(2):107-22.
195. Dubey N, Bentini R, Islam I, Cao T, Castro Neto AH, Rosa V. Graphene: a versatile carbon-based material for bone tissue engineering. *Stem Cells International*. 2015;2015.
196. Dong H, Dong C, Ren T, Li Y, Shi D. Surface-engineered graphene-based nanomaterials for drug delivery. *Journal of Biomedical Nanotechnology*. 2014;10(9):2086-106.
197. John AA, Subramanian AP, Vellayappan MV, Balaji A, Mohandas H, Jaganathan SK. Carbon nanotubes and graphene as emerging candidates in neuroregeneration and neurodrug delivery. *International Journal of Nanomedicine*. 2015;10:4267.
198. Chaudhary K. Graphene, its synthesis and its application in anti-cancer drug delivery. *International Journal of Science and Research*. 2015;4(8):741-4.
199. Liu J, Cui L, Losic D. Graphene and graphene oxide as new nanocarriers for drug delivery applications. *Acta Biomaterialia*. 2013;9(12):9243-57.
200. Yang K, Feng L, Liu Z. The advancing uses of nano-graphene in drug delivery. *Expert Opinion on Drug Delivery*. 2015;12(4):601-12.
201. Liu Z, Robinson JT, Tabakman SM, Yang K, Dai H. Carbon materials for drug delivery & cancer therapy. *Materials Today*. 2011;14(7):316-23.
202. Kwon OS, Park SJ, Hong J-Y, Han A-R, Lee JS, Lee JS, et al. Flexible FET-type VEGF aptasensor based on nitrogen-doped graphene converted from conducting polymer. *ACS Nano*. 2012;6(2):1486-93.
203. Ohno Y, Maehashi K, Matsumoto K. Label-free biosensors based on aptamer-modified graphene field-effect transistors. *Journal of the American Chemical Society*. 2010;132(51):18012-3.

204. Chen Y, Vedala H, Kotchey GP, Audfray A, Cecioni S, Imberty A, et al. Electronic detection of lectins using carbohydrate-functionalized nanostructures: graphene versus carbon nanotubes. *Acs Nano*. 2011;6(1):760-70.
205. Pu Y, Zhu Z, Han D, Liu H, Liu J, Liao J, et al. Insulin-binding aptamer-conjugated graphene oxide for insulin detection. *Analyst*. 2011;136(20):4138-40.
206. He S, Song B, Li D, Zhu C, Qi W, Wen Y, et al. A graphene nanoprobe for rapid, sensitive, and multicolor fluorescent DNA analysis. *Advanced Functional Materials*. 2010;20(3):453-9.
207. Wen Y, Xing F, He S, Song S, Wang L, Long Y, et al. A graphene-based fluorescent nanoprobe for silver (I) ions detection by using graphene oxide and a silver-specific oligonucleotide. *Chemical Communications*. 2010;46(15):2596-8.
208. Liu M, Zhao H, Chen S, Yu H, Zhang Y, Quan X. Label-free fluorescent detection of Cu (II) ions based on DNA cleavage-dependent graphene-quenched DNazymes. *Chemical Communications*. 2011;47(27):7749-51.
209. Sailer I, Philipp A, Zembic A, Pjetursson BE, Hämmerle CH, Zwahlen M. A systematic review of the performance of ceramic and metal implant abutments supporting fixed implant reconstructions. *Clinical Oral Implants Research*. 2009;20(s4):4-31.
210. Thamaraiselvi T, Rajeswari S. Biological evaluation of bioceramic materials-a review. *Carbon*. 2004;24(31):172.
211. Andersson B, Taylor Å, Lang BR, Scheller H, Schärer P, Sorensen JA, et al. Alumina ceramic implant abutments used for single-tooth replacement: a prospective 1- to 3-year multicenter study. *International Journal of Prosthodontics*. 2001;14(5).
212. Raigrodski AJ, Chiche GJ, Potiket N, Hochstedler J, Mohamed SE, Billiot S, et al. The efficacy of posterior three-unit zirconium-oxide-based ceramic fixed partial dental prostheses: A prospective clinical pilot study. *Journal of Prosthetic Dentistry*. 2006;96(4):237-44.
213. Ehrl P, Reuther J, Frenkel G. Al₂O₃-Ceramic as material for dental implants: experimental and clinical study for the development of screw-and extension-implants. *International Journal of Oral Surg*. 1981;10(1):93-8.
214. Klawitter JJ, Weinstein AM, Cooke FW, Peterson LJ, Pennel BM, McKinney jr RV. An evaluation of porous alumina ceramic dental implants. *Journal of Dental Research*. 1977;56(7):768-76.
215. Griss P, Silber R, Merkle B, Haehner K, Heimke G, Krempien B. Biomechanically induced tissue reactions after Al₂O₃-ceramic hip joint replacement. Experimental and early clinical results. *Journal of Biomedical Materials Research Part A*. 1976;10(4):519-28.
216. Rahaman MN, Yao A, Bal BS, Garino JP, Ries MD. Ceramics for prosthetic hip and knee joint replacement. *Journal of the American Ceramic Society*. 2007;90(7):1965-88.
217. Cao W, Hench LL. Bioactive materials. *Ceramics international*. 1996;22(6):493-507.

218. Becher PF, Sun EY, Plucknett KP, Alexander KB, Hsueh CH, Lin HT, et al. Microstructural design of silicon nitride with improved fracture toughness: I, effects of grain shape and size. *Journal of the American Ceramic Society*. 1998;81(11):2821-30.
219. Rajendran S. Production of ultrafine alpha alumina powders and fabrication of fine grained strong ceramics. *Journal of Materials Science*. 1994;29(21):5664-72.
220. Zhan G-D, Mitomo M, Kim Y-W. Microstructural control for strengthening of silicon carbide ceramics. *Journal of American Ceramic Society*. 1999;82(10):2924-6.
221. Ducheyne P, Healy K, Hutmacher DE, Grainger DW, Kirkpatrick CJ. *Comprehensive biomaterials*: Newnes; 2015.
222. Frank I, Tanenbaum DM, Van der Zande A, McEuen PL. Mechanical properties of suspended graphene sheets. *Journal of Vacuum Science and Technology B: Microelectronics and Nanometer Structures Processing, Measurement, and Phenomena*. 2007;25(6):2558-61.
223. Vacanti JP, Langer R. Tissue engineering: the design and fabrication of living replacement devices for surgical reconstruction and transplantation. *The Lancet*. 1999;354:S32-S4.
224. Kostarelos K, Vincent M, Hebert C, Garrido JA. Graphene in the Design and Engineering of Next - Generation Neural Interfaces. *Advanced Materials*. 2017;29(42).
225. Li N, Zhang Q, Gao S, Song Q, Huang R, Wang L, et al. Three-dimensional graphene foam as a biocompatible and conductive scaffold for neural stem cells. *Scientific Reports*. 2013;3:1604.
226. Song Q, Jiang Z, Li N, Liu P, Liu L, Tang M, et al. Anti-inflammatory effects of three-dimensional graphene foams cultured with microglial cells. *Biomaterials*. 2014;35(25):6930-40.
227. Mena F, Abdelghani A, Mena B. Graphene nanomaterials as biocompatible and conductive scaffolds for stem cells: impact for tissue engineering and regenerative medicine. *Journal of Tissue Engineering and Regenerative Medicine*. 2015;9(12):1321-38.
228. Li Z, Wang H, Yang B, Sun Y, Huo R. Three-dimensional graphene foams loaded with bone marrow derived mesenchymal stem cells promote skin wound healing with reduced scarring. *Materials Science and Engineering: C*. 2015;57:181-8.
229. Xie H, Cao T, Gomes JV, Neto AHC, Rosa V. Two and three-dimensional graphene substrates to magnify osteogenic differentiation of periodontal ligament stem cells. *Carbon*. 2015;93:266-75.
230. Xi K, Kidambi PR, Chen R, Gao C, Peng X, Ducati C, et al. Binder free three-dimensional sulphur/few-layer graphene foam cathode with enhanced high-rate capability for rechargeable lithium sulphur batteries. *Nanoscale*. 2014;6(11):5746-53.
231. Porwal H, Tatarko P, Grasso S, Khaliq J, Dlouhý I, Reece MJ. Graphene reinforced alumina nano-composites. *Carbon*. 2013;64:359-69.
232. JPK Instruments. Using Atomic Force Microscopy to Determine Elastic Properties of Biological Samples by JPK Instruments. 2009. Available from: <http://www.azonano.com/article.aspx?ArticleID=2270>.

233. Flanagan LA, Ju Y-E, Marg B, Osterfield M, Janmey PA. Neurite branching on deformable substrates. *Neuroreport*. 2002;13(18):2411.
234. Rowley JA, Madlambayan G, Mooney DJ. Alginate hydrogels as synthetic extracellular matrix materials. *Biomaterials*. 1999;20(1):45-53.
235. Gray DS, Tien J, Chen CS. Repositioning of cells by mechanotaxis on surfaces with micropatterned Young's modulus. *Journal of Biomedical Materials Research Part A*. 2003;66(3):605-14.
236. Vedula SRK, Hirata H, Nai MH, Toyama Y, Treppe X, Lim CT, et al. Epithelial bridges maintain tissue integrity during collective cell migration. *Nature Materials*. 2014;13(1):87-96.